POLITECNICO DI MILANO
DEPARTMENT OF AEROSPACE SCIENCE AND TECHNOLOGY
DOCTORAL PROGRAMME IN AEROSPACE ENGINEERING

ORBIT PROPAGATION AND UNCERTAINTY MODELLING FOR PLANETARY PROTECTION COMPLIANCE VERIFICATION

Doctoral Dissertation of:
Matteo Romano

Supervisor:
Prof. Camilla Colombo

Technical advisor:
Mr. José Manuel Sánchez Pérez

Academic year 2019/20 – Cycle XXXII

Doctoral Dissertation of:		**Matteo Romano**
Supervisor:	**Prof.**	**Camilla Colombo**
Technical advisor:	**Mr.**	**José Manuel Sánchez Pérez**
Coordinator of the Doctoral Program:	**Prof.**	**Pierangelo Masarati**
External reviewer:	**Prof.**	**Giacomo Tommei**
External reviewer:	**Prof.**	**Kleomenis Tsiganis**

Romano, Matteo (2020), *Orbit propagation and uncertainty modelling for planetary protection compliance verification*, PhD thesis, Politecnico di Milano, Supervisors: Colombo, Camilla and Sánchez Pérez, José Manuel

Abstract

At the beginning of interplanetary missions, launcher upper stages may be left orbiting the Sun on trajectories that may bring them close to other planets, with the risk of impacting and contaminating them. For this reason, all interplanetary missions must comply to planetary protection requirements. These guidelines have the goal of limiting the probability of unwanted collisions between mission-related objects and celestial bodies that may host extra-terrestrial life forms or conditions favourable to their development.

The aim of the research presented in this thesis is to develop new techniques and numerical tools to improve the means currently employed in planetary protection analysis. The proposed approach focuses on different methods for numerical propagation, uncertainty sampling and uncertainty propagation to make the verification of compliance to planetary protection requirements more precise and affordable. In this work, particular attention is given to the main aspects affecting the reliability and affordability of planetary protection analysis.

In particular, the orbital propagation in the n-body dynamics which causes issues on a numerical level due to the occurrence of close approaches with celestial bodies is addressed by selecting methods for the integration of the trajectories and comparing them in various test cases. The effect of numerical integration errors on the overall planetary protection analysis is assessed, and a novel approach to deal with close encounters with planets is proposed. This method establishes a criterion based on the eigenvalues of the Jacobian of the equations of motion to detect when a fly-by occurs during the propagation: this provides a definition that avoids neglecting some of these events in the analysis, as a way to identify all possible conditions that affect the simulation and to contain their effects at the numerical level.

On the side of the estimation of impact probability, a novel application of the Line Sampling method is proposed as an alternative to the standard approach based on Monte Carlo simulation. During the research, the method was implemented and validated for planetary protection analysis and made more effective by developing new algorithms to increase its accuracy and efficiency: these novel techniques allow to extend the applicability of the method to more complex cases, where multiple impact events and very low probability levels are expected.

Finally, uncertainty propagation methods were also applied to planetary protection, to overcome the limitations of sampling methods. The use of Gaussian Mixture Models and of adaptive splitting of the distribution is proposed to accurately propagate the initial uncertainty characterising the state of a mission-related object into interplanetary orbits, and to estimate efficiently the probability of impacts.

Sommario

All'inizio delle missioni interplanetarie, gli stadi superiori dei lanciatori possono essere lasciati in orbita attorno al Sole su traiettorie che potrebbero avvicinarli ad altri pianeti, con il rischio di collidere con essi e contaminarli. Per questo motivo, tutte le missioni interplanetarie devono essere conformi ai requisiti di protezione planetaria. Queste linee guida hanno lo scopo di limitare la probabilità di collisioni indesiderate tra oggetti legati alla missione e corpi celesti che possono ospitare forme di vita extraterrestri o condizioni favorevoli al loro sviluppo.

Lo scopo della ricerca presentata in questa tesi è quello di sviluppare nuove tecniche e strumenti numerici per migliorare i mezzi attualmente impiegati nell'analisi di protezione planetaria. L'approccio proposto si concentra su diversi metodi per la propagazione numerica, il campionamento dell'incertezza e la sua propagazione per rendere più precisa ed efficiente la verifica della conformità ai requisiti di protezione planetaria. In questo lavoro, particolare attenzione è data ai principali aspetti che influenzano l'affidabilità e l'efficienza dell'analisi di protezione planetaria.

In particolare, la propagazione orbitale nella dinamica degli n-corpi, che causa problemi a livello numerico dovuti al verificarsi di incontri ravvicinati con corpi celesti, viene affrontata selezionando metodi per l'integrazione di traiettorie e confrontandoli in vari casi test. L'effetto degli errori di integrazione numerica sull'analisi di protezione planetaria viene valutato, e viene proposto un nuovo approccio per affrontare gli incontri ravvicinati con i pianeti. Questo metodo stabilisce un criterio basato sugli autovalori della matrice jacobiana delle equazioni del moto per rilevare quando si verifica un fly-by durante la propagazione: ciò fornisce una definizione che evita di trascurare alcuni di questi eventi nell'analisi, permettendo di identificare tutte le possibili condizioni che influenzano la simulazione e per contenere i loro effetti a livello numerico.

Sul fronte della stima della probabilità di impatto, viene proposta una nuova applicazione del metodo del Line Sampling come alternativa all'approccio standard basato sulla simulazione Monte Carlo. Nel corso della ricerca, il metodo è stato implementato e validato per l'analisi di protezione planetaria e reso più efficace sviluppando nuovi algoritmi per aumentarne l'accuratezza e l'efficienza: queste nuove tecniche permettono di estendere l'applicabilità del metodo a casi più complessi, dove sono previsti eventi di impatto multipli e livelli di probabilità molto bassi.

Infine, alla protezione planetaria sono stati applicati anche metodi di propagazione dell'incertezza, per superare i limiti dei metodi di campionamento. L'uso di Gaussian Mixture Models e di splitting adattivo della distribuzione viene proposto per propagare accuratamente l'incertezza iniziale che caratterizza lo stato di un oggetto della missione in orbite interplanetarie, e per stimare in modo efficiente la probabilità di impatti.

Acknowledgements

First, I would like to acknowledge my supervisor, Prof. Camilla Colombo. I cannot imagine how I could have faced the last three years without you, Camilla, and I cannot thank you enough for your constant support and ever strong enthusiasm, and for guiding me with endless trust and patience.

I would like to acknowledge José Manuel Sanchéz Peréz and express my gratitude to him for accepting to be my advisor. Thank you for guiding me during my stays at ESOC, and for lending me your precious expertise in mission analysis.

Many of my thoughts go to the whole COMPASS team, who accompanied me along this journey. Thank you Davide, Simeng, Stefan, and Ioannis who were there from the beginning, and thank you Mirko, Juan, Narcís, Gabriella, Marco, and Giacomo who joined us along the way. You have been excellent friends and the best team I could have hoped for.

I would like to express my gratitude to the members of the Department of Aerospace Science and Technology at Politecnico di Milano, for granting an environment both professional and friendly, rich with opportunities to improve myself.

Thanks to the friends who were with me from the start and to the ones I found along the way, those who made Milano feel like the centre of the world, and those who made Darmstadt a sunnier place. Thank you for the countless new experiences you offered me, you are many of the reasons I don't regret taking on this endeavour.

Last, but not least, I would like to thank my family, from the bottom of my heart. Thank you mum and dad for your unconditional support and for the sacrifices you've made for me, for every cup of tea and for every morning race to the train station.

The doctoral research presented in this thesis has received funding from the European Research Council (ERC) under the European Union's Horizon 2020 research and innovation programme as part of project COMPASS (Grant agreement No 679086), and from the European Space Agency (ESA) though a Networking/Partnering Initiative (NPI) agreement.

Contents

List of Figures

List of Tables

List of acronyms

List of acronyms

AU Astronomical Unit

CA Close approach

CDF Cumulative distribution function

COMPASS Control for Orbit Manoeuvring through Perturbations for Application to Space Systems

COSPAR Committee on Space Research

DA Differential Algebra

EKF Extended Kalman Filter

ERC European Research Council

ESA European Space Agency

ESOC European Space Operations Centre

FPE Fokker-Plank Equation

GMM Gaussian Mixture Model

IS Importance Sampling

JPL Jet Propulsion Laboratory

KS Kustaanheimo-Stiefel

LOV Line Of Variations

LS Line Sampling

MC Monte Carlo

List of acronyms

MCMC Markov Chain Monte Carlo

MOID Minimum Orbital Intersection Distance

NBP n-body problem

NEA Near Earth Asteroid

NEO Near Earth Object

NPI Networking/Partnering Initiative

PCE Polynomial Chaos Expansion

pdf Probability density function

RK Runge-Kutta

SNAPPshot Suite for the Numerical Analysis of Planetary Protection

SOI Sphere of Influence

SS Subset Simulation

STM State Transition Matrix

STT State Transition Tensor

UT Unscented Transformation

CHAPTER 1

Introduction

Exploration missions to other planets and moons must comply to planetary protection guidelines in order to reduce the risk of contaminating them with biological material from Earth. As these missions leave the Earth, the launcher stages used to inject the spacecraft into the final transfer orbit are also left on trajectories that, in the course of years or even decades, may return to the Earth or impact other planets. Furthermore, a spacecraft may become uncontrollable during the course of the mission due to failures of one of the main on-board systems, or its trajectory may deviate from the nominal one due to manoeuvring errors.

Planetary protection requirements act on the design of a mission by setting a limit to the probability of a collision between mission-related objects and protected celestial bodies, which may be the subjects of biological studies and future targets for exploration missions aiming to search for extra-terrestrial life [2]. To protect these environments, planetary protection policy is adopted internationally and put into act by countries and Space Agencies. Quantifying the risk of unwanted collisions with these planets and moons becomes a duty of great importance for mission designers.

Verifying the compliance to these requirements is a key aspect of space mission design, and demands precise and reliable tools. However, great computational burden is needed to carry out this task, whose challenges are represented by accurate orbital propagation in the chaotic environment of the n-body dynamics and statistical investigation of events characterised by low probabilities, taking into account uncertainty on the state of the spacecraft and the possibility of random failures. This thesis develops numerical methods with the goal of improving current tools for the verification of compliance to these requirements.

In this chapter the motivations and objectives of this research are presented, along with an overview of the current state of the art in accurate orbital propagation and

uncertainty treatment, focusing on the solutions presented in the available literature. In particular, from the point of view of orbital propagation, the review concentrates on numerical integration schemes for simulations of the n-body dynamics, justifying the attention given to symplectic methods. On the side of uncertainty treatment, instead, the main subjects of the discussion are advanced Monte Carlo sampling methods and covariance propagation techniques.

This chapter introduces the state of the art in these fields, focusing on the available tools used to address the relevant problems, and justifying the choices made in this research. The following chapters will introduce the problems related to the aspects the thesis focuses on, explaining in detail the approaches that were followed, the techniques that were developed and the main results used to validate them.

Finally, a summary of the methodologies developed and implemented in this research is provided.

1.1 Definition of the problem of planetary protection

"The legal basis for planetary protection was established in Article IX of the United Nations Treaty on Principles Governing the Activities of States in the Exploration and Use of Outer Space, including the Moon and other Celestial Bodies (Outer Space Treaty), with the basic goals of: preserving planetary conditions for future biological exploration, and protecting Earth and its biosphere (including the Moon) from potential harmful extraterrestrial sources of contamination. To meet these goals, space flight missions have to control: forward contamination, contamination of celestial bodies other than the Earth by terrestrial life forms in the course of space flight missions, and backward contamination, contamination of the terrestrial biosphere by extraterrestrial life forms in the course of space flight missions." [2]

Planetary protection policy is maintained, updated and promoted by the Committee On Space Research (COSPAR) every few years [3], both as an international standard on procedures to avoid biological contamination in space exploration, and to provide accepted guidelines and requirements in this area as stated in the Outer Space Treaty. Planetary protection policy acts on two aspects of the design of a space mission: at the system engineering level, ensuring the total or partial pre-sterilisation of hardware components on the spacecraft before launch, imposing bioburden (measure of quantity of bacterial spores on exposed surfaces) estimation analyses and procedures to reduce it via cleanroom procedures; at the mission analysis level, accounting for trajectory uncertainty to reduce the probability of impacts between mission-related objects and the protected celestial bodies.

Planetary protection policy distinguishes different categories depending on the class of the missions, reflecting the level of interest and concern that contamination can compromise future investigations. The categories and associated requirements depend on the target body and mission type combinations, with each having a probability and a confidence level to be verified in a given time frame. For every interplanetary mission, a probability of impact analysis on a protected Solar system body shall be performed, taking into account [2, 3]:

- Single/multiple pass analysis;

- Spacecraft reliability;
- Meteoroid impacts;
- Knowledge of spacecraft state (location, velocity vector);
- Manoeuvre and planet/satellite ephemeris uncertainty;
- Stochastic variability of the atmospheric density with the amplitude of the Solar cycle estimated for the mission/sun epoch as variable;
- Scientific evidence of sufficient radiation for sterilisation of terrestrial life forms.

Planetary protection requirements are divided into categories which reflect the level of interest and concern that contamination can compromise future investigations. The categories and associated requirements depend on the target body and mission type combinations, based on the COSPAR classification [2, 3]:

I all missions to bodies which are not object of significant biological interest (e.g. Mercury);

II all missions to bodies which are object of significant biological interest with low chance of compromising future investigation in case of contamination by a spacecraft (e.g. Venus, most natural satellites of the solar system);

III fly-by and orbital missions to bodies which are object of significant biological interest with high chance of compromising future investigation in case of contamination by a spacecraft (e.g. Mars, Europa, Enceladus);

IV surface missions to bodies which are object of significant biological interest with high chance of compromising future investigation in case of contamination by a spacecraft (e.g. Mars, Europa, Enceladus);

V all Earth-return missions.

All categories require different levels of bioburden control and of analysis of the trajectory (outbound and inbound phases).

Some of the requirements adopted in the planetary protection policy of the European Space Agency (ESA) for any exploration mission leaving the Earth's sphere of influence are summarised in Table 1.1. These refer only to the possible contamination due to unplanned impacts occurring during the outer leg of the missions, which create situations where unsterilised particles containing viable terrestrial microorganisms or bacterial spores are released into a protected biosphere, or during the return leg of sample return missions to Earth, where potential extraterrestrial spores may be brought back to our planet in an uncontrolled manner. Similar situations may inadvertently occur also in other kinds of missions not reported in the table, such as surface landings with or without human crew (e.g. a mission to Mars). In these cases the planetary protection requirements focus on the bioburden on the local environment, specifying limits to the number of particles that could be exposed tot the local biosphere [2]. The Earth's Moon does not appear in the Table as it is considered part of the Earth-Moon

system, thus having the same level of protection from backward contamination as the Earth to avoid planetary protection requirements for lunar missions [2].

Notice that not all cases include a requirement on the time frame: while generally missions within the inner solar system ask to verify the possibility of contamination in a period of at least 50 years, missions to the outer solar system do not impose a limitation on it. However, in cases where the verification of the requirements is particularly strict or sensitive to errors, as for orbital propagations in the Jovian system, very extended time frames (up to 1000 years) are commonly considered.

Table 1.1: *Some of the planetary protection requirements adopted by ESA for interplanetary exploration missions.*

Mission	Object	Biosphere	Impact probability	Time
Generic	Any	Any	$\leq 1 \cdot 10^{-3}$	50 years
Mars				
- General	Upper stage	Mars	$\leq 1 \cdot 10^{-4}$	50 years
	Spacecraft	Mars	$\leq (1-5) \cdot 10^{-2}$	20−50 years
- Sample return	Spacecraft	Earth	$\leq 1 \cdot 10^{-6}$	-
Outer solar system				
- General	Any	Subsurface ocean	$\leq 1 \cdot 10^{-4}$	-
- Europa (sample return)	Spacecraft	Earth	$\leq 1 \cdot 10^{-6}$	-
- Small bodies (sample return)	Spacecraft	Earth	$\leq 1 \cdot 10^{-6}$	-

1.2 Research motivations and objectives

The work presented in this thesis focuses on the second aspect of planetary protection as introduced in the previous section, that is the verification of the requirements limiting the probability of collisions of mission-related objects with protected celestial bodies. The main goal of this research is to improve the accuracy and the efficiency of the planetary protection analysis for interplanetary space missions, reducing the complexity which derives from the need to quantify the chance of impacts integrating the trajectories in an n-body dynamics with frequent planetary encounters.

When interplanetary missions leave the Earth's sphere of influence, the launcher upper stages used for their launch may also be injected into orbits that will eventually come back to the Earth or get close to other planets. A notable example of this is the case of the object WT1190F, which was detected in October 2015 on collision path with the Earth [4], and later identified as a man-made object possibly produced during a Moon exploration mission [5].

Moreover, during the missions, random failures of the on-board systems or other accidents (e.g. collisions from debris or micrometeoroids) may make a spacecraft uncontrollable, and leave it on a trajectory that will eventually impact another celestial

body. The same can happen at the end of the mission, after the spacecraft runs out of propellant to control its course or attitude, or after the power systems and batteries fail. This is the main reason behind the end-of-life strategies adopted for missions such as Galileo and Cassini-Huygens: in this cases the orbiters were manoeuvred to plunge into the atmospheres of, respectively, Jupiter (Sep. 2003) and Saturn (Sep. 2017), ensuring their complete burn-up. This choice effectively nullified the risk of colliding with any of the moons of the two planets in the long term and contaminate it with material from Earth [6, 7].

During the design of a mission, the chances of impacts with the Earth or other planets must be studied to verify the compliance with the planetary protection requirements [2], to ensure that the risk of an uncontrolled re-entry in the Earth's atmosphere or of a potential collision with an extraterrestrial habitat and its contamination is reduced below a critical threshold. This problem is commonly approached by studying the evolution of the object's trajectory in the reference time frame, taking into account the uncertainties associated with its state and design parameters as the area-to-mass ratio, errors in the execution of manoeuvres, random failures. However, the way the objects interact with celestial bodies during the long term evolution of its trajectory is often difficult to predict, due to the chaotic nature of the orbits in the n-body problem [8, 9]. For this reason, planetary protections analysis requires precise and reliable tools to propagate trajectories with uncertainty over long times and to predicts impacts with bodies in the solar system.

As already introduced, the main goal of this research is to make the tools currently used in planetary protection analysis more accurate and efficient. For this purpose, the research focused on three primary aspects: numerical orbital propagation, uncertainty sampling, and uncertainty propagation, tested on several applications.

Orbital propagation is studied on a numerical level, with the objective of understanding how errors in a single propagation scale up on a statistical level, that is when thousand of trajectories are propagated to evaluate the probability of impacts, and what their effects are on planetary protection verification. A second target is the improvement of the numerical propagation, with particular attention on the treatment of close approaches with planets, due the their effect of reducing the quality and the accuracy of the integration: for this reason, a novel approach to identify when close approaches occur during the integration will be presented.

The uncertainties characterising the state of the spacecraft are studied initially using a Monte Carlo (MC) approach, where initial conditions are randomly sampled and then propagated to simulate the evolution of the uncertainty and evaluate the probability of possible impacts. In this work, the goal is to improve the sampling process in order to reduce the overall computational effort of the analysis. This is done by introducing an advanced sampling method called Line Sampling, which samples the initial uncertainty distribution in a more efficient way compared with standard MC, and by applying it in multiple calls to estimate the probability of impacts with celestial bodies during different events distributed over a long time. The desired result is to provide an overall overview of the interesting regions within the uncertainty distribution in a way useful for the design of the mission.

Aside from focusing on their sampling, the research also studies the propagation

of uncertainties, with the goal of improving the estimation of impact probability by analysing the evolution of the initial distribution as a whole without the limitations due to the sampling procedure. Since in many cases the uncertainty related to the initial state of spacecraft or launcher stage is expressed through a covariance matrix, the approach that was adopted makes use of Gaussian Mixture Models, which approximate the uncertainty as a weighted sum of Gaussian distributions, and of the Unscented Transformation to propagate it using a fully non-linear dynamic model. A test case is provided to show the application of the techniques for estimating impact probabilities, observing numerical problems related to the selected algorithms. These issues were commented alongside with the main results, and possible solutions were proposed.

The final goal of this research is to combine the techniques presented here to improve the verification of compliance to planetary protection requirements of interplanetary exploration mission. The performance of these techniques will be assessed through numerical simulations in various test cases: Near-Earth Asteroids (due to their well known orbits), and interplanetary missions subject to planetary protection analyses.

1.3 State of the art

1.3.1 Accurate orbital propagation

When numerically integrating an initial value problem, the choice of the integration scheme affects how the error deriving from the numerical integration accumulates time step after time step, and, thus, the eventual accuracy of the computation [10]. In particular, the integration error growth sets the limit to the length of any integration, as long as it is required that the final computed positions are still causally related to the initial conditions [11]. This is true in particular for strongly non-linear problems, such as the study of long term n-body orbital dynamics, due to the complexity of the system, the number of terms involved, and its chaotic behaviour [8, 9].

One of the contributing factors to error growth in long term integration is the fact that most integration schemes do not consider that the n-body systems have quantities that are conserved during the motion, such as the total mechanical energy and the total angular momentum, and have no information about the conservation laws. When these integration methods are used, a variation of these quantities is observed, which is a phenomenon that is not coherent with the physical formulation of the problem. Geometry preserving numerical integration methods attempt to introduce conservation laws into the system to reduce the error growth rate. Examples of such methods include symplectic methods and manifold projection methods [12]. While non-symplectic integrators distort the orbits being propagated, symplectic integrators preserve the symplectic structure of the problem, with no long-term build-up of energy error [12]. For this reason they are often chosen for studying problems involving planetary or satellite systems.

Despite improving the qualitative behaviour, symplectic methods do not guarantee a more precise solution. Since symplectic algorithms have fixed-step formulations, dealing with close encounters can become difficult due to the faster dynamics which requires shorter time steps to preserve the accuracy of the integration as it was before the encounter. However, changing the step-size of a symplectic integrator in order to

preserve the accuracy of the overall integration introduces an error with each change [13].

Several symplectic integration schemes and tools based on them have been proposed in the last decades. The methods by Yoshida [14] and the SABA methods by Laskar and Robutel [15] are high-order symplectic schemes for perturbed Hamiltonian systems used for the long term study of the Solar System dynamics. For the same application, Chambers proposed a symplectic integrator capable of accounting for close encounters between massive bodies thanks to a hybrid formulation between symplectic and non-symplectic schemes [16] (the integrator is included in the MERCURY software package). Similarly, the SyMBA integrator by Duncan et al. [17] uses a multiple time step technique to deal with close encounters while maintaining good computational efficiency. Another package of mixed symplectic and non-symplectic integration methods was developed Levison and Duncan under the name of SWIFT [18–20]. REBOUND, by Rein and Tamayo [21] also uses symplectic (SABA and Wisdom-Holman among them) and non-symplectic methods to integrate the motion of particles under the influence of gravity.

On a different perspective, non-symplectic methods can ensure great accuracy in approaching the strongly non-linear orbital problem, despite not explicitly having a conservative formulation.

Runge-Kutta (RK) methods are some of the most used numerical schemes, thanks to their relatively simple formulation even at high-orders and flexibility to solve difficult problems [22] even in explicit form. In particular, one of their main advantages is the possibility to define embedded schemes to adapt the times step and ensure great accuracy [23–25]. Also, particular schemes exist that can be made symplectic with a proper choice of the coefficients, a property that will be explained in more detail and exploited in Chapter 2. One alternative to RK methods are the high-order implicit schemes based on Gauss collocation methods developed by Everhart, making use of truncated time series in time and obtaining more accurate and efficient results [26, 27].

Other than the choice of the integration scheme, the propagation can be made more accurate also by acting on the equations to eliminate singularities. The regularisation of equations is a process that consists in changing the dependent and independent variables, so that the dynamics are described by a set of equations that are non-singular. Moreover, time-regularisation yields more uniformly spaced integration steps, introducing an automated integration step size adaptation mechanism, thus improving accuracy and computational cost of the propagation. In particular, the Sundman transformation replaces the physical time with a fictitious time that is proportional to the eccentric anomaly of the orbit [28, 29]. Furthermore, the Kustaanheimo-Stiefel (KS) regularisation converts the equations of motion into a high-dimensional harmonic oscillator [30], as an extension of the Levi-Civita transformation to the 3D case [31].

More recently, the Group of Space Dynamics of UPM (GSD-UPM) developed the DROMO regularisation scheme [32], which exhibits a higher accuracy when compared with other propagation schemes. This method shows itself particularly apt to high fidelity long term propagation, as in the case of the propagation of Near Earth Objects (NEO's) orbits. Further work introduced different time scales to increase the stability

of the regularisation when dealing with close approaches [33], and studies of the long term effects of perturbations [34].

1.3.2 Uncertainty sampling and impact probability analysis

Current approaches for robust detection and prediction of planetary encounters mainly refer to linearised models [35] or full non-linear approaches to orbital sampling [36]. The uncertainty in the determined orbital state, the length of the time window and the possibility of close approaches with other planets between the observation epoch and the epoch of the expected impact are the main factors driving the choice of the approach to the problem. Simplified models are generally preferred when linear approximations are reliable for both the orbit determination and uncertainty propagation, and while they can significantly reduce the required computational burden, their range of application can be very narrow. The application of linear methods in the impact plane was introduced by Chodas [37].

When the simplifying assumptions are not valid, fully non-linear techniques are required in order to obtain results that are reliable and coherent with the true physics of the problem: among these, MC methods are the most accurate but also the most computationally intensive, since the number of evaluations needed to verify the required probability level grows when greater accuracy is desired [38]. Given the non-linear and chaotic behaviour of the orbital propagation problem, MC simulations are preferred to address this kind of problem thanks to their general and flexible way of approaching collision and impact probability estimation [39, 40]. This approach is based on the generation of virtual impactors via observation of random sampling of an initial distribution and the integration over the time interval of investigation using fully non-linear equations [41, 42].

As said, in cases where long-term propagations are necessary and multiple close approaches with planets are expected, MC techniques represent the best choice to address the problem of estimating impact probabilities. These techniques are intensively applied for the prediction of impacts of NEOs with the Earth [43]. Since these objects are continuously detected, often while they are already approaching the Earth, it becomes necessary to estimate accurately and in a short time whether a collision will occur, and the likelihood of it. However, despite their higher fidelity to non-linear models, standard MC simulations may not be suitable for fast NEO impact probability estimation, since they generally need numerous evaluations to achieve high accuracy. An elegant and effective compromise was introduced with the concept of the Line Of Variations (LOV) [44]: in this case, Milani et al. applied the multiple solutions approach to sample the central line of variations (1-dimensional) of the non-linear 6-dimensional confidence region at the initial epoch and then numerically integrate over the time span of interest in a similar way, and integrated it in the CLOMON2 [1] monitoring system operated by the Universities of Pisa (Italy) and SpaceDyS. With respect to standard MC, the LOV method guarantees compute times 3-4 orders of magnitude lower than those required in MC simulations, though the LOV analysis may grow quite complex after it has been stretched and folded by multiple close planetary encounters [45]. However,

[1] `https://newton.spacedys.com/neodys/`, see the Risk Page. [last accessed 15 Nov 2019]

various efforts are still being made to refine the work on the LOV: for example, Tommei extends the LOV to the 2-dimensional case when the observational arc of the asteroids are short [46], while Valsecchi et al. focus on studying analytically the effects of close approaches on the LOV [47].

In a similar way, these methods are applied to planetary protection analysis, which requires high accuracy to verify that the design of an interplanetary mission is compliant to the international guidelines [5, 48–50]. In particular, Colombo et al. and Jehn et al. exploit the expression of the confidence interval by Wilson [51] to estimate in advance the number of MC runs necessary to grant a desired confidence level (as requested by planetary protection policy).

In all the cited applications, more efficient sampling methods may increase the precision of the probability estimate, or reduce the amount of simulations, and thus the computational cost. Aside from the LOV method, in recent times new advanced MC techniques, such as the Importance Sampling (IS) [52], Line Sampling (LS) and Subsets Simulation (SS) methods were developed [53], aiming at reducing the computational burden by either restricting the sampling phase space or identifying optimal sampling paths within it: these approaches are also based on alternative ways to sample the uncertainty space, and offer competitive results in both fields, providing a significant improvement with respect to standard MC performance while maintaining a sufficiently high level of accuracy. Alternative solutions approach the problem from other perspectives, such as exploiting the variation of the Minimum Orbit Intersection Distance (MOID) to predict encounters [54], mapping on the b-plane [41, 55–57], or the use of Differential Algebra [53, 58, 59] to represent the propagated uncertainty in more manageable ways.

1.3.3 Uncertainty propagation techniques

The main issue in assessing the risk of impacts between small objects and celestial bodies (whether for planetary protection analysis or asteroid impact monitoring) is the large amount of uncertainty that is intrinsic in the problem. When quantifying the initial state of an object, uncertainty in its trajectory arises from measurement errors or approximations of the physical model, due to lack of knowledge or simplifications.

In the context of space mission analysis, uncertainty propagation usually refers to the orbital uncertainty propagation, that is to determine the satellite's probability density function (pdf) or state moments. Generally, it is assumed that the probability distribution of the deviation from the mean state can be initially represented by a Gaussian distribution, with a mean and a covariance matrix, as typical of navigation uncertainties in orbital uncertainty propagation problems. However, the Gaussian error hyper-ellipsoid gradually becomes non-Gaussian during the propagation, due to the non-linear nature of dynamics. For this reason, estimating its evolution at a future time is not straightforward.

The time evolution of a pdf is described by the Fokker–Planck equation (FPE) [60]. Since solving the FPE for high dimensional dynamic system is very difficult, orbital uncertainty propagations are usually addressed by linear models or non-linear MC simulations [61]. However, linear problems do not ensure high efficiency over long-term propagations, and MC methods, while providing high precision, become computation-

ally expensive as the required accuracy increases. For these reasons, different analytical, semi-analytical, or numerical non-linear methods have been developed in recent years.

The Unscented Transformation (UT), originally proposed by Julier et al. [62, 63], approximates the mean and covariance of a Gaussian distribution by considering a set of deterministically chosen weighted sigma-points which are selected such that the distribution is exactly captured by the sigma-points. The sigma-points are then evolved thorough the non-linear transformation to obtain the mean and covariance describing the new state. Instead of random samples, the UT method uses no more than $2n + 1$ sigma-points for efficient and accurate uncertainty propagation, where n is the dimensionality of the system.

On a similar note act Gaussian Mixture Models (GMM), which were introduced by Garmier et al. and by Terejanu et al. in 2008 [64, 65] for uncertainty propagation and then developed further by Giza et al. [66, 67], De Mars et al. [68], and Vittaldev and Russel [69] with specific application to space debris. Frey et al. [70] also applied GMM to the study of space debris using the continuity equation to model the fragment density as a continuum and propagate it forward in time. The idea at the base of GMM is to represent the distribution of the quantity of interest with a weighted sum of Gaussian distributions: the mean value and covariance of the distribution are sufficient to describe its evolution, and can be updated via application of the Unscented Transformation or Unscented Kalman Filter. Further work was then carried out to optimise the weights of the GMM components and adapt them during the propagations.

Polynomial chaos expansions (PCE) methods work differently from UT and GMM, as they provide knowledge of the state pdf and its moments at orders higher than mean and covariance. Wiener first proposed a method where series approximations using standard random variables represent both input uncertainty and the output uncertainty of the system under consideration [71]. The series expansion consists of polynomials of the corresponding multi-dimensional random variable defined on a basis of orthogonal functions, and its coefficients are recovered by first propagating a few points and then interpolating them with a least square approach or exploiting the orthogonality of the basis functions. The PCE method does not require any simplifications of the dynamic model, meaning it can be easily applied to fully non-linear orbit uncertainty propagation problems, as first presented by Jones et al. [72].

A common disadvantage of the GMM and PCE methods is that they both suffer from the curse of dimensionality: as they are both sample-based methods, both the number of Gaussian mixtures to be propagated and the number of terms of PC polynomials grow as the dimensions of the problem grow, thus increasing the computational load to reach adequate accuracy.

Other methods, instead, exploit analytical or semi-analytical approximations for uncertainty propagation.

Taylor series can be used to expand the solution as function of the nominal initial conditions of a trajectory and approximate the non-linear dynamics through automatic differentiation or analytical derivatives [73]. The Taylor expansions are used to approximate the non-linear motion locally and to map the initial uncertainties to the new values

analytically. Methods using State Transition Matrix (STM) developed starting from the 1st order of the expansion have high simplicity and computational efficiency, but fail to provide sufficient accuracy in case of highly non-linear systems, long-duration uncertainty propagation, or large initial uncertainty. A method obtained from the higher order terms of the Taylor expansion (State Transition Tensors, STT) was proposed by Park and Scheeres [73], but complexity arises from the partial derivatives of high orders and differentiation is not possible when singularities and discontinuities are present.

Different from the STTs methods, Taylor Algebra replaces real algebra with operations among Taylor polynomials. From this, Berz developed Differential Algebra (DA) [74] which can expand any function into its Taylor polynomials up to an arbitrary order, providing easy evaluation and differentiation, allowing to automatically expand the flow of the dynamics up to an arbitrary order and to non-linearly map the uncertainty with respect to the initial conditions. Armellin and Di Lizia [75] developed an accurate non-linear uncertainty propagator and applied it to asteroid encounters, Wittig et al. applied it to the propagation of large uncertainty sets through automatic domain splitting [76], Morselli et al. employed it for orbital conjunctions analysis [53]. However, also the DA technique requires the dynamics to be continuous and differentiable.

1.3.4 SNAPPshot tool suite

Past work at the University of Southampton has developed SNAPPshot (Suite for the Numerical Analysis of Planetary Protection) under a contract for the European Space Agency [5,56,57]. The purpose of SNAPPshot is to verify whether a mission is compliant with the planetary protection requirements for a given confidence level, considering the launcher dispersion and the distribution of additional parameters such as the area-to-mass ratio. MC analysis is exploited to study the evolution of the trajectory and its uncertainty in the considered time frame, and to estimate the probability of impacts with major celestial bodies.

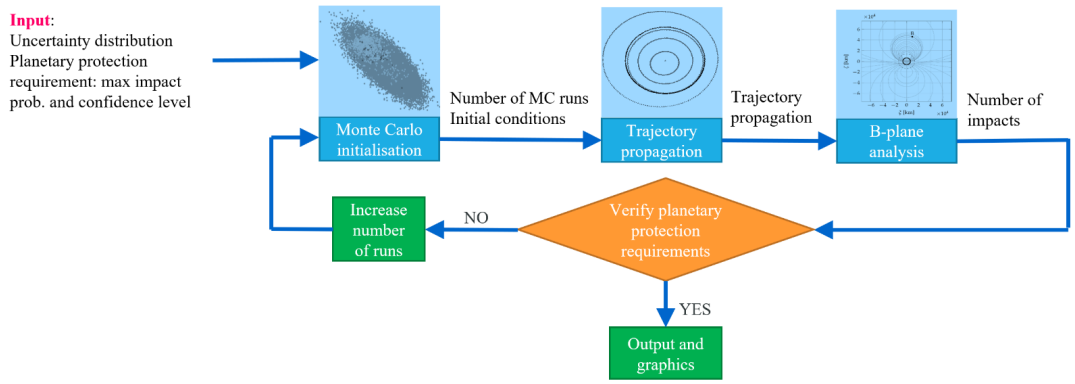

Figure 1.1: *SNAPPshot building blocks.*

Fig. 1.1 shows a block diagram of SNAPPshot in the original version that was delivered to ESA, written in Modern Fortran. The user specifies the maximum allowed probability of impact with a specific body and the desired confidence level, together with providing the initial uncertainty distribution (which can represent a failure in the

propulsion system, a distribution in are-to-mass ratio of the satellite, or the covariance matrix representative of the launcher injection error). The tool computes the required number of MC runs to ensure the desired confidence level by applying the expression of the confidence interval by Wilson [51] as in Jehn [48] and Wallace [49]. It then samples the distribution to obtain the initial conditions, which are propagated for a given amount of time (usually 100 years) using high-order Runge-Kutta methods with different possible ways to adapt the time-step. Each trajectory is then analysed with the representation on the b-plane of the relevant bodies, and the number of detected impacts is used to compute the probability of impact with the target planets with a given level of confidence: if the number is not compatible with the planetary protection requirements, the number of MC runs is increased until the requirements are fulfilled or the maximum number of runs is reached [5].

The work on SNAPPshot has been continued at Politecnico di Milano as part of this research with funding from the European Research Council (ERC) under the European Union's Horizon 2020 research and innovation programme as part of project COMPASS (Grant agreement No 679086), and from the European Space Agency (ESA) though a Networking/Partnering Initiative (NPI) agreement. The novel techniques presented in this thesis (along with several other modifications aimed at making the analysis more flexible) have been implemented in it and tested, applying the software to interplanetary mission cases during three stays at the European Space Operations Centre (ESOC) under the supervision of Dr. José Manuel Sánchez Pérez as technical advisor. These techniques will be introduced and explained in detail in the following chapters, providing also test cases and numerical results use for their validation.

The final version of the tool will be tested by the Mission Analysis team of ESA on several space missions such as Mars Sample Return and JUICE.

1.4 Methodologies developed and implemented

As already introduced, the research focuses on three aspects of planetary protection analysis (numerical orbital propagation, uncertainty sampling, and uncertainty propagation) with the goal of improving its accuracy and efficiency. This was done by developing various numerical methods, implementing them in the SNAPPshot tool, and by validating their effectiveness in the application to different interplanetary mission cases.

In particular, the numerical propagation was studied by selecting a number of integration schemes, implementing them and comparing their performance in terms of accuracy and efficiency in different test cases ranging from the propagation of NEOs orbits to actual interplanetary missions. The study mostly focused on high-order RK and symplectic schemes: the first ones were chosen due to their simplicity [22], taking advantage of the methods already implemented in SNAPPshot, the latter due to their formulation preserving the physical aspects of the dynamics, such as total mechanical energy of the system [14, 77, 78]. In relation with symplectic scheme, the projection method was also implemented: this numerical technique, which forces the conservation of the integrals of the motion even in schemes that are not symplectic [12], was chosen as an alternative to symplectic methods to allow the conservation of the total energy.

Moreover, a novel technique for the identification of close approaches with massive bodies was devised. The main motivation behind it was the need to reduce the impact fly-bys on the numerical integration of a trajectory, due to the faster and more chaotic dynamics governing the motion during such occurrences, as will be shown in Chapter 2. The method exploits the knowledge of the dynamics to estimate during the propagation when a close approach is occurring, that is when it will have the highest impact on the numerical accuracy. This is done by considering the eigenvalues of the Jacobian matrix derived from the equations of motion, which were easily recovered since they were already utilised in SNAPPshot for the adaptation of the time step during the integration, following the method proposed by Debatin et al. [79]. Results will show that this approach gives a wider definition of close approach with respect to the used of a fixed distance to define it (e.g. the radius of the sphere of influence of the approached planet).

Regarding uncertainty sampling, the work presented here focused on finding ways to improve the performance of the statistical analysis needed to verify planetary protection requirements. After different comparisons with standard MC and Subset Simulation, the Line Sampling method was chosen as alternative to standard MC simulation due to its higher accuracy in evaluating small probabilities, as often required in this kind of problem [80, 81]. The LS algorithm was implemented in SNAPPshot and applied to impact probability analysis for asteroids and exploration missions to validate its efficiency in the case of single impact events (other application to single events already exist in the available literature for in-orbit conjunction analysis [53]). Later, other algorithms were devised and added to the tool, with the goal of improving the results obtained in the previous analyses: on one side, a way to obtain a choice of the main sampling direction closer to the ideal case was introduced, which improved the accuracy of the probability estimation with respect to previous results; on the other side, an algorithm to identify, via a preliminary MC sampling, which time intervals were potential candidates to find an impact region to probe using LS. These additional algorithms were used to improve the impact probability analysis and make it applicable to cases where multiple impacts events can be found in long time intervals.

Finally, the research focused on uncertainty propagation techniques for the propagation of the covariance representing the initial state dispersion of the object being propagated. An approach based on Gaussian Mixture Models was selected to approximate the covariance as a weighted sum of Gaussian distributions during the propagation. The propagation itself was carried out using the Unscented Transformation, which does not relies on approximations of the dynamics, but exploits the fully non-linear n-body model. Moreover, splitting techniques were used during the propagations to contain the effects of the non-linear dynamics and be able to maintain a Gaussian description of the propagated elements. However, the numerical simulations showed the presence of problems related to the splitting algorithm for the absence of control techniques to maintain the accuracy of the overall uncertainty approximation. Possible solutions to this issue and improvements of the selected algorithm are discussed in Chapter 4.

1.5 Thesis organisation

This thesis is divided into six chapters, which introduce different aspects of the research on orbit propagation and uncertainty modelling for planetary protection compliance verification. The first part of each chapter explains the theoretical development and the method adopted, subsequently some results are presented as the application of the theory. The thesis is organised as follows.

Chapter 2 presents the integration methods that have been analysed, implemented, and applied to orbital propagation. The construction and the properties of the integration schemes are shown, explaining the reasons for their choice, and are later applied in Section 2.4 to compare them in various applications. The chapter also introduces a new dynamics-based algorithm to detect close approaches during the propagation, with the aim of identifying the conditions increasing the numerical error of the trajectory integration.

Chapter 3 focuses on the Line Sampling method, which is introduced as an alternative to standard MC simulation to estimate impact probabilities with higher accuracy and efficiency. The first part of the chapter is devoted to the explanation of the base algorithm and its theoretical formulation, which is later extended to better characterise the accuracy of the method in various situations. In the second part, instead, new algorithms exploiting LS are presented and then applied in planetary protection analysis of interplanetary missions in Section 3.3.

Chapter 4 focuses on techniques for the direct propagation of an uncertainty distribution, particularly on the propagation of covariances making use of the Gaussian Mixture Model approach with adaptive splitting. The methods that were chosen and then implemented are presented from the theoretical point of view, and then their performance on the numerical level is studied when applied to planetary protection analysis in Section 4.4.

Chapter 5 presents a breakdown of the work done on the SNAPPshot tool, introducing the original functionalities of the software and presenting the algorithms that were introduced as part of the PhD research, along with an outline of the modifications implemented in the code.

Finally Chapter 6 summarises the finding of this research and gives an insight into possible further developments of this study that will be subject of future work.

1.6 Contributions and publications

Some of the contents of this dissertation have been presented during various international conferences, and have been submitted for review to scientific journals or are about to be submitted.

Journal publications

- Romano M., Losacco M., Colombo C., Di Lizia P., “Impact probability computation of Near-Earth Objects using Monte Carlo Line Sampling and Subset Simulation", unpublished manuscript, submitted for 2^{nd} review Jan. 2020 to Celestial Mechanics and Dynamical Astronomy, currently under second review

- Romano M., Colombo C., Sánchez Pérez J. M., "Assessment of integration methods for application to planetary protection analysis", unpublished manuscript, submitted for review to Acta Astronautica in Jan. 2020
- Romano M., Colombo C., Sánchez Pérez J. M., "Line Sampling procedure for extensive planetary protection analysis", unpublished manuscript, submitted for review to Journal of Guidance, Control, and Dynamics in Jan. 2020

Conference proceedings

- Romano M., Colombo C., Sánchez Pérez J. M., "Verification of planetary protection requirements with symplectic methods and Monte Carlo Line Sampling", Proceedings of the 68th International Astronautical Congress (IAC), Sep. 25th-29th 2017, Adelaide, Australia, IAC-17-C1.9.5
- Romano M., Colombo C., Sánchez Pérez J. M., "Efficient planetary protection analysis for interplanetary missions," Proceedings of the 69th International Astronautical Congress (IAC), Oct. 1st-5th 2018, Bremen, Germany, IAC-18-A3.5.10
- Losacco M., Romano M., Di Lizia P., Colombo C., Morselli A., Armellin R., Sánchez Pérez J. M., "Advanced Monte Carlo Sampling Techniques for Orbital Conjunctions Analysis and NEO Impact Probability Computation", Proceedings of the 1st NEO and Debris Detection Conference, Jan. 22nd-24th 2019, ESA/ESOC, Darmstadt, Germany
- Masat A., Romano M., Colombo C., "Orbital resonance analysis in Monte Carlo simulations for planetary protection and defence", Proceedings of the XXV AIDAA International Congress, Sep. 9th-12th 2019, Rome, Italy

Presentations (not included in conference proceedings)

- Romano M., Losacco M. Colombo C., Di Lizia P., "Estimation of impact probability of asteroids and space debris through Monte Carlo Line Sampling and Subset Simulation", 3rd international workshop on Key Topics in Orbit Propagation applied to Space Situational Awareness (KePASSA), Jul. 25th-27th 2017, ESA/ESTEC, Noordwijk, The Netherlands
- Romano M., Colombo C., "Planetary protection analysis for interplanetary missions", Satellite Dynamics and Space Missions Summer School, Aug. 28th - Sep. 2nd, 2017, San Martino al Cimino, Italy
- Romano M., Colombo C., Sánchez Pérez J. M., "Line sampling procedure for extensive planetary protection analysis", 4th international workshop on Key Topics in Orbit Propagation applied to Space Situational Awareness (KePASSA), Apr. 24th-26th 2019, Universidad de la Rioja, Logrono, Spain

CHAPTER 2

Numerical integration methods for n-body propagation

2.1 Introduction

Planetary protection requirements are set to limit the chance of impacts between uncontrollable mission-related objects (launcher upper stages or damaged spacecraft) and other celestial bodies for any interplanetary mission, with with the possibility of additional constraints over the considered time frame [2]. The verification of the requirements leads to the need of propagating the initial state of these objects over periods of 50 years at least. This is, however, a non-trivial task: the non-linearity of the dynamics, the modelling of non-gravitational perturbations (and other small effects), the uncertainty in the ephemerides of the solar system bodies, and the eventual close approaches with them affects the long-term evolution of the trajectories. As a consequence, predicting the actual position of the launcher stage or debris over periods up to 100 years, and whether an impact with a sensitive target will occur or not, becomes difficult [5,48]. This is even more complex when propagating the dynamics in environment such as the Jovian system, which presents challenges from the numerical point of view due to the fast dynamics, which emphasises the chaotic aspect of the problem.

As no analytical solution for the gravitational n-body problem exists without introducing simplifying hypotheses, the orbital propagations have to be carried out numerically, in a dynamics with frequent close approaches of massive bodies; this heavily affects the numerical integrations of the trajectory, whose uncertainty increases over time. Moreover, the representation of the spacecraft state may in some cases become unreliable due to accumulating numerical errors during long integrations, which affect not only the accurate estimation of the state, but also introduce variations in the conserved quantities of the motions which are not coherent with the physical laws in the

form of fictitious dissipation of the total energy of the system [12]. The quality of the numerical integration is commonly improved by using high order integration methods, but alternative schemes may be necessary to ensure a better long term accuracy with respect to the existing methods without compromising the computational efficiency.

This chapter analyses the process of numerical integration, to understand how the errors in a single propagation affect the overall verification of the planetary protection requirements, and to improve the accuracy of the numerical propagation in an n-body environment.

The first issue is addressed from two points of view. First, single propagations of known cases are studied by integrating the trajectories with different schemes and comparing the results among them and with the reference data, to reveal how the selected methods deal with the chaoticity of the n-body dynamics. Then, Monte Carlo (MC) analyses are performed, to quantify how the errors in the propagation of a single orbit weight on a statistical level when thousands of trajectories are integrated with the goal of estimating the probability of impact with a celestial body. The integration methods under examination include symplectic methods and other energy-preserving techniques: the formulation of these methods includes the conservation of total energy (or other constants of the motion) when a Hamiltonian description of the dynamics is given, thus granting, on long integration times, a numerical solution that is closer to the true physical behaviour of the system, and eventually a higher accuracy.

Alongside these analyses, this work also presents a novel method to identify the occurrence of close approaches during the integration, based solely on the dynamics of the problem, in order to address the numerical issues caused by fly-bys in a more effective way. This is done by considering the Jacobian of the equations of motion and the evolution of its eigenvalues in time to identify when a close approach is occurring, and thus when it starts affecting the numerical integration, without relying on a definition based on a fixed distance (e.g. radius of the sphere of influence).

In the chapter, the theory behind the different integration techniques is first explained, then applied to various test cases in numerical simulations. These tests are used to compare the performance of the selected integration methods in terms of accuracy and computational cost, and to show how their choice affects the results of a planetary protection analysis. The test cases include:

- the propagation of known orbits of Near-Earth Asteroids (99942 Apophis, 2010 RF_{12}, and 2007 UD_6), which are used as reference to validate the implemented integration methods and to quantify the effects of close approaches on the energy conservation and on the numerical error during the integration;
- the planetary protection analysis for the launcher upper stages of the Bepi Colombo mission and of the Solar Orbiter mission, to study the effect of the choice of the integration methods on the results of a statistical analysis (that is the value of the impact probability).

Note that the planetary protection analyses are carried out using a MC approach, as already introduced in section 1.3.1 of Chapter 1: the initial conditions are generated by randomly sampling a covariance matrix representing the uncertainty distribution over the initial state of the considered object, and then propagated using the proposed

integration methods. Finally, the impact probability is estimated as the fraction of the total number of propagated trajectories leading to a collision with a celestial body.

Finally, the trajectory of the launcher stage of Solar Orbiter and the trajectory of the JUICE spacecraft will be used to validate the Jacobian-based method for the identification of close approaches during the propagation.

2.2 Equations and constants of the motion

Before starting the overview of the selected numerical methods, the definitions of the equations of motion is given. Two sets of equations are used: the restricted n-body problem (RNBP), describing the motion of a particle subjected to the gravitational forces of n celestial bodies; the complete n-body problem (NBP), which instead describes the motion of n massive bodies subjected to each other's gravitational forces. Along with the equations, this section also provides the definitions and the expressions of the the Hamiltonian functions associated with each formulation of the gravitational n-body problem since it represents one of the conserved quantities of the motion. All the equations and constants presented here are defined in Cartesian coordinates with respect to an inertial reference frame centred in the Solar System barycentre.

Restricted n-body problem

In this model, only the gravitational forces of the n celestial bodies acting on the object whose trajectory is being propagated are considered, not the effects on the bodies on each other. This corresponds to the simplification that the n-body dynamics is restricted, i.e., the $n-1$ bodies act on the dynamics of the body to be integrated but its mass do not influence the motion of the other masses. Therefore, the dynamics of the other $n-1$ masses can be integrated off-line and included in the propagation through the ephemerides as a function of time.

The equations of motion are reported in Eq. 2.1 in an inertial barycentric reference frame [82, pp. 29–32]:

$$\begin{cases} \dot{\mathbf{r}} = \mathbf{v} \\ \dot{\mathbf{v}} = -\sum_{j=1}^{n} \mu_j \frac{\mathbf{r}-\mathbf{r}_j(t)}{\|\mathbf{r}-\mathbf{r}_j(t)\|^3} \end{cases} \tag{2.1}$$

with $\mathbf{r}$ and $\mathbf{v}$ being, respectively, the position and velocity vectors of the propagated body, $\mathbf{r}_j$ the position of the j-th planet and μ_j its gravitational parameter.

The Hamiltonian function $\mathcal{H}$, which represents a measure of the total mechanical energy of the system, is explicitly dependent on time, as planetary ephemerides $\mathbf{r}_j(t),\ j = 1, ..., n$ are imposed as a function of time:

$$\begin{cases} \mathcal{H}(\mathbf{r}, \mathbf{v}, t) = \frac{1}{2}\|\mathbf{v}\|^2 - \sum_{j=1}^{n} \frac{\mu_j}{\|\mathbf{r}-\mathbf{r}_j(t)\|} \\ \frac{\mathrm{d}\mathcal{H}}{\mathrm{d}t} = \frac{\partial \mathcal{H}}{\partial t} = f(\mathbf{r}_j(t)) \neq 0 \end{cases} \tag{2.2}$$

where $\partial[\cdot]/\partial t$ represents the partial derivative with respect to the time t, while $\mathrm{d}[\cdot]/\mathrm{d}t$ represents the total derivative.

The Hamiltonian function can be made a constant of the motion by extending the phase space: the problem is reformulated in such a way the Hamiltonian does not

explicitly depend on time any more, as a new system evolution parameter s is introduced [83]; this makes it possible to rewrite the time t as an additional coordinate $\tau(s)$ with its own conjugate momentum $u(s)$ [84, pg.20-21]. The new Hamiltonian is thus written as

$$\begin{aligned}\mathcal{K}(\mathbf{r}(s),\tau(s),\mathbf{v}(s),u(s)) &= \mathcal{H}(\mathbf{r},\mathbf{v},\tau)+u \\ &= \frac{1}{2}\|\mathbf{v}\|^2-\sum_{j=1}^{n}\frac{\mu_j}{\|\mathbf{r}-\mathbf{r}_j(s)\|}+u\end{aligned} \tag{2.3}$$

Analytically, the new defined Hamiltonian $\mathcal{K}$ does not explicitly depend on time [84, pg.20-21]. Also, the equations describing the variation of the orbital state (position $\mathbf{r}$ and velocity $\mathbf{v}$) maintain the same form as in Eq. 2.1, while two new equations are added to the system:

$$\begin{cases}\frac{\mathrm{d}\mathbf{r}}{\mathrm{d}s}=\frac{\partial\mathcal{K}}{\partial\mathbf{v}}=\mathbf{v}\\ \frac{\mathrm{d}\mathbf{v}}{\mathrm{d}s}=-\frac{\partial\mathcal{K}}{\partial\mathbf{r}}=-\sum_{j=1}^{n}\mu_j\frac{\mathbf{r}-\mathbf{r}_j(s)}{\|\mathbf{r}-\mathbf{r}_j(s)\|^3}\\ \frac{\mathrm{d}\tau}{\mathrm{d}s}=\frac{\partial\mathcal{K}}{\partial u}=1\\ \frac{\mathrm{d}u}{\mathrm{d}s}=-\frac{\partial\mathcal{K}}{\partial\tau}=\sum_{j=1}^{n}\mu_j\frac{(\mathbf{r}-\mathbf{r}_j(s))\cdot\mathbf{v}_j(s)}{\|\mathbf{r}-\mathbf{r}_j(s)\|^3}\end{cases} \tag{2.4}$$

The third equation has the trivial solution $\tau = s = t$ (except for a constant), so that the equations of motion for $\mathbf{r}$ and $\mathbf{v}$ given by $\mathcal{K}$ are identical to those given by the Hamiltonian $\mathcal{H}$. Substituting this solution in the fourth equation, one obtains:

$$\frac{\mathrm{d}u}{\mathrm{d}s}=-\frac{\partial\mathcal{K}}{\partial\tau}=-\frac{\partial\mathcal{H}}{\partial\tau}=-\frac{\partial\mathcal{H}}{\partial t} \tag{2.5}$$

which, when integrated, shows that u is equal to the negative *value* $-H(t)$ of the system's Hamiltonian $\mathcal{H}(\mathbf{r}(t),\mathbf{v}(t),t)$ [83]:

$$u=-K(\tau)=-H(t) \tag{2.6}$$

This operation has two main advantages: first, a true constant of motion is defined, being $\mathcal{K}(\mathbf{r},\tau,\mathbf{v},u)=\mathcal{H}(\mathbf{r},\mathbf{v},t)+u=\mathcal{H}(\mathbf{r},\mathbf{v},t)-H(t)=0$; second, the canonical form of the Hamiltonian is recovered, with the possibility to apply other canonical transformations (meaning a transformation that preserves the Hamiltonian form of the equations of motion [84, pg.22]) or symplectic integration schemes.

Complete n-body problem

In this model, all the gravitational forces of the objects being propagated (celestial bodies and particles) acting on each other are considered.

The equations of motion expressed in an inertial barycentric reference frame are:

$$\begin{cases}\dot{\mathbf{r}}_i=\mathbf{v}_i\\ \dot{\mathbf{v}}_i=-\sum_{j=1,j\neq i}^{n}\mu_j\frac{\mathbf{r}_i-\mathbf{r}_j}{\|\mathbf{r}_i-\mathbf{r}_j\|^3} \quad i=1,...,n\end{cases} \tag{2.7}$$

In Eq. 2.7 all the gravitational forces acting on the i^{th} body due to the other $n-1$ masses with gravitational parameters $\mu_j, j=1,...,n-1$ are considered and added up.

The Hamiltonian of the system is not dependent on time, and is equal to the total energy of the system:

$$\begin{cases} \mathcal{H}(\mathbf{r}_1, ..., \mathbf{r}_n, \mathbf{v}_1, ..., \mathbf{v}_n) = \frac{1}{2}\sum_{i=1}^{n} m_i \|\mathbf{v}_i\|^2 - \mu_i \sum_{i=1}^{n}\sum_{j=1}^{i-1} \frac{m_i m_j}{\|\mathbf{r}_i - \mathbf{r}_j\|^3} = E_0 \\ \frac{\mathrm{d}\mathcal{H}}{\mathrm{d}t} = \frac{\partial \mathcal{H}}{\partial t} = 0 \end{cases} \tag{2.8}$$

In this case, the motion of all the celestial bodies and other objects is represented by a set of equations with the same form as Eq. 2.1, repeated for each propagated object.

2.3 Selection of integration methods and energy preservation techniques

This section shows a selection of integration methods that were chosen and then implemented for this work and provides explanations of how the numerical schemes are defined.

First, a general introduction of the properties that were considered will be made, in order to introduce the terminology and the most important aspects of the numerical methods. Considering a generic initial value problem

$$x'(t) = f(x,t), x(t_0) = x_0$$

a single-step numerical integration method computes the value of the generic dependent variable x at time $t_{n+1} = t_n + h$, where h represents the step size, according to the scheme Φ_h as $x_{n+1} = \Phi_h(x_n)$. The properties of the scheme can be defined using the notation here introduced [22]:

- the order of the integration method (the numerical method has order p if for any sufficiently smooth solution of the initial value problem, the local truncation error is $O(h^{p+1})$);
- the number of stages, that is equal to the number of evaluations of the function f required to advance one step;
- whether it is explicit (meaning that the evaluation of the integration formula is sufficient for each integration step, or formally $x_{n+1} = \Phi_h(x_n)$) or implicit (meaning that it is necessary to solve an implicit equation or system or equations, or formally $x_{n+1} = \Phi_h(x_{n+1}, x_n)$);
- whether the step size h is fixed (in case the step size is constant during the integration) or variable (in case the step size is controlled);
- whether it is symplectic (meaning that the advancement of a time step is defined as transformation that preserves the Hamiltonian form of the equations of motion [84, pg.22]) or not.

All the methods shown ahead are single step, meaning that for the calculation of x_{n+1} depends only on x_n $\forall n \geq 0$.

Table 2.1 shows the numerical integration methods that were chosen and then implemented for this work, highlighting their properties as defined above. The methods include:

- standard Runge-Kutta methods (RK) [22],
- Runge-Kutta methods based on Gauss-Legendre quadrature (GLRK) [77],
- Runge-Kutta-Nystrom methods (RKN) [24, 78],
- the symplectic Yoshida method (SY) [14].

Different versions of each scheme were implemented to obtain methods of different order. Moreover, for all the implemented methods, there is the possibility to use step regularisation (explained in section 2.3.1) and the projection method (explained in section 2.3.1).

All the coefficients used to define and implements the methods are reported in Appendix A.

Table 2.1: *Implemented integration methods and their properties.*

Method	(Order, Stages)	Type	Time step	Property	Other
RK4	(4,4)	Explicit	Fixed step		+ projection method
RK45	(5/4,7)	Explicit	Variable step		+ projection method + regularised step
RK8	(8,13)	Explicit	Fixed step		+ projection method + regularised step
RK78	(8/7,13)	Explicit	Variable step		+ projection method + regularised step
GLRK4 GLRK6 GLRK8	(4,2) (6,3) (8,4)	Implicit	Fixed step	Symplectic	+ projection method + regularised step
RKN8	(8,26)	Explicit	Fixed step	Symplectic	+ projection method + regularised step
RKN64	(6/4,6)	Explicit	Variable step	Symplectic	+ projection method + regularised step
SY4 SY6 SY8	(4,4) (6,8) (8,16)	Explicit	Fixed step	Symplectic Canonical	+ projection method + regularised step

Generic explicit Runge-Kutta methods

A single step of integration from t_n to $t_{n+1} = t_n + h$ following an explicit RK scheme is expressed as [22]:

$$x_{n+1} = x_n + hF(t_n, x_n, h; f), n \geq 0 \tag{2.9}$$

$$F(t_n, x_n, h; f) = \sum_{i=1}^{s} b_i K_i \tag{2.10}$$

$$K_i = f(t_n + c_i h, x_n + h \sum_{j=1}^{s} a_{ij} K_j), \quad i = 1, 2, \ldots, s \tag{2.11}$$

where x_n is the solution at the current step, t_n the value of the independent variable at the current step, h the step size, f the function to integrate, F is the increment function, s is the number of stages of the method, and a_{ij}, b_i, c_i are the coefficients that define a specific Runge-Kutta method. They are usually indicated as the Runge-Kutta matrix (a_{ij}), the vector of weights (b_i), and the vector of nodes (c_i); they are collected in the *Butcher tableau* $(\mathbf{a}, \mathbf{b}, \mathbf{c})$

$$\begin{array}{c|ccc} c_1 & a_{11} & \dots & a_{1s} \\ \vdots & \vdots & & \vdots \\ c_s & a_{s1} & \dots & a_{ss} \\ \hline & b_1 & \dots & b_s \end{array}$$

that completely define a Runge-Kutta method. The method is valid if the following relation is true [22]:

$$\sum_{j=1}^{i-1} a_{ij} = c_i, \ i = 2, ..., s$$

If the $a_{i,j}$ coefficients are equal to zero for $j \geq i, \ i = 1, ..., s$, each K_i can be computed explicitly as a function only of the $i-1$ coefficients K_1, K_{i-1} and the method is said to be *explicit*. If this is not the case, it is said to be *implicit* and requires the resolution of a non-linear system with s unknowns. More requirements are found if one requires the method to have a certain order p, meaning that the local truncation error is $O(h^{p+1})$, which can be derived from the definition of the truncation error itself. Moreover, explicit methods with s stages cannot have order higher than s itself [22].

Embedded methods can be used for step adaptation (thus increasing the efficiency of the scheme). The truncation error at each time step can be estimated by using two integrators at the same time, which is possible and convenient as they share most of the function evaluations [25, 85].

One-step RK schemes with s stages can become symplectic when applied to a dynamics in a Hamiltonian formulation if the coefficients of the Butcher's tableau $(\mathbf{a}, \mathbf{b}, \mathbf{c})$ satisfy the symmetric relation given in [86]:

$$b_i a_{ij} + b_j a_{ji} - b_i b_j = 0, \quad \forall i, j = 1, ..., s \tag{2.12}$$

In this way, the value of the Hamiltonian function will remain bounded during the integration, instead of presenting fictitious energy dissipation. However, this relation implies that explicit schemes cannot be symplectic without having all $\mathbf{b}$ coefficients equal to zero [86], thus making all symplectic RK methods implicit.

Gauss-Legendre Runge-Kutta

A class of symplectic implicit RK methods is represented by collocation methods. In particular, those derived from Gauss-Legendre quadrature coefficients (indicated as GLRK in Table 2.1) were selected for this work.

These schemes follow the general RK construction, and are particularly efficient for orbital propagation, since they are A-stable at all orders, thus allowing larger time

steps with lower error [77] (a numerical method is said to be A-stable if the solution $y(t) = e^{kt}$ to the test equation $y' = ky$ subject to the initial condition $y(0) = 1$ with $k \in \mathcal{C}$ approaches zero as $t \to \infty$ when $\mathrm{Re}(k) < 0$. [87]). GLRK methods using s stages yield a solution of order $p = 2s$ [77].

However, implicit methods require the resolution at every step of a system of non-linear implicit equations, which can be done with the use of Newton's or fixed-point iterations [77], with the consequence that the accuracy of this iterative process will affect also the accuracy of the propagation. The second option was chosen in the implementation of the method for the present work

With reference to Eq. 2.11, the algorithm for fixed-point iterations is described as follows [77]:

$$K_i^{new} = f(t_n + c_i h, x_n + h \sum_{j=1}^{s} a_{ij} K_j), \quad i = 1, 2, \ldots, s \tag{2.13}$$

The iterations are stopped either when a maximum number of iterations is reached, or when the difference between the values of K_i of the current iteration and the previous one fall below a given tolerance δ: $\max|K_i^{new} - K_i|/x_n < \delta$.

Runge-Kutta-Nyström methods

RKN schemes are partitioned RK methods, which are formulated to be applied to problems presenting a separable Hamiltonian function in the form [78]

$$\mathcal{H}(\mathbf{r}, \mathbf{v}) = \mathcal{T}(\mathbf{v}) + \mathcal{V}(\mathbf{r}), \quad \mathcal{T}(\mathbf{v}) = \frac{1}{2}\mathbf{v}^T\mathbf{v} \tag{2.14}$$

where the potential contribution $\mathcal{V}$ is function of the coordinate variables $\mathbf{r}$ (Cartesian position vector) only and the kinetic contribution T is a quadratic function of the associated momenta $\mathbf{v}$ (Cartesian velocity vector) only, with the equations of motion taking the form

$$\begin{cases} \dot{\mathbf{r}} = \mathbf{v} \\ \dot{\mathbf{v}} = -\frac{\partial \mathcal{V}}{\partial \mathbf{r}} = f(\mathbf{r}) \end{cases} \tag{2.15}$$

This kind of methods use two different sets of coefficients to integrate the coordinates and the momenta separately. For the integration step of length h which brings $(\mathbf{r}_n(t_n), \mathbf{v}_n(t_n))$ onto $(\mathbf{r}_{n+1}(t_{n+1}), \mathbf{v}_{n+1}(t_{n+1}))$ the algorithm follows:

$$\begin{cases} \mathbf{r}_{n+1} = \mathbf{r}_n + h\mathbf{v}_n + h^2 \sum_{i=1}^{s} b_i f(t_n + c_i h, \mathbf{K}_i) \\ \mathbf{v}_{n+1} = \mathbf{v}_n + h \sum_{i=1}^{s} d_i f(t_n + c_i h, \mathbf{K}_i) \\ \mathbf{K}_i = \mathbf{r}_n + c_i h \mathbf{v}_n + h^2 \sum_{j=1}^{s} a_{ij} f(t_n + c_j h, \mathbf{K}_j), \quad i = 1, ..., s \end{cases} \tag{2.16}$$

with a Butcher's tableau $(\mathbf{a}, \mathbf{b}, \mathbf{c}, \mathbf{d})$, where $\mathbf{b}$ are the coefficients used for the coordinates, and $\mathbf{d}$ the coefficients for the momenta:

$$\begin{array}{c|ccc} c_1 & a_{11} & \ldots & a_{1s} \\ \vdots & \vdots & & \vdots \\ c_s & a_{s1} & \ldots & a_{ss} \\ \hline & b_1 & \ldots & b_s \\ & d_1 & \ldots & d_s \end{array}$$

In the case of RKN methods, also explicit schemes can be symplectic, and embedded adaptive schemes are possible [24]. To be symplectic, an s-stage explicit scheme with Butcher's tableau $(\mathbf{A}, \mathbf{b}, \mathbf{c}, \mathbf{d})$ must satisfy the relations [78]:

$$\begin{cases} b_i = d_i(1 - c_i), \quad i = 1, ..., s \\ d_i(b_j - a_{ij}) = d_j(b_i - a_{ij}), \quad i, j = 1, ..., s \end{cases} \tag{2.17}$$

Canonical methods

Some numerical integration methods can be obtained directly from the Hamiltonian formulation of the problem, through subsequent canonical transformations. The methods so derived are symplectic, meaning that the truncation error in the total energy has no secular component, thus conserving the total energy exactly up to a certain order of accuracy [88].

In this work, the method proposed by Yoshida [14] in the separable Hamiltonian form was considered (SY in Table 2.1). Given the initial state $\mathbf{x}_0 = (\mathbf{r}_0, \mathbf{v}_0)^T$ at time t_0, the nth order solution at time $t_0 + h$ is given as a composition of elementary symplectic mappings of lower order, which is equal to the product of the operators:

$$\mathbf{x}(h) = \left[\sum_{i=1}^{k} \exp(c_i h D_T) \exp(d_i h D_V) \right] \mathbf{x}_0 \tag{2.18}$$

where D_T and D_V are differential operators associated with the kinetic and potential terms of the separable Hamiltonian defined in Eq. 2.14, and $\exp(\cdot)$ represents the exponential function. The map above gives a succession of k explicit mappings:

$$\begin{cases} \mathbf{r}_{i+1} = \mathbf{r}_i + c_i h \frac{\partial \mathcal{T}}{\partial \mathbf{v}}(\mathbf{v}_i) \\ \mathbf{v}_{i+1} = \mathbf{v}_i - d_i h \frac{\partial \mathcal{V}}{\partial \mathbf{r}}(\mathbf{r}_{i+1}) \\ i = 1, ..., k \end{cases} \tag{2.19}$$

with $\mathbf{x}_k = (\mathbf{r}_k, \mathbf{v}_k)$ being the solution at time step $t_0 + h$.

2.3.1 Additional numerical techniques

Time step regularisation

Following the procedure that was already implemented in SNAPPshot [5], the regularisation of the time step is obtained using the approach by [79] from the Jacobian $\mathbf{J}$ of the equations of motion.

Given the equations of motion $\dot{\mathbf{x}} = \mathbf{f}(\mathbf{x}, t)$, let $\mathbf{x} = (\mathbf{r}, \mathbf{v})^T$ be the state vector, containing position and velocity, and $f(\mathbf{x}, t)$ be equal to $(\mathbf{v}, \dot{\mathbf{v}})^T$. Then the Jacobian matrix is given by

$$\mathbf{J} = \frac{\mathrm{df}}{\mathrm{dx}} = \begin{bmatrix} \mathbf{0} & \mathbf{I} \\ \mathbf{G} & \mathbf{0} \end{bmatrix} \tag{2.20}$$

where $\mathbf{x} = (\mathbf{r}, \mathbf{v})^T$ is the state vector, containing position and velocity vectors, $\mathbf{I}$ is the identity matrix and $\mathbf{G}$ results from the derivation of the gravitational terms defined in Eq. 2.1.

Indicating with λ the eigenvalues of the matrix in 2.20 and with Λ the maximum eigenvalue, the condition for the stability of the integration scheme is written as

$$C\Lambda h < 1,$$

where h is the step size and the value of C is actually set by choosing an initial step-size that results in a sufficient number of integration steps per orbit. In this way, the user can set an accuracy level and the initial step h_0 is automatically computed by the integrator.

The integration step is rescaled as

$$h_{n+1} = h_n \frac{\Lambda(t_n)}{\Lambda(t_{n+1})}. \tag{2.21}$$

Debatin et al. [79] propose a simplified expression for Λ:

$$\Lambda = \left[\sum_{j=0}^{N} \frac{2\mu_j}{|x - x_j(t)|^3} \right]^{\frac{1}{2}} \tag{2.22}$$

where μ_j is the gravitational constant of the j^{th} considered body.

Projection methods

Projection methods are numerical techniques that correct the solution obtained with other integrators to minimise the integration error on a given first integral of the dynamics (e.g. the total energy of the system). In this way, a solution closer to the physical behaviour of the system is obtained [12].

Given an arbitrary one-step method Φ_h applied to the dynamical system $\dot{\mathbf{x}} = \mathbf{f}(\mathbf{x})$ such that $\mathbf{x}_{n+1} = \Phi_h(\mathbf{x}_n)$, where $\mathbf{x}$ represents the state vector, and given a quantity $I(\mathbf{x})$ that conserves during the propagation, generally the numerical solution given by the method does not satisfy the relation $I(\mathbf{x}_{n+1}) = I(\mathbf{x}_n)$ due to numerical errors. A new solution $\tilde{\mathbf{x}}_{n+1}$ such that $I(\tilde{\mathbf{x}}_{n+1}) = I(\mathbf{x}_0)$ can be obtained by solving a constrained minimisation problem considering the Lagrange function

$$\mathcal{L}(\tilde{\mathbf{x}}_{n+1}, \lambda) = \frac{1}{2}\|\tilde{\mathbf{x}}_{n+1} - \mathbf{x}_{n+1}\| - g(\tilde{\mathbf{x}}_{n+1})^T\lambda \tag{2.23}$$

with $g(\mathbf{x}) = I(\mathbf{x}) - I(\mathbf{x}_0)$ being the constraint vector function, and λ a vector of Lagrange multipliers. This leads to a simplified expression

$$\begin{cases} \tilde{\mathbf{x}}_{n+1} = \mathbf{x}_{n+1} + g'(\mathbf{x}_{n+1})^T\lambda \\ g(\tilde{\mathbf{x}}_{n+1}) = 0 \end{cases} \tag{2.24}$$

where $g'(\mathbf{x})$ represents the gradient of the function g with respect to the vector $\mathbf{x}$.

The second relation is a non-linear system of algebraic equations with λ unknown, that can be easily solved via Newton iterations:

$$\begin{cases} \Delta\lambda_i = -\left(g'(\mathbf{x}_{n+1})g'(\mathbf{x}_{n+1})^T\right)^{-1} g\left(\mathbf{x}_{n+1} + g'(\mathbf{x}_{n+1})^T\lambda_i\right) \\ \lambda_{i+1} = \lambda_i + \Delta\lambda_i \end{cases} \tag{2.25}$$

2.4 Application

Basing on previous works [89], the numeric chapter focuses on the analysis of the 8^{th} order methods, as they had showed the most interesting results after extensive analyses of their numerical properties.

2.4.1 Selection of test cases

The methods and models presented in this chapter are evaluated by comparing them in different applications, on the level of single propagations and on a statistical level when thousands of initial conditions are propagated in MC analyses, as in planetary protection studies. Various test cases were chosen in order to show if the differences observed in the propagation of single trajectories due to the choice of integration method and ephemeris model are important or not on a statistical level, and to quantify their effect on the overall analysis.

Two main groups of objects were considered, asteroids (whose reference data was taken from the Jet Propulsion Laboratory (JPL) Horizons ephemeris system[1] via the SPICE toolkit[2]), and mission cases that had already been studied for the presentation of SNAPPshot [5, 56, 57]:

- Asteroids
  - 99942 Apophis
  - 2010 RF_{12}
  - 2007 UD_6
- Interplanetary missions
  - Launcher upper stage of Solo
  - Launcher upper stage of Bepi Colombo

The asteroid cases were studied in terms of single propagations using the adaptive RK78 (already available in SNAPPshot [5]), the implicit GLRK8, the Runge-Kutta-Nyström RKN8, and the canonical SY8 methods (newly implemented in SNAPPshot as part of this work as seen in Table 2.1). In these cases, two ephemerides models were also compared, as introduced in the following section. Asteroid Apophis was selected since it is a well-known case used to study numerical propagation and impact probability, while asteroid 2010 RF_{12} was chosen as test case due to the multiple fly-bys with Earth, one when it was observed in 2010 and one that is expected in 2095 (which also presents one of the highest levels of impact probabilities in the Near-Earth Object (NEO) Risk List[3] from the European Space Agency (ESA)).

The MC analysis were performed for the asteroids Apophis and 2010 RF_{12}, and for the mission cases as well, by comparing the performance of RK78 and GLRK8, which were chosen due to the considerations made following the analysis of the single propagations. In the case of the asteroids, a number of runs for the MC analyses was

[1] `https://ssd.jpl.nasa.gov/horizons.cgi`
[2] `https://naif.jpl.nasa.gov/naif/`
[3] `http://neo.ssa.esa.int/risk-page`

chosen according to previous studies. On the contrary, for the planetary protection analysis, the number of runs was pre-estimated thanks to the SNAPPshot tools [5, 48], by applying the expression of the confidence interval by Wilson [51].

In all test cases, the initial conditions were defined with respect to the EME2000 inertial reference frame (Earth's Mean Equator and Equinox at 12:00 Terrestrial Time on 1 January 2000): the x-axis is aligned with the mean equinox, the z-axis is aligned with the Earth's celestial North Pole, and the y-axis is rotated by 90° East about the celestial equator [82].

2.4.2 Ephemeris models

The comparisons presented here also include planetary ephemerides coming from diverse sources, to show how the differences in the physical models affect the results of the propagations. In each model, the state of the planets and celestial bodies are obtained by integrating a set of n-body equations simulating the dynamics of the whole Solar System: these equations include gravitational and additional forces that are different for each model, with the possibility of affecting the propagation of a single trajectory.

The following models with the following characteristics were considered:

- the NASA JPL Horizons ephemeris system via the SPICE toolkit, which obtains the ephemeris data by integrating the n-body dynamics considering the gravitational and relativity effects of major planets, the Sun, the Moon, Vesta, and Ceres, and by using Chebyshev interpolation to obtain the states of all the included celestial bodies as function of time (for more details see `https://ssd.jpl.nasa.gov/?horizons_doc#longterm` and `https://ssd.jpl.nasa.gov/?horizons_doc#limitations`);

- the ESA routines interfacing with the JPL *de422* ephemerides;

- a third model, named "recomputed" here, which obtains the ephemeris data by integrating the complete n-body dynamics presented in Section 2.2 considering the gravitational and relativity effects of the major planets, the Sun, and the Moon, and by using cubic spline interpolation to obtain the states of all the included celestial bodies as function of time;

The third model is the one used for the propagations produced in this work, using the set of equations of the restricted n-body problem already presented in Section 2.2. Together with the gravitational terms, the accelerations related to the relativistic effects of the motion of the celestial bodies were also considered, obtaining the full equations

of motion in the Solar System in the form described by Armellin et al. in [75]:

$$\begin{aligned}\ddot{\mathbf{r}} = &\sum_i \frac{\mu_i(\mathbf{r}_i - \mathbf{r})}{r_i^3}\left\{1 - \frac{2(\beta+\gamma)}{c^2}\sum_j \frac{\mu_j}{r_j} - \frac{2\beta-1}{c^2}\sum_{j\neq i}\frac{\mu_j}{r_{ij}} + \frac{\gamma|\dot{\mathbf{r}}|^2}{c^2}\right.\\ &\left. + \frac{(1+\gamma)|\dot{\mathbf{r}}_i|^2}{c^2} - \frac{2(1+\gamma)}{c^2}\dot{\mathbf{r}}\cdot\dot{\mathbf{r}}_i - \frac{3}{2c^2}\left[\frac{(\mathbf{r}-\mathbf{r}_i)\cdot\dot{\mathbf{r}}_i}{r_i}\right]^2 + \frac{1}{2c^2}(\mathbf{r}-\mathbf{r}_i)\cdot\ddot{\mathbf{r}}_i\right\}\\ &+ \sum_i \frac{\mu_i}{c^2 r_i}\left\{\frac{3+4\gamma}{2}\ddot{\mathbf{r}}_i + \frac{\{[\mathbf{r}-\mathbf{r}_i]\cdot[(2+2\gamma)\dot{\mathbf{r}} - (1+2\gamma)\dot{\mathbf{r}}_i]\}(\mathbf{r}-\mathbf{r}_i)}{r_i^2}\right\}\end{aligned} \tag{2.26}$$

where $\mathbf{r}$ is the point of interest, μ_i and $\mathbf{r}_i$ are the gravitational parameter and the Solar System barycentric position of body or planetary system i, $\mathbf{r}_i = |\mathbf{r}_i - \mathbf{r}|$, c is the speed of light in vacuum, and β and γ are the parametrized post-Newtonian parameters measuring the non-linearity in superposition of gravity and space curvature produced by unit rest mass [90]. In Eq. 2.26 it is assumed that the object being propagated is affected by the gravitational attraction of n bodies, but has no gravitational effect on them; i.e., the restricted (n+1)-body problem approximation is adopted.

The relativistic effects can be switched on or off according to the parameters of the simulation, and it was not used when comparing symplectic and non-symplectic integration methods. This choice was made since the adopted model described in Armellin et al. is not consistent with the Horizons model. This issue was addressed by Masat et al. [91] with a representation of the relativity model requiring the resolution of a linear system (thus increasing the computational complexity of the propagator) to include correctly the gravitational acceleration terms $\ddot{\mathbf{r}}_i,\ i = 1, ..., n$ of all celestial bodies.

This model was used in two ways: to produce reference data for the asteroids used in the test cases (Section 2.4.4), and also to produce the planetary ephemerides. When using this model, the states of the planets obtained by the integration of the complete n-body model of the solar system are interpolated and then imposed as the time-dependant terms in the equations of the restricted problem. This choice was done to make the physical model coherent, by using planetary ephemerides that are consistent with the dynamics described by the equations that are integrated.

For the work presented in this chapter, the n-body equations were integrated using the variable step RK78 integrator with relative and absolute tolerances equal to 10^{-12}.

2.4.3 Single propagations

A series of tests were carried out to show how the considered symplectic and non-symplectic 8$^{\text{th}}$ order methods (RK78, GLRK8, RKN8, and SY8) perform for the integration of the n-body equations of motion expressed in Eq. 2.1. The case in exam is the propagation of asteroid Apophis between 1989 and 2039, with the ephemerides for every planet obtained from the JPL SPICE model.

The integrations of the equations of motion are carried out using Cartesian coordinates in an inertial reference frame centred in the solar system barycentre. Non-dimensional variables are used, following the approach of Colombo et al. [5], obtained by dividing, respectively, distance and time by

$$\bar{L} = AU, \qquad \bar{t} = 2\pi\sqrt{AU^3/\mu_{Sun}}$$

where AU is the Astronomical Unit and μ_{Sun} is the gravitational constant of the Sun. The trajectory is propagated under the effect of gravitational forces of the Sun and all the planetary systems considered with their barycentre, except for the Earth and the Moon, considered as separate bodies. No additional perturbations such as solar radiation pressure and relativistic effects were included. All propagators with adaptive time step use relative and absolute tolerances both equal to 10^{-12}. Following the option already available in SNAPPshot [5], the initial step size was determined for all the fixed-step and regularised step methods via a single-step run of RK78 using relative and absolute tolerances both equal to 10^{-12}: in this way, an accuracy level was set and the initial step size was automatically computed by the integrators.

The value of the Hamiltonian function shown in Fig. 2.1 to Fig. 2.3 is the one introduced in Eq. 2.3 the expected value is thus analytically zero during the whole propagation, with variations only due to numerical errors; on the right, the error over the state (position $\Delta\mathbf{r}$ and velocity $\Delta\mathbf{v}$)is shown. The errors are defined as follows:

- $\Delta\mathbf{r} = |\mathbf{r}(t) - \mathbf{r}_{ref}|$ is the deviation of the integrated position from the JPL SPICE ephemerides used as reference, and measures the position error;
- $\Delta\mathbf{v} = |\mathbf{v}(t) - \mathbf{v}_{ref}|$ is the deviation of the integrated velocity from the JPL SPICE ephemerides used as reference, and measures the velocity error.

Fig. 2.1 shows the value of the Hamiltonian (a) for the propagation of Apophis from 1989 to 2029 (before the predicted fly-by with the Earth in 2029) using a fixed step size. We can observe that, when the dynamics is regular, the symplectic methods (GLRK, RKN and SY, respectively the red, yellow and purple lines) preserve the value of the Hamiltonian as expected, with bounded oscillations but no secular drift, while the non-symplectic RK method (blue line) shows a small linear variation; the implicit RK method shows a comparable level of error over the state (position $\Delta\mathbf{r}$ in (b) and velocity $\Delta\mathbf{v}$ in (c)) of Apophis as given by the non-symplectic RK method.

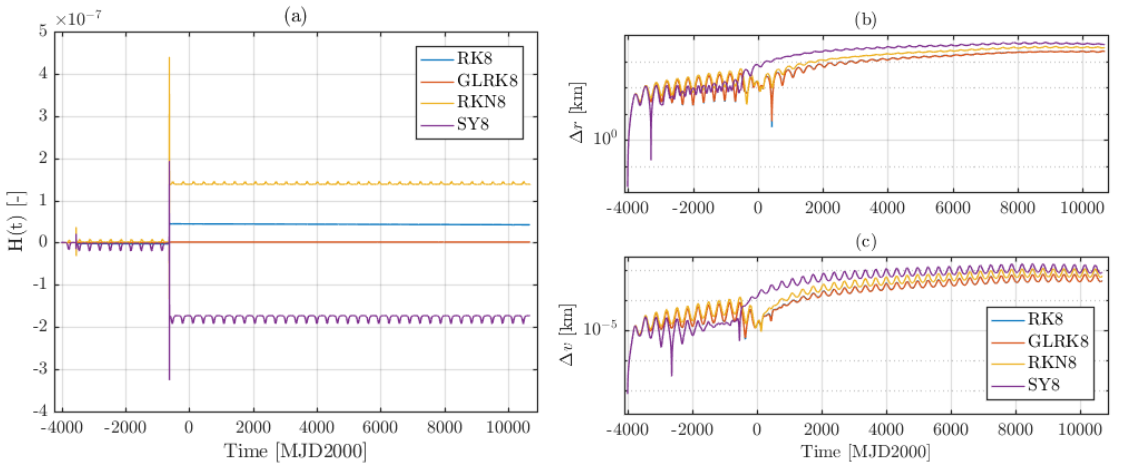

Figure 2.1: *Comparison among the different fixed-step integration methods for the propagation of asteroid Apophis from 1989 to 2029; (a) Value of the Hamiltonian function in time, (b) position and (c) velocity errors in time with respect to the reference ephemerides.*

The same time interval was considered in the propagation shown in Fig. 2.2, with the use in this case of step regularisation for all the integration schemes. Here also the non-symplectic adaptive method RK78 was used as a reference to compare the performance of the proposed methods with the tools already available in SNAPPshot. In this case, as expected, the value of the Hamiltonian in (a) shows a secular drift also for symplectic methods due to the variation of the time step. The method by Yoshida (SY), however, shows a better behaviour in terms of error over the state.

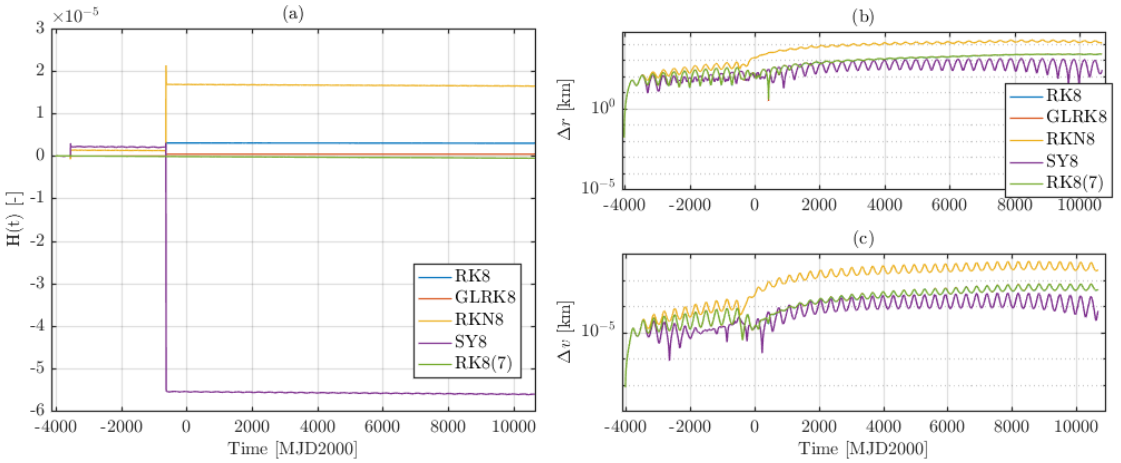

Figure 2.2: *Comparison among the different regularised-step integration methods for the propagation of asteroid Apophis from 1989 to 2029; (a) Value of the Hamiltonian function in time, (b) position and (c) velocity errors in time with respect to the reference ephemerides.*

The long-term behaviour seen in Fig. 2.1 and Fig. 2.2, however, changes when a flyby occurs during the propagation. Fig. 2.3 also shows the propagation of Apophis, in this case in the window 1989-2039 in order to include also the 2029 fly-by with Earth. The increase of non-linearity of the dynamics during the fly-by can be visualised in the jump of several orders of magnitude that the total energy in (a) and the state error in (b) and (c) undergo at the epoch of the flyby, affecting in similar ways all the integration schemes and hiding the approximation errors of the integrations. Similar jumps can also be observed in Fig. 2.1 and Fig. 2.2, again due to close approaches with Earth. In these cases, however, the variation in the total energy is much more contained than in the case of a deep fly-by, due to the larger distance from the planet.

Fig. 2.4 shows the performance of the integration methods both in terms of accuracy and in terms of efficiency: the maximum errors (energy in (a) and (d), position in (b) and (e), and velocity in (c) and (f)) are related to the average computational time[4] to perform one integration step. The errors are defined as follows:

- $\Delta\mathcal{H}_{max} = \max|\mathcal{H}(t) - \mathcal{H}_0| = \max|\mathcal{H}(t)|$ is the maximum deviation of the value of the Hamiltonian function obtained via integration from the value at the initial time, and measures the energy error;

- $\Delta\mathbf{r}_{max} = \max|\mathbf{r}(t) - \mathbf{r}_{ref}|$ is the maximum deviation of the integrated position from the JPL SPICE ephemerides used as reference, and measures the position

[4]The simulations were run on a machine with a processor Intel(R) Xeon(R) CPU E5-4620 v4 @ 2.10 GHz.

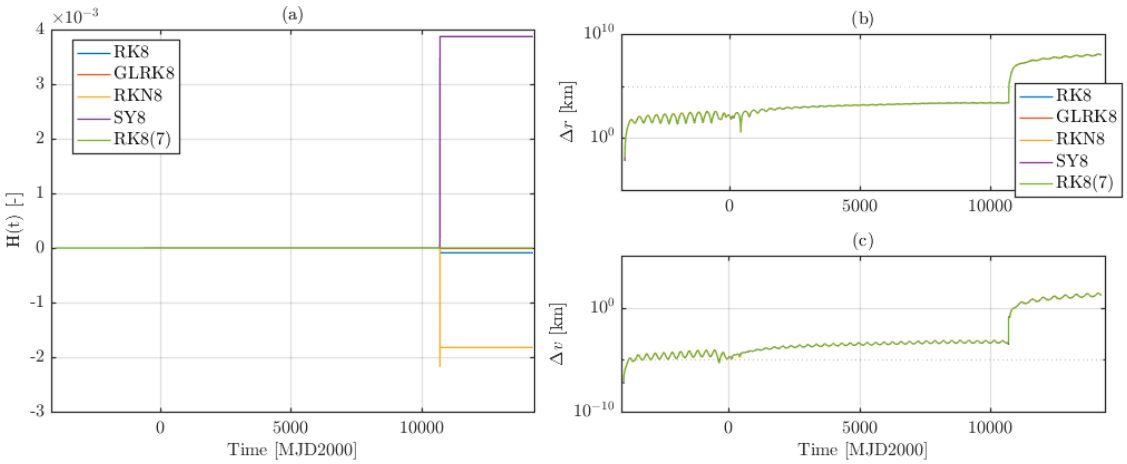

Figure 2.3: *Comparison among the different regularised-step integration methods for the propagation of asteroid Apophis from 1989 to 2039; (a) Value of the Hamiltonian function in time, (b) position and (c) velocity errors in time with respect to the reference ephemerides.*

error;

- $\Delta\mathbf{v}_{max} = \max|\mathbf{v}(t) - \mathbf{v}_{ref}|$ is the maximum deviation of the integrated velocity from the JPL SPICE ephemerides used as reference, and measures the velocity error.

From the results presented here it can be observed that the symplectic implicit Runge-Kutta (GLRK) and the method by Yoshida (SY) are the most accurate in terms of position error in time among the ones taken into exam, respectively with a fixed-step and a regularised step. However, while the SY method performs generally better when the distance from the celestial bodies is large enough, the GLRK in both cases shows a better conservation of energy in time also when close approaches are present. The higher computational time with respect to the other integration methods is due to the fixed-point iterations to solve the implicit problem at every step. For this reason, a focus on methods to solve implicit systems of non-linear equations could improve the efficiency of the integrator.

After studying the energy conservation performance of the various methods, this analysis focuses now on the propagations of selected asteroid trajectories to evaluate errors over position and velocity following close approaches with planets. The results are compared when the different ephemeris models presented in 2.4.2 are used. All the integration methods analysed before were chosen to be applied to these test cases but RKN8, since it has been observed as the least accurate in most cases as inferred from Fig. 2.4. Tables 2.2, 2.3, and 2.4 report the timespan and the parameters used to set the propagations of Apophis, 2010 RF_{12}, and 2007 UD_6, respectively, while the various figures visualise the results according to different parameters, to show the evolution of the orbit computed according to the various methods, and to compare their accuracy on a numerical level.

The results of the 50 years long propagation of asteroid Apophis are shown in Figures 2.5 and 2.6: in the first, they are represented in terms of the distance of Apophis

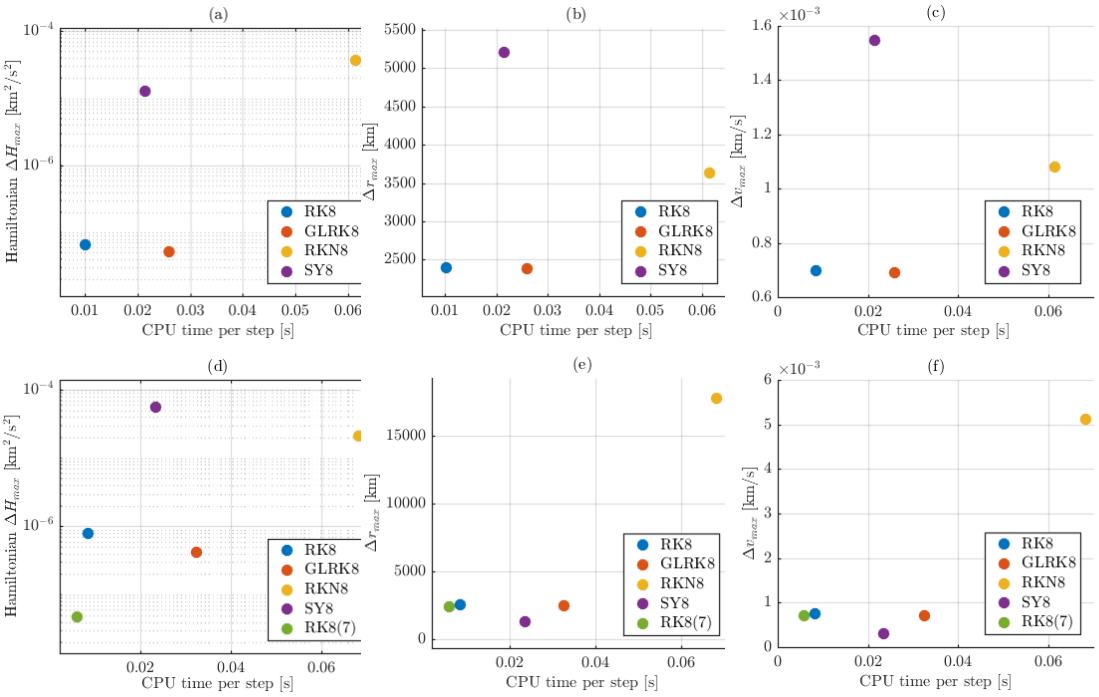

Figure 2.4: *Plots showing the efficiency and the accuracy of the methods in terms of average computational time per step (x axis) and maximum error (y axis): (a) maximum energy error, (b) maximum position error, (c) maximum velocity error for fixed-step propagations; (d) maximum energy error, (e) maximum position error, (f) maximum velocity error for propagations with step regularisation.*

Table 2.2: *Parameters for the propagation of the asteroid 99942 Apophis.*

Propagation start epoch	1989/01
Propagation end epoch	2039/01
Expected fly-bys with the Earth	2029/01
Integration tolerance (absolute)	10^{-12}
Integration tolerance (relative)	10^{-12}
Integrators	RK78, GLRK8, SY8

from Earth using the Horizons ephemerides in (a) and the recomputed ephemerides in (b); in the second, they are shown in terms of errors on the position (a) and velocity (b) during the propagation with respect to the Horizons ephemerides, and errors on the position (c) and velocity (d) during the propagation with respect to the recomputed model. It is clearly visible in all the plots that the greatest differences among the propagations arise after the fly-by of Apophis with Earth in 2029: while the propagations are all in agreement with each other up to that epoch, the very close approach with the Earth, as expected, increases the error differently for all the propagators, magnifying the small differences initially present before the event.

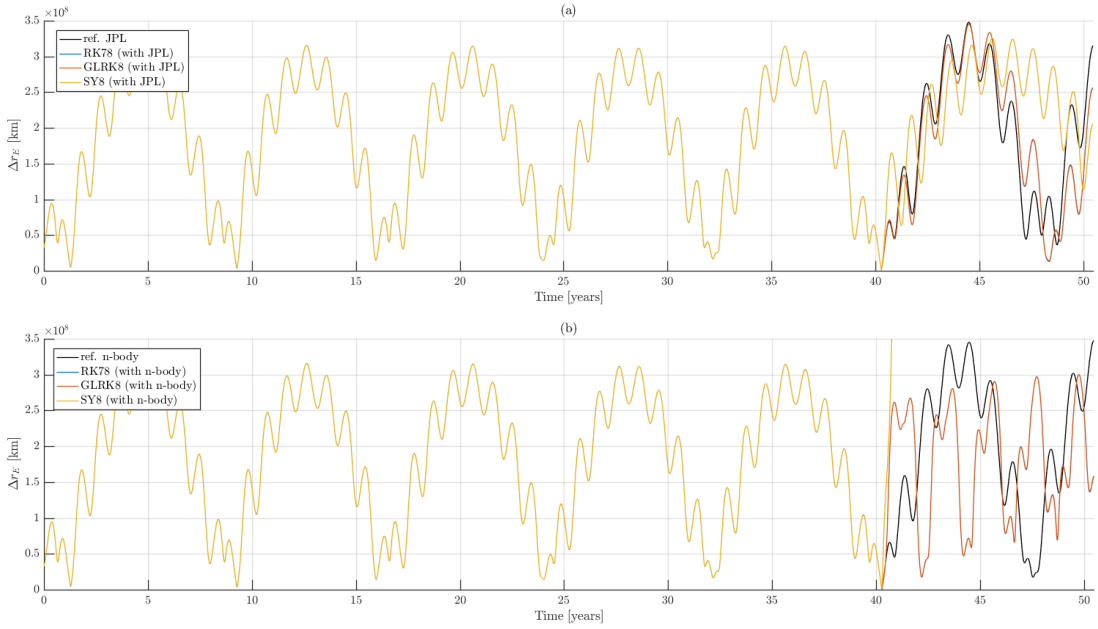

Figure 2.5: *Distance of Apophis from the Earth during the propagation according to different integration methods, using Horizons ephemerides (a), using the recomputed ephemerides (b).*

In Figures 2.7 and 2.8, instead, it is possible to observe the results of the propagations of asteroid 2010 RF_{12} for 100 years: similarly to what was observed in the previous case, the early fly-by of 2010 increases the error over the state, which propagates in time until it diverges from the expected trajectory in correspondence with the second fly-by in similar ways for all the included integration methods. An analogous solution is found with the propagation of asteroid 2007 UD_6 also for 100 years, which shows in Figures 2.9 and 2.10 an agreement among all the integration methods until the 2048 fly-by with Earth occurs. However, it is clearly visible that, while the Runge-Kutta schemes RK78 and GLRK8 (blue and red lines in all plots, respectively) are usually in good agreement with each other and the reference data (black lines), the canonical symplectic integrator SY8 (yellow lines) performs generally worse, probably due to the different way it is defined. For this reason, this numerical scheme was not considered for the statistical analyses in Sections 2.4.4 and 2.4.5.

It is worth noticing the differences that all test cases show in the propagations using

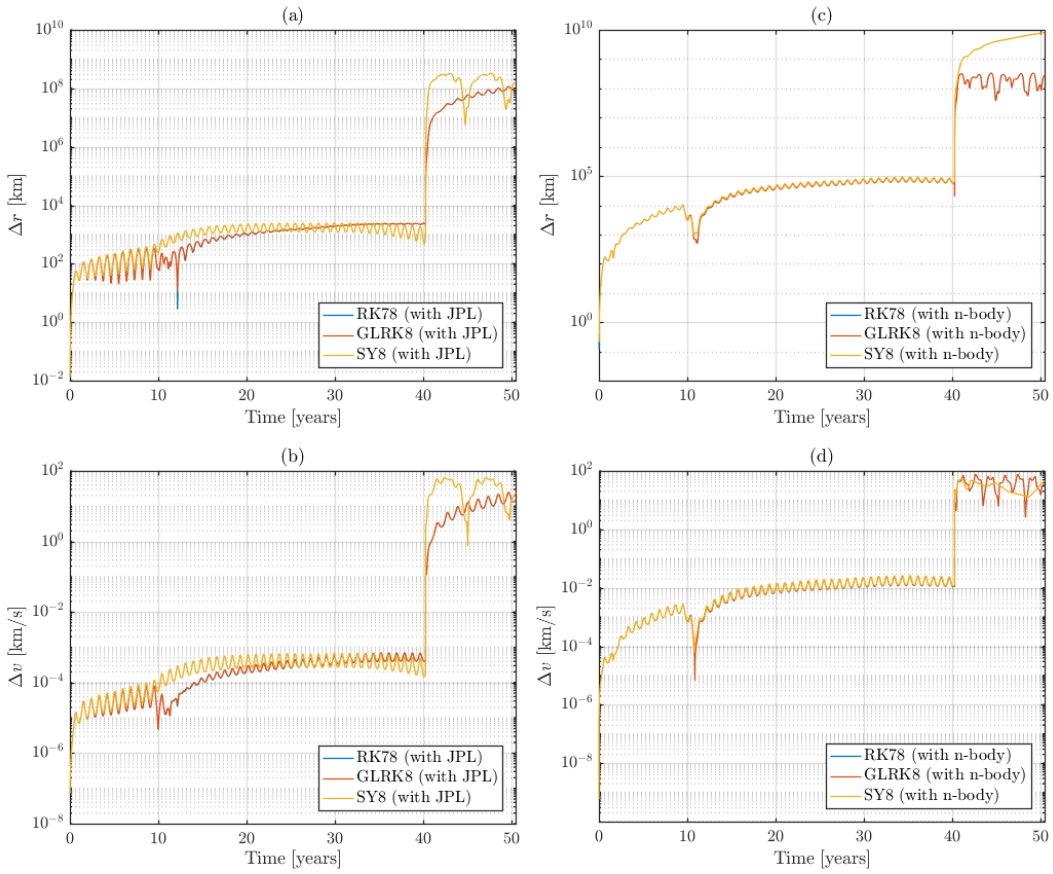

Figure 2.6: *Errors in Apophis position (a) and velocity (b) during the propagation with respect to the Horizons ephemerides, and errors in Apophis position (c) and velocity (d) during the propagation with respect to the recomputed model.*

Table 2.3: *Parameters for the propagation of the asteroid 2010 RF_{12}.*

Propagation start epoch	2001/01
Propagation end epoch	2100/01
Expected fly-bys with Earth	2010/09, 2095/09
Integration tolerance (absolute)	10^{-12}
Integration tolerance (relative)	10^{-12}
Integrators	RK78, GLRK8, SY8

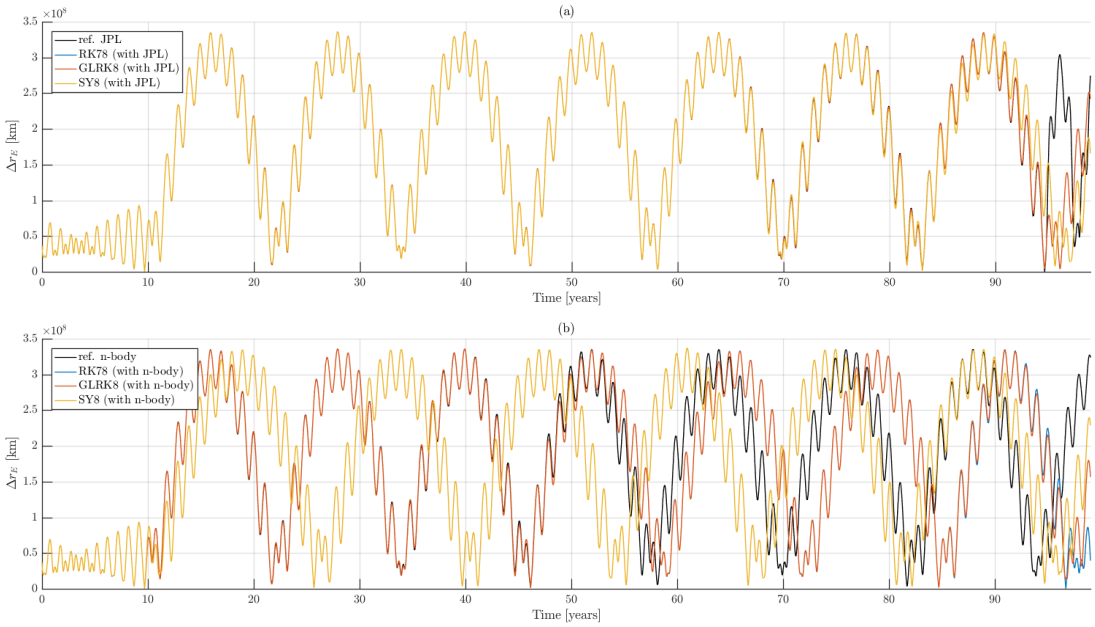

Figure 2.7: *Distance of asteroid 2010 RF_{12} from the Earth during the propagation using different integration methods, using Horizons ephemerides (a), using the recomputed ephemerides (b).*

Table 2.4: *Parameters for the propagation of the asteroid 2007 UD_6.*

Propagation start epoch	2001/01
Propagation end epoch	2100/01
Expected fly-bys with Earth	2007/10, 2048/01
Integration tolerance (absolute)	10^{-12}
Integration tolerance (relative)	10^{-12}
Integrators	RK78, GLRK8, SY8

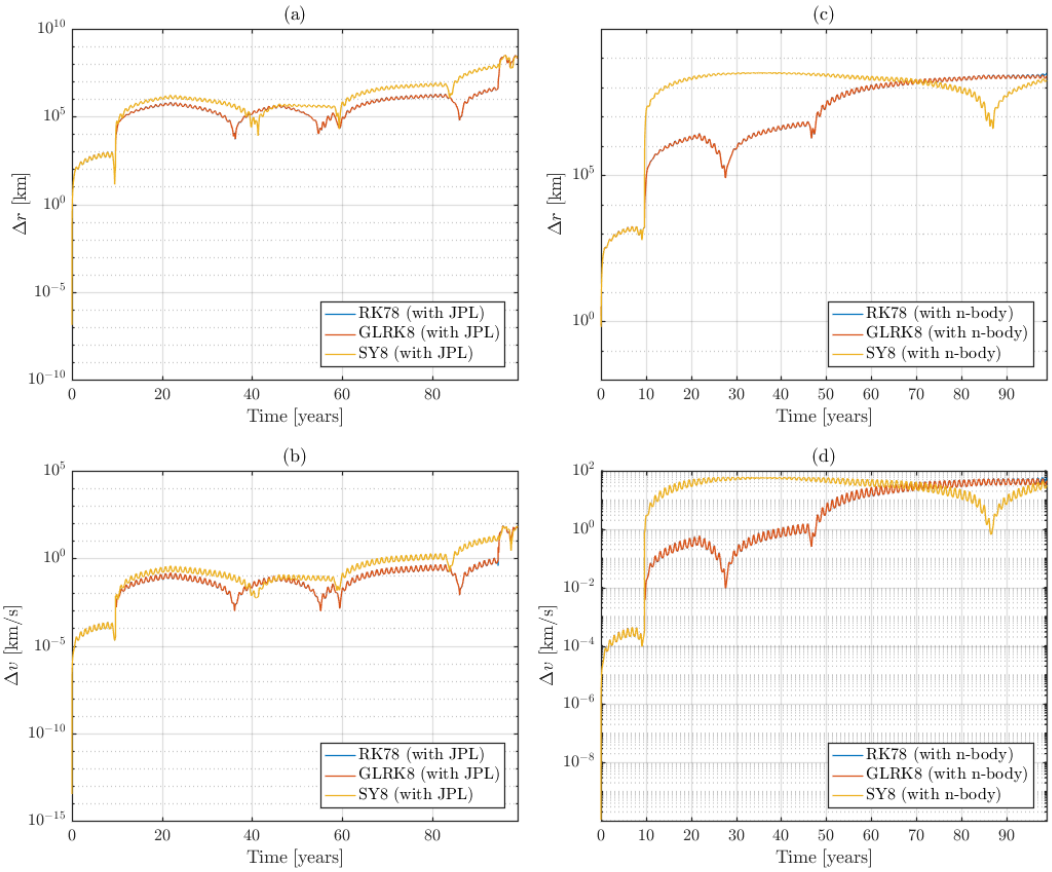

Figure 2.8: *Errors in asteroid 2010 RF_{12} position (a) and velocity (b) during the propagation with respect to the Horizons ephemerides, and errors in position (c) and velocity (d) during the propagation with respect to the recomputed model.*

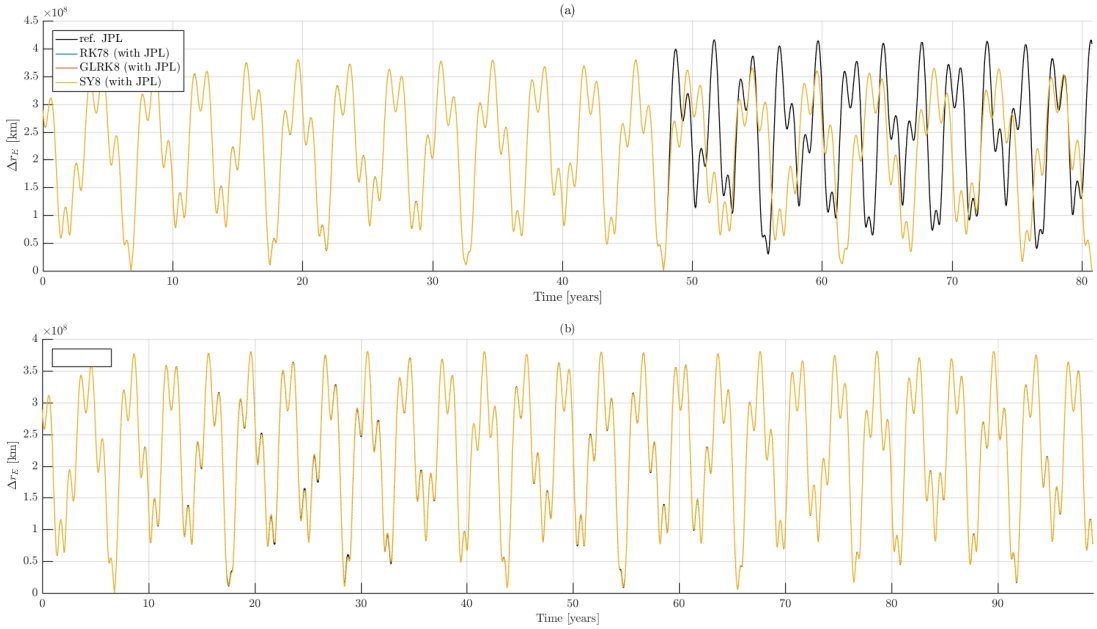

Figure 2.9: *Distance of asteroid 2007 UD_6 from the Earth during the propagation using different integration methods, using Horizons ephemerides (a), using the recomputed ephemerides (b).*

the recomputed n-body ephemerides with respect to the ones obtained via the Horizons system. These differences are visible as higher error values between the trajectories of the asteroids after the propagation in the restricted n-body problem using the recomputed planetary ephemerides, and the reference trajectories of the same asteroids obtained via the integration of the complete n-body problem, and are related to the different integration methods and tolerances that were used to obtain them and the interpolation methods.

2.4.4 Statistical analyses

This section is dedicated to analysing the performance of the selected integration methods on a statistical level, to show how the differences found in their applications to propagate single trajectories are reduced when considering thousands of them in MC simulations. In this section and in the next, the analysis focuses on two of the three integrators considered so far, that is RK78 and GLRK8, as previous tests showed they outperformed the SY8 method in terms of accuracy with both Horizons and recomputed ephemeris models.

The statistical analysis employs the same MC approach already available in SNAPPshot, by singularly propagating several initial conditions, using the parameters reported in Tables 2.7 and 2.8 for the propagations. The cases of the asteroids Apophis and 2010 RF_{12} were analysed to compare the performance of the RK78 and GLRK8 methods. In both cases initial conditions were expressed in equinoctial parameters [92], with initial uncertainties in the form of diagonal covariance matrices, and then transformed into Cartesian coordinates for the propagation. These data were obtained by accessing the

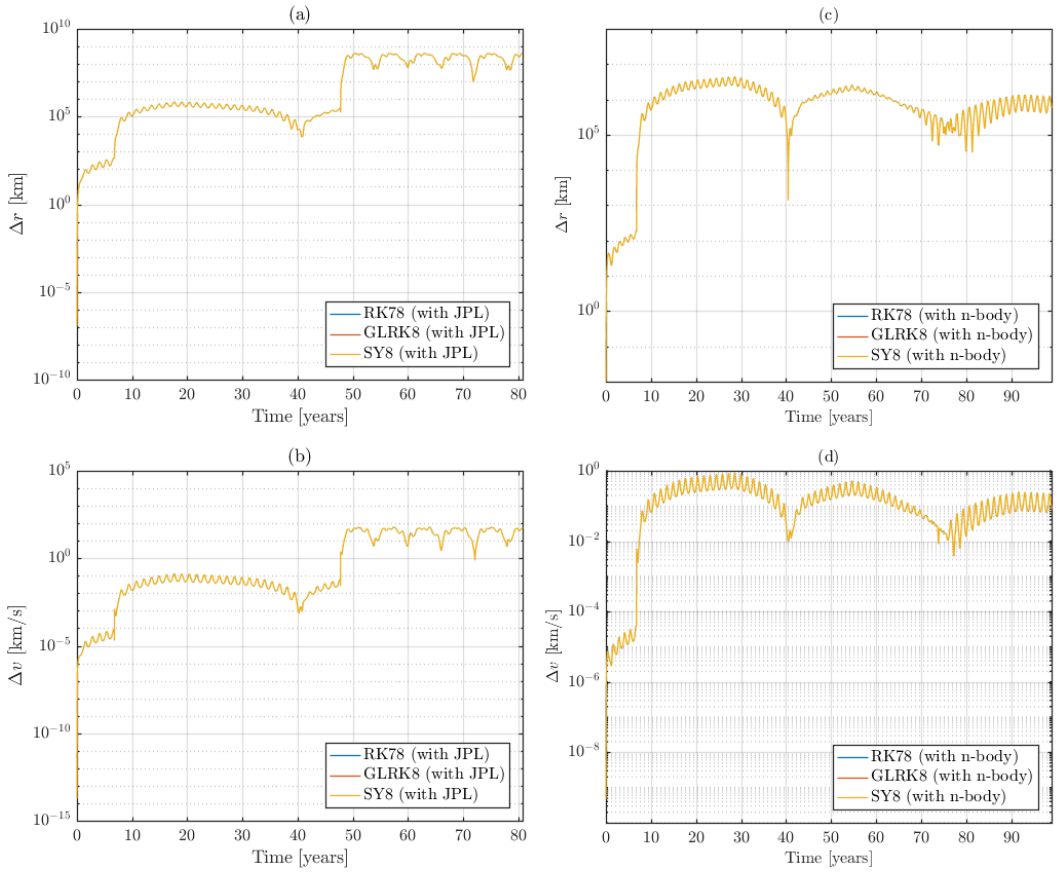

Figure 2.10: *Errors in asteroid 2007 UD_6 position (a) and velocity (b) during the propagation with respect to the Horizons ephemerides, and errors in position (c) and velocity (d) during the propagation with respect to the recomputed model.*

Near-Earth Object Dynamic Site (NEODyS[5]) in July 2018.

Table 2.5: *Parameters of the statistical analysis for the asteroid 99942 Apophis.*

Dispersion of initial conditions	Yes (covariance matrix)
Dispersion of Area-to-Mass ratio	No (fixed value 0.0 m^2/kg)
Number of MC runs	10^6
Propagation length	33.3 years
Integrators	RK78, GLRK8
Ephemerids	JPL Horizons (SPICE toolkit)

Table 2.6: *Parameters of the statistical analysis for the asteroid 2010 RF_{12}.*

Dispersion of initial conditions	Yes (covariance matrix)
Dispersion of Area-to-Mass ratio	No (fixed value 0.0 m^2/kg)
Number of MC runs	10^4
Propagation length	80.7 years
Integrators	RK78, GLRK8
Ephemerids	JPL Horizons (SPICE toolkit)

Figures 2.11 and 2.12 show the results of the MC analyses of Apophis and 2010 RF_{12} in terms of initial uncertainty dispersion over the semimajor axis a and the equinoctial longitude l. In each plot, the grey dots represent the random initial conditions not leading to an impact, while the coloured dots represent impacts: in the case of asteroid Apophis, the impacting solutions refer to three different events, in 2035, 2036, and 2037 (blue, purple, and red, respectively), while for asteroid 2010 RF_{12} only the impact event in 2095 is considered.

Both figures show that the two integration methods give results that do not differ relevantly between each other in both test cases, identifying the same impact regions within the initial uncertainty distributions. The numerical results are reported in Tables 2.7 and 2.8 in terms of number of impacts, impact probability and associated standard deviation, together with the total computational time[6] as measure of the efficiency of the numerical schemes. From both tables one can see that extremely similar values of the impact probability can be obtained with the two methods, despite showing diverse behaviours on the propagation of a single trajectory, which thus become not relevant on statistical levels. One can also see that the implicit GLRK8 method needs a longer computational time with respect to the explicit method, due to the iterations that have to be performed in order to solve the implicit system of equation that characterises the method. In the implementation used for this work, the implicit problem was solved using a fixed-point solver with a stopping condition based on the relative error between two iterations, and a tolerance equal to 10^{-15}, with the intention to focus mainly on the

[5] `https://newton.spacedys.com/neodys/`

[6] The simulations were run on a machine with a processor Intel(R) Xeon(R) CPU E5-4620 v4 @ 2.10 GHz.

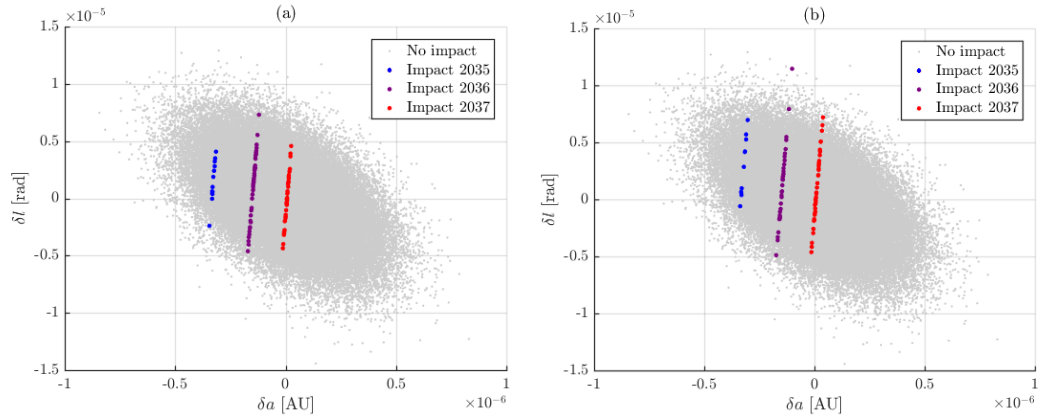

Figure 2.11: *Visualisation of the initial dispersion in the uncertainty space $(\delta a, \delta l)$ for the statistical analysis of asteroid Apophis with RK78 (a) and GLRK8 (b), with grey dots corresponding to the random initial conditions that do not lead to an impact and colored dots leading to impacts with Earth during the resonant close approaches in 2035 (blue), 2036 (purple), 2037 (red).*

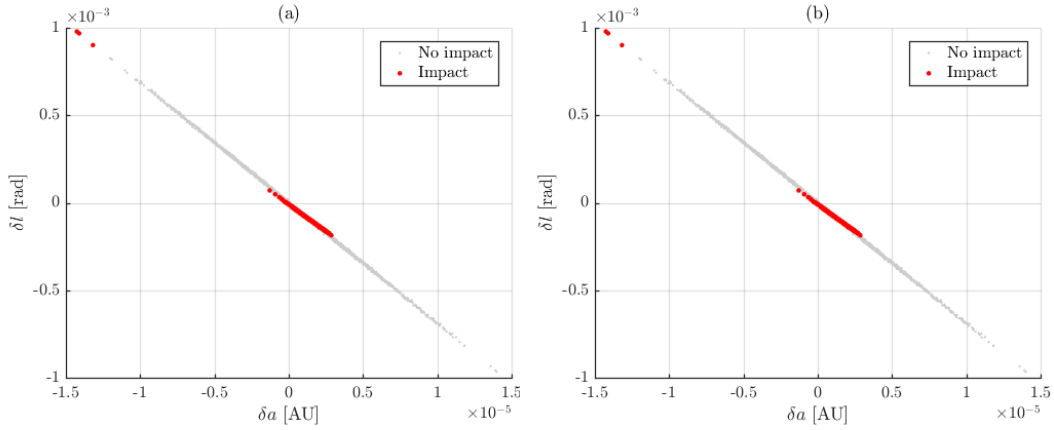

Figure 2.12: *Visualisation of the initial dispersion in the uncertainty space $(\delta a, \delta l)$ for the statistical analysis of asteroid 2010 RF_{12} with RK78 (a) and GLRK8 (b), with grey dots corresponding to the random initial conditions that do not lead to an impact and red dots leading to impacts with Earth during the close approaches in 2095.*

accuracy of the integration method than on the computational efficiency.

Table 2.7: *Results and performance of the statistical analysis of the asteroid Apophis.*

	RK78	GLRK8
Number of impacts	100 (Earth)	99 (Earth)
Impact probability $P(I)$	$1.00 \cdot 10^{-4}$	$9.90 \cdot 10^{-5}$
Standard deviation σ	$9.99 \cdot 10^{-6}$	$9.95 \cdot 10^{-6}$
Computational time	92.8 h	280.5 h

Table 2.8: *Results and performance of the statistical analysis of the asteroid 2010 RF*$_{12}$.

	RK78	GLRK8
Number of impacts	687 (Earth)	688 (Earth)
Impact probability $P(I)$	$6.87 \cdot 10^{-2}$	$6.88 \cdot 10^{-2}$
Standard deviation σ	$2.50 \cdot 10^{-3}$	$2.50 \cdot 10^{-3}$
Computational time	0.85 h	2.42 h

2.4.5 Planetary protection analyses

In this Section another statistical analysis is performed, this time with the goal of analysing planetary protection requirements for two interplanetary missions. The launcher upper stages of the Solar Orbiter and the Bepi Colombo missions were chosen as test cases to compare the results of the planetary protection analysis with the ones already presented for the characterisation of SNAPPshot [5, 56, 57]. The analyses were done in both cases using the functionalities of SNAPPshot: preliminary estimation of required MC runs according to an expected impact probability level and a required confidence level (as already introduced earlier in the chapter), and post-processing with the b-plane analysis to identify orbital resonances and other situations of interest [5, 56, 57]. The comparisons between the integration methods includes again RK78 (already available in SNAPPshot [5]) and GLRK8 (newly implemented in this work).

As a reference, the definition of the b-plane is presented. It is based on an analytical theory that attempts to set up a first model for orbital resonances, initially developed based on Opik's variables [93].

When a CA is detected (as a crossing of the SOI or using other criteria, such as the one that will be introduced in Section 2.5), the b-plane is defined as the plane perpendicular to the object incoming planetocentric velocity. A reference system $[\hat{\eta}, \hat{\xi}, \hat{\zeta}]$ is defined [93] such that: $\hat{\eta}$ is parallel to the planetocentric velocity of the object, $\hat{\zeta}$ is parallel to the projection of the body velocity on the b-plane, but with opposite direction; $\hat{\xi}$ completes a right-handed reference system.

The definition of these coordinates allows to obtain an insight on the characteristics

of the close approach, and to easily represent conditions of orbital resonance as circle represented on the b-plane [94, 95].

Tables 2.14 and 2.13 report the parameters that were used for the analyses of the Solar Orbiter and the Bepi Colombo launcher upper stages, respectively, similarly to what was done in the case of the asteroids. In both cases, the initial epoch, states and the covariance matrices representing the dispersion of initial conditions were also taken from [5, 56, 57], and are reported in Tables 3.1 and 2.12.

Table 2.9: *Parameters of the planetary protection analysis for the launcher upper stage of the Solar Orbiter mission.*

Dispersion of initial conditions	Yes (covariance matrix)
Dispersion of Area-to-Mass ratio	No (fixed value 0.0 m^2/kg)
Probability and confidence levels	10^{-4}, 0.99
Number of MC runs	54114
Propagation length	100 years
Integrators	RK78, GLRK8
Ephemerids	ESA routines with *de422*

Table 2.10: *Parameters of the planetary protection analysis for the launcher upper stage of the Bepi Colombo mission.*

Dispersion of initial conditions	Yes (covariance matrix)
Dispersion of Area-to-Mass ratio	No (fixed value 0.0 m^2/kg)
Probability and confidence levels	10^{-4}, 0.99
Number of MC runs	54114
Propagation length	100 years
Integrators	RK78, GLRK8
Ephemerids	ESA routines with *de422*

For these two cases, similar considerations to the ones already made for the asteroids Apophis and 2010 RF_{12} can be made, both in terms of numerical results and computational performances[7]. Figures 2.13 and 2.14 show the results of the MC analysis in terms of initial velocity dispersion in both cases, highlighting how the two selected integration methods can identify correctly and with no relevant differences between each other the regions of initial conditions leading to a simple close approach with either Venus or the Earth (dark grey dots), a resonant orbit with such planets (yellow dots), or an impact (red dots). Tables 2.14 and 2.13 report the number of impacts and impact probabilities for each case, which, again, are not significantly different between the two methods.

[7]The simulations were run on a machine with a processor Intel(R) Xeon(R) CPU E5-4620 v4 @ 2.10 GHz.

Table 2.11: *Initial conditions for the simulations of the state inaccuracy of the launcher upper stage of Solar Orbiter: epoch, position, velocity, and the associated covariance matrix are reported, defined in the inertial EME2000 reference frame centres in the Sun.*

Epoch, MJD2000	$\mathbf{r}$, km, $\mathbf{v}$, km/s (EME2000 centred in the Sun)				
6868.6194	132048839.01817, 63140185.879734, 27571915.378760				
	-12.199001757542, 20.240166264928, 9.767449779832				
Covariance matrix (EME2000)					
x, km	y, km	z, km	v_x, km/s	v_y, km/s	v_z, km/s
$5.351 \cdot 10^4$	$5.409 \cdot 10^4$	$-2.562 \cdot 10^4$	$2.482 \cdot 10^{-1}$	$2.744 \cdot 10^{-1}$	$-1.205 \cdot 10^{-1}$
$5.409 \cdot 10^4$	$1.355 \cdot 10^5$	$4.508 \cdot 10^3$	$2.337 \cdot 10^{-1}$	$7.100 \cdot 10^{-1}$	$3.427 \cdot 10^{-2}$
$-2.562 \cdot 10^4$	$4.508 \cdot 10^3$	$1.728 \cdot 10^5$	$-1.370 \cdot 10^{-1}$	$5.015 \cdot 10^{-2}$	$8.333 \cdot 10^{-1}$
$2.482 \cdot 10^{-1}$	$2.337 \cdot 10^{-1}$	$-1.370 \cdot 10^{-1}$	$1.156 \cdot 10^{-6}$	$1.179 \cdot 10^{-6}$	$-6.485 \cdot 10^{-7}$
$2.744 \cdot 10^{-1}$	$7.100 \cdot 10^{-1}$	$5.015 \cdot 10^{-2}$	$1.179 \cdot 10^{-6}$	$3.724 \cdot 10^{-6}$	$3.078 \cdot 10^{-7}$
$-1.205 \cdot 10^{-1}$	$3.427 \cdot 10^{-2}$	$8.333 \cdot 10^{-1}$	$-6.485 \cdot 10^{-7}$	$3.078 \cdot 10^{-7}$	$4.019 \cdot 10^{-6}$

Table 2.12: *Initial conditions for the simulations of the state inaccuracy of the launcher upper stage of Bepi Colombo: epoch, position, velocity, and the associated covariance matrix are reported, defined in the inertial EME2000 reference frame centres in the Sun.*

Epoch, MJD2000	$\mathbf{r}$, km, $\mathbf{v}$, km/s (EME2000 centred in the Sun)				
6693.7946	-119442379.96300, -84380070.357924, -38117397.479734				
	16.055193000000, -18.773061902425, -9.4656005258014				
Covariance matrix (EME2000)					
x, km	y, km	z, km	v_x, km/s	v_y, km/s	v_z, km/s
4.198	1.395	$-5.582 \cdot 10^{-2}$	3.352	4.652	$-2.032 \cdot 10^{-1}$
1.395	1.687	$1.087 \cdot 10^{-1}$	1.234	3.250	$-4.346 \cdot 10^{-2}$
$-5.582 \cdot 10^{-2}$	$1.087 \cdot 10^{-1}$	3.787	$-5.172 \cdot 10^{-2}$	$-5.355 \cdot 10^{-2}$	2.051
3.352	1.234	$-5.172 \cdot 10^{-2}$	2.759	3.872	$-1.647 \cdot 10^{-1}$
4.652	3.250	$-5.355 \cdot 10^{-2}$	3.872	7.574	$-2.697 \cdot 10^{-1}$
$-2.032 \cdot 10^{-1}$	$-4.346 \cdot 10^{-2}$	2.051	$-1.647 \cdot 10^{-1}$	$-2.697 \cdot 10^{-1}$	1.428

Table 2.13: *Results and performance of the planetary protection analysis of the launcher upper stage of the Bepi Colombo mission.*

	RK78	GLRK8
Number of impacts	2 (Venus), 5 (Earth)	2 (Venus), 4 (Earth)
Impact probability $P(I)$	$1.29 \cdot 10^{-4}$	$1.11 \cdot 10^{-4}$
Standard deviation σ	$4.89 \cdot 10^{-5}$	$4.53 \cdot 10^{-5}$
Computational time	5.9 h	35.1 h

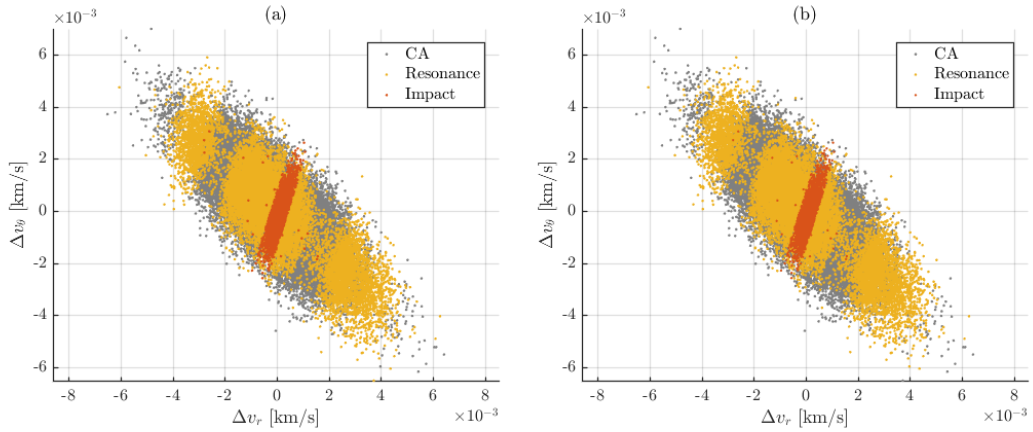

Figure 2.13: *Velocity dispersion (in the radial, Δv_r, and transversal, Δv_θ directions) and trajectory characterisation for the MC analysis on the launcher upper stage of the Solar Orbiter mission, showing the initial conditions leading to a close approach (dark grey), a resonance (yellow) or an impact (red) with Venus or the Earth. In (a) RK78 is used, in (b) GLRK8 is used instead.*

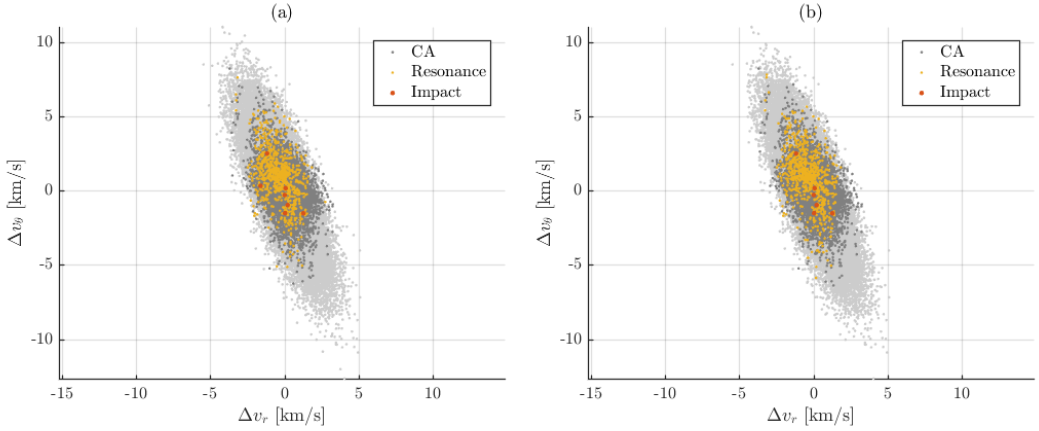

Figure 2.14: *Velocity dispersion (in the radial, Δv_r, and transversal, Δv_θ directions) and trajectory characterisation for the MC analysis on the launcher upper stage of the Bepi Colombo mission, showing the initial conditions leading to a close approach (dark grey), a resonance (yellow) or an impact (red) with Venus or the Earth. In (a) RK78 is used, in (b) GLRK8 is used instead.*

Table 2.14: *Results and performance of the planetary protection analysis of the launcher upper stage of the Solar Orbiter mission.*

	RK78	GLRK8
Number of impacts	2347 (Venus), 1 (Earth)	2348 (Venus), 1 (Earth)
Impact probability $P(I)$	$4.34 \cdot 10^{-2}$	$4.34 \cdot 10^{-2}$
Standard deviation σ	$8.76 \cdot 10^{-4}$	$8.76 \cdot 10^{-4}$
Computational time	6.5 h	81.5 h

To draw a conclusion based on the results of the analyses that were performed to compare the different integration method of 8^{th} order, the implicit GLRK is the one that showed the best performance in all conditions: the method was able to guarantee a better conservation of the value of the Hamiltonian function during the propagation, not only when the distance from the planets was large, but also when close encounters occurred. This is also shown from the analysis of the position and velocity errors in the various cases. For this reasons, further work to improve its use and implementation is recommended.

2.5 Numerical identification of fly-bys

Symplectic methods can achieve conservation of the total energy (as value of the Hamiltonian function) over long integration times. This is true in those cases when the dynamics is non-chaotic or chaotic with long-range interactions during the propagation. However, close approaches with planets, especially very close fly-bys, represent conditions when the non-linearity of the dynamics drastically increases the numerical error on the solution. This is visible as a steep growth of position and velocity errors from the reference values, and of the total energy from the initial value. This generally affects any numerical fixed- or variable-step method, whether symplectic or not.

This kind of problem has been addressed before by many authors, who devised different approaches to overcome or bypass the numerical effects of the fly-bys, by applying ad-hoc numerical techniques only during a close approach (e.g. switching the primary body of the propagation from the main body to the approaching planet [96], or applying the projection technique in order to impose the conservation of energy [89]).

Any devised solution, however, requires a correct identification of the close approach or fly-by conditions to counteract the increase of numerical errors in an effective way, following criteria that should be evaluated automatically during the integration. Again, there exist various possible solutions to accomplish this task (e.g. setting a limit distance from the approaching planet). In this work, another approach is proposed, which considers the behaviour of the dynamics as an automatic criterion to define a close approach during the propagation: here the Jacobian of the equations of motion is used to monitor the evolution of its eigenvalues before and during the encounter with a celestial body, using an approximation similar to the one introduced by Debatin et al. [79]. The advantage of using this approach is the independence from arbitrary choices such as choosing the planet's sphere of influence as distance to define the start

or end of the close approach.

Given the equations of motion $\dot{\mathbf{x}} = \mathbf{f}(\mathbf{x}, t)$, let $\mathbf{x} = (\mathbf{r}, \mathbf{v})^T$ be the state vector, containing position and velocity, and $f(\mathbf{x}, t)$ be equal to $(\mathbf{v}, \dot{\mathbf{v}})^T$. Then the Jacobian matrix is given by

$$\mathbf{J} = \frac{\mathrm{df}}{\mathrm{dx}} = \begin{bmatrix} \mathbf{0} & \mathbf{I} \\ \mathbf{G} & \mathbf{0} \end{bmatrix} \tag{2.27}$$

where $\mathbf{x} = (\mathbf{r}, \mathbf{v})^T$ is the state vector, containing position and velocity vectors, $\mathbf{I}$ is the identity matrix and $\mathbf{G}$ results from the derivation of the gravitational terms defined in Eq. 2.1:

$$\mathbf{G} = \frac{\partial \dot{\mathbf{v}}}{\partial \mathbf{x}} = \sum_{j=0}^{n} \mathbf{G}_j = \sum_{j=0}^{n} \frac{\mu_j}{\|\mathbf{d}_j\|^5} \left(\|\mathbf{d}_j\|^2 \mathbf{I} - 3\mathbf{d}_j \mathbf{d}_j^T \right) \tag{2.28}$$

where $\mathbf{d}_j = \mathbf{r} - \mathbf{r}_j(t)$ and $\mathbf{r}_j(t) = \{x_j, y_j, z_j\}^T$ represents the position of the j-th planet as given by the ephemerides and $\mathbf{G}_j$ is its contribution to the matrix $\mathbf{G}$, with the index $j = 0$ indicating the body of the system with the largest gravitational influence (e.g. the Sun in the case of an interplanetary trajectory).

The set of eigenvalues $\boldsymbol{\lambda}$ of the Jacobian matrix defined in Eq. 2.27 is given by the roots of the characteristic polynomial, written using the properties of the determinant of a square block matrix [97]:

$$\det(\mathbf{J} - \lambda \mathbf{I}) = \det(\lambda^2 \mathbf{I} - \mathbf{G}\mathbf{I}) = \det(\lambda^2 \mathbf{I} - \mathbf{G}) = \det(\lambda^2 \mathbf{I} - \mathbf{G}) = 0 \tag{2.29}$$

In this case, as an approximation, only the contributions to the Jacobian given by each planet alone are considered, using the decomposition of $\mathbf{G}$ introduced in Eq. 2.28:

$$\det(\lambda_j^2 \mathbf{I} - \mathbf{G}_j) = 0, \quad j = 0, ..., n \tag{2.30}$$

with $\boldsymbol{\lambda}_j$ being the set of eigenvalues given by the contribution of j-th planet. Indicating with Λ_j the eigenvalue with the maximum absolute value of such set, the simplified expression proposed by Debatin et al. [79] is used to estimate Λ_j as

$$\Lambda_j = \frac{2\mu_j}{\|\mathbf{r} - \mathbf{r}_j(t)\|^3}, \; j = 0, ..., n \tag{2.31}$$

With this criterion for the detection of close approaches, not only the single eigenvalues are considered, but also their derivative in time:

$$\dot{\Lambda}_j = \frac{\partial \Lambda_j}{\partial t} = \left| -2\mu_j \frac{3(\mathbf{r} - \mathbf{r}_j(t)) \cdot (\mathbf{v} - \mathbf{v}_j(t))}{\|\mathbf{r} - \mathbf{r}_j(t)\|^5} \right| \tag{2.32}$$

The value of the eigenvalue contributions given by the single planets are compared with the one given by the main body, and the same is done for their derivatives. A fly-by event is identified when one or both ratios defined in Eq. 2.33 grows beyond given thresholds ε_1 and ε_2:

$$\begin{aligned} \frac{\Lambda_j}{\Lambda_0} &= \frac{\mu_j}{\mu_0} \frac{\|\mathbf{r} - \mathbf{r}_0(t)\|^3}{\|\mathbf{r} - \mathbf{r}_j(t)\|^3} \geq \varepsilon_1 \\ \frac{\dot{\Lambda}_j}{\dot{\Lambda}_0} &= \frac{\mu_j}{\mu_0} \left| \frac{(\mathbf{r} - \mathbf{r}_j(t)) \cdot (\mathbf{v} - \mathbf{v}_j(t))}{(\mathbf{r} - \mathbf{r}_0(t)) \cdot (\mathbf{v} - \mathbf{v}_0(t))} \right| \frac{\|\mathbf{r} - \mathbf{r}_0(t)\|^5}{\|\mathbf{r} - \mathbf{r}_j(t)\|^5} \geq \varepsilon_2 \end{aligned} \tag{2.33}$$

where the j index indicates a celestial body and the index 0 indicates the main body of the system, which is exerting the largest gravitational influence on the body being propagated. The two ratios represent two different quantities: the first one compares the gravitational attractions of the approached body with the one of the central body of the system, thus considering only their relative distance, similarly to the definition of the SOI; the second one, on the other hand, compares not only the gravitational influences of the two bodies, but also their relative velocities with the propagated body, projected onto the relative directions. This allows to define the close approach taking into account the actual dynamics of the encounter, instead of simply setting a relative distance or relative velocity threshold.

For the application of this method, one or both expressions (ratio of the values and ratio of the derivatives of the eigenvalues) can be used, separately or together.

An example of the application of this method can be seen in Figure 2.15, which shows the case of two close approaches between the launcher upper stage of the Solar Orbiter spacecraft and Venus. In both cases the variations of the eigenvalues and of their derivatives (are compared with the crossing of the sphere of influence (SOI) and Hill's sphere [98] of Venus, to show the differences between the two criteria.

Figure 2.15 shows the variation in time of the eigenvalues relative to Venus and the Sun and their associated derivative (respectively lower left and right) during the propagation of the nominal trajectory of the launcher upper stage of Solar Orbiter, with the distance between the two bodies as a reference (upper plot). In both cases, the comparison is done on the 100 years propagation (top), with a focus on the 1st close approach with Venus during the first year of the mission (centre), and on a second close approach 80 years later (bottom). In both graphs, different information is reported: the red and green areas represent, respectively, the crossing of the SOI and the Hill sphere of Venus; the vertical dashed lines indicate the epochs where the ratios defined in Eq. 2.33 are both equal to 1.0 (only one value is used for both ratios for simplicity).

The plots show that both close approaches can be successfully identified using the definitions defined previously. In particular, a threshold value of 1.0 for the ratios in 2.33 correctly identifies the not only the first CA (where an actual crossing of the SOI occurs), but also the second one, which happens at a larger distance from Venus, with no SOI crossing. This is possible due to the information about the relative velocity between the propagated body and the planet contained in the derivative in Eq. 2.32.

Note also that tolerances equal to 1.0 allow to determine initial and final epochs for the close approach in a broader sense than the ones defined by the SOI and Hill sphere crossings, particularly for the derivative ratio, meaning that a lower value can be also used in the case of interplanetary trajectories. On the other hand, a larger tolerance can be used to detect close approaches with great advance, or detect conditions which may affect the quality of the numerical integration even without a close fly-by.

Figure 2.16 shows the the results of the propagation of the trajectory of the Juice spacecraft around Jupiter in terms of distance from the Galilean moons (a), variation of eigenvalues (b), and variation of the derivatives for the eigenvalues (c). The propagation was carried out using the initial conditions and integrator setup reported in Table 2.15. From it is possible to observe that the Juice spacecraft encounters multiple times the moons Europa, Ganymede, and Callisto, performing several fly-bys and close ap-

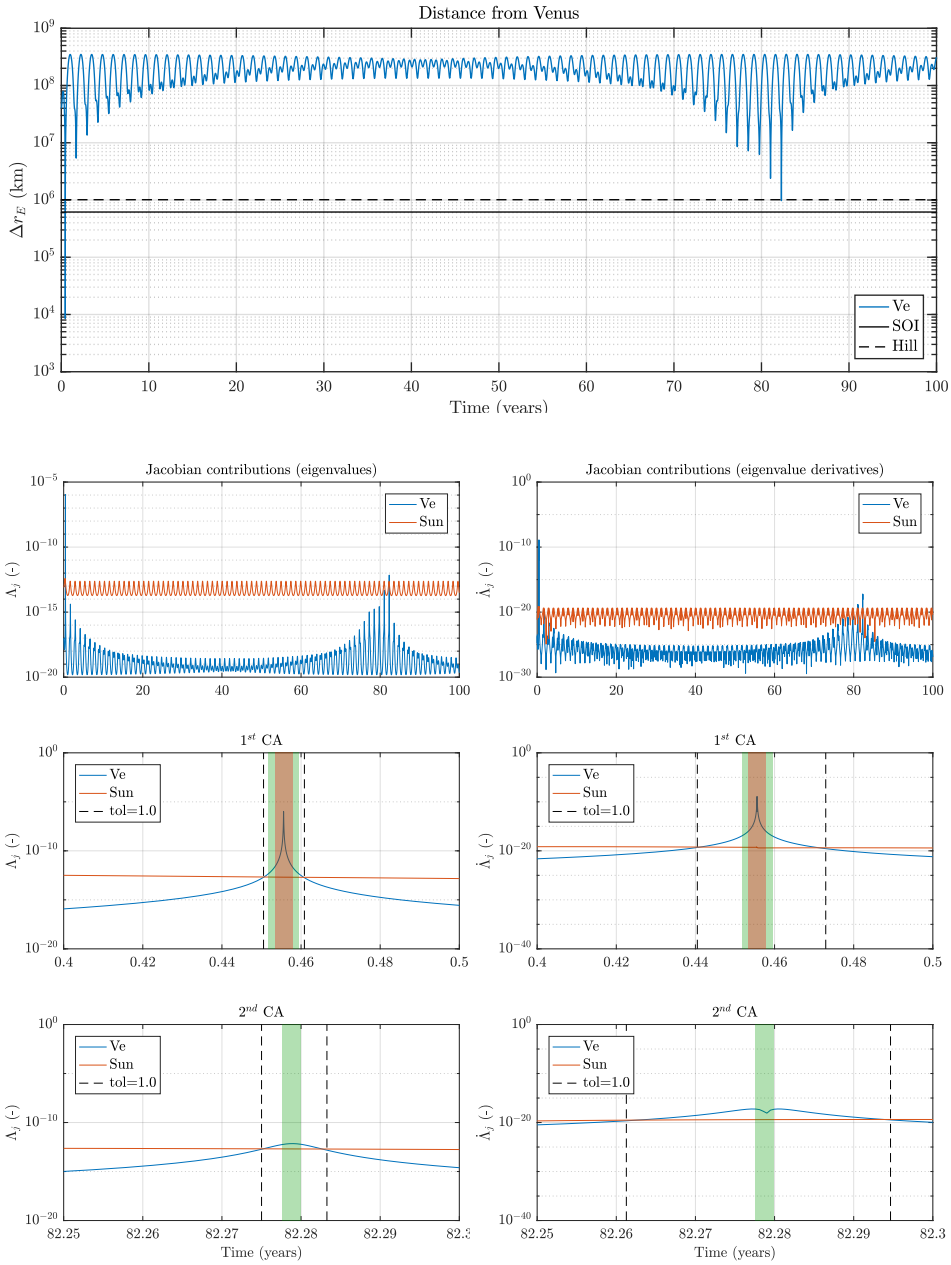

Figure 2.15: *Upper plot: distance of the Solar Orbiter launcher upper stage from Venus during the propagation. Lower plots: variation in time of the eigenvalues corresponding to the single contribution of the Sun and Venus during the propagation of the nominal trajectory of Solar Orbiter's launcher upper stage, with values (left) and derivatives (right) of the eigenvalues, compared with the crossing of SOI (red area) and Hill sphere (green area) of Venus. The vertical dashed lines refer to the epochs where the ratio between the eigenvalues of Venus and the Sun is equal to 1.0.*

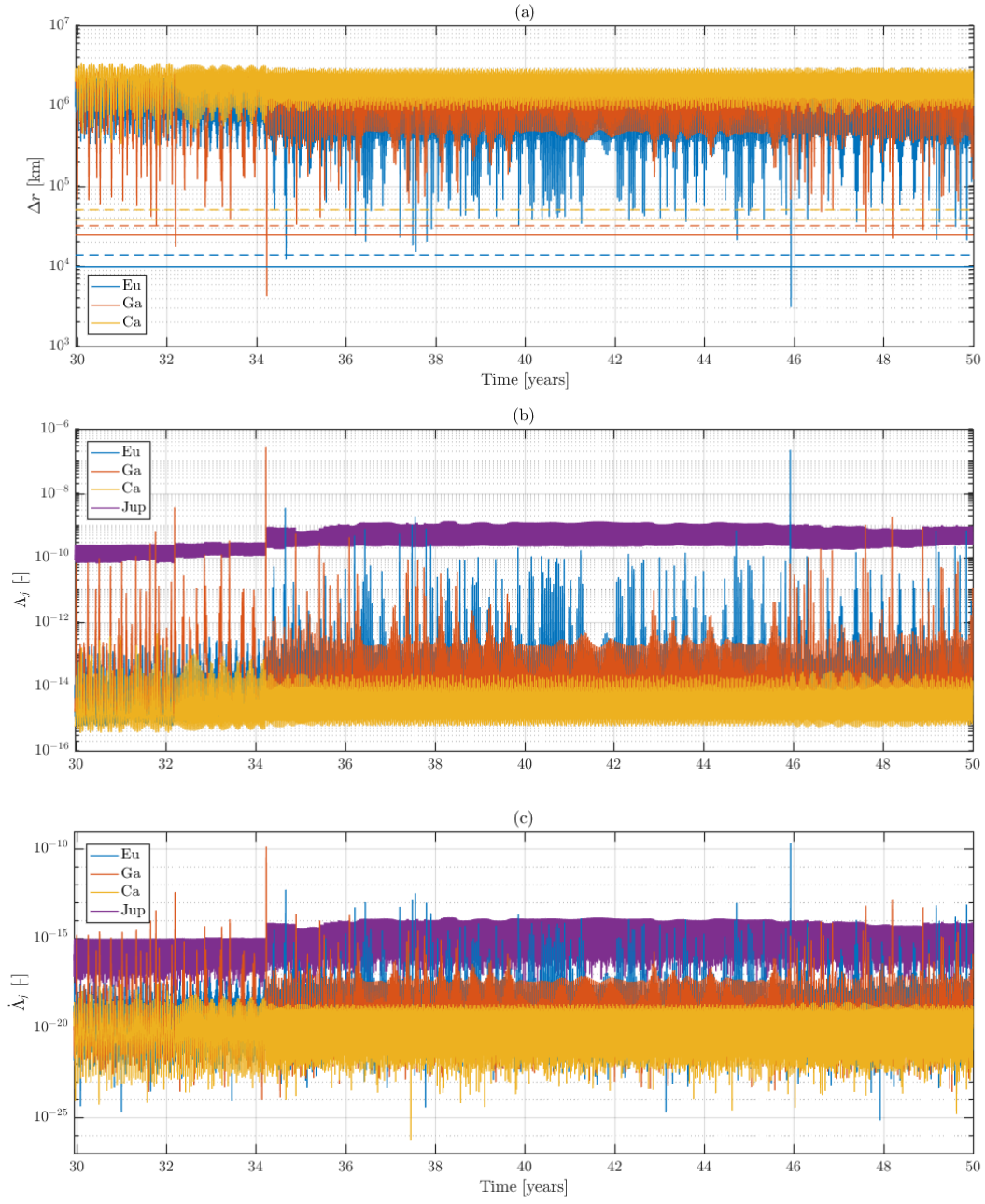

Figure 2.16: *(a) Distance of Juice from the Jovian moons Europa (blue), Ganymede (red), and Callisto (yellow) during the propagation. (b) Variation in time of the eigenvalues corresponding to the single contribution of Jupiter (purple) and the moons during the propagation of the trajectory of Juice. (c) Variation in time of the eigenvalue derivatives corresponding to the single contribution of Jupiter (purple) and the moons during the propagation of the trajectory of Juice.*

proaches during the 20 years of the propagation shown in the Figure. In the top plot, the continuous and the dashed horizontal lines represent the SOI and the Hill sphere radius for each moon, respectively. By comparing those values with the distances from the moons, it is possible to notice how in many cases the spacecraft just skims a SOI or Hill sphere, thus coming close to a moon but without performing a full close fly-by.

Table 2.15: *Initial conditions and integrator setup for the propagation of the trajectory of the JUICE spacecraft.*

Initial epoch, MJD2000	11915.28114
Initial position, km	$1.10613 \cdot 10^6$, $1.33233 \cdot 10^5$ $8.75564 \cdot 10^4$
Initial velocity, km/s levels	-2.2709, 10.08696, 5.07097
Reference frame	EME2000 centred at Jupiter
Area-to-mass ratio, m^2/kg	0.01
Reflection coefficient, adim.	1.0
Propagation length	50 years
Integrator	RK78
Absolute and relative tolerances	10^{-12}
Ephemerides	JPL Horizons (SPICE toolkit)

Due to the high number of encounters with the moons, no close-up picture of the single close approaches is reported, but details of two one-year long intervals are shown in Figures 2.17 and 2.18. From the observation of these plots, it is clear that the eigenvalue criteria are able to identify also those situations where the spacecraft does not enter the SOI or Hill sphere of a moon. In such cases, both the eigenvalue contributions (value and associated derivative) given by the encountered moon have values that are significantly higher or at least comparable to the contributions given by Jupiter.

2.6 Summary

In this chapter a comparison of various numerical integration methods was presented with the goal of showing how the accumulation of approximation errors during a single propagation affect the whole planetary protection analysis.

A first selection of high-order methods was proposed based on the different properties characterising them (e.g. the conservation of integrals of the motion in case of symplectic methods, or the adaptability of the time step in case of embedded schemes), including: standard Runge-Kutta methods (RK), Runge-Kutta methods based on Gauss-Legendre quadrature (GLRK), Runge-Kutta-Nystrom methods (RKN), and the symplectic Yoshida method (SY). This selection was then narrowed down to the most accurate schemes among the proposed ones via the study of their numerical accuracy in the context of planetary protection analyses of interplanetary missions, as well as of single propagations of asteroid trajectories: the latter were considered due to their resonant close passages to the Earth's orbit and to the availability of the SPICE ephemerides computed by the JPL to be used as a reference.

The results of the tests pointed out that the use of symplectic integration can be

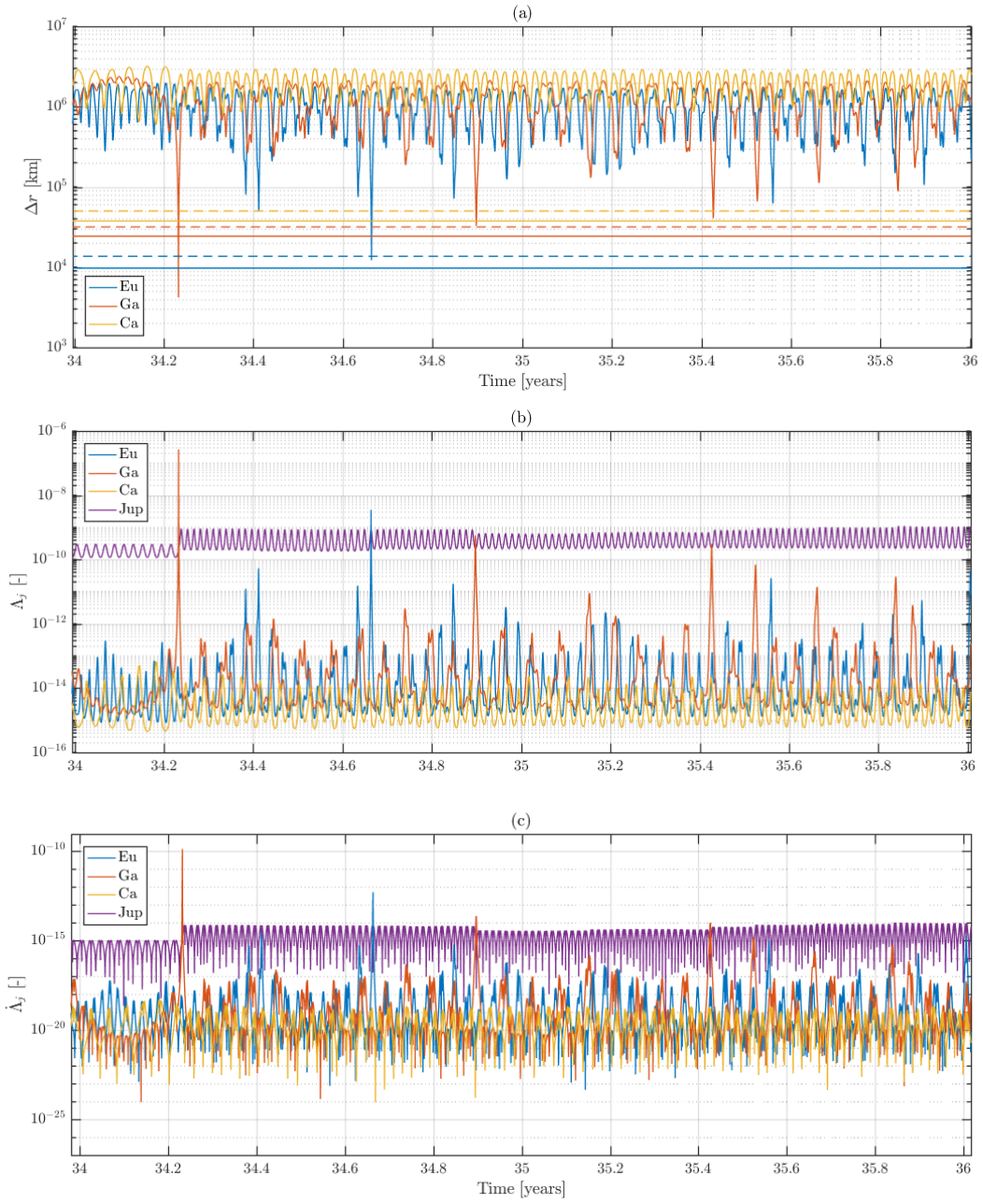

Figure 2.17: *Details of the plots in Figure 2.16 showing how the trajectory is subject to close approaches according to the proposed definition even if no crossing of the SOI (continuous lines) and of the Hill spheres (dashed horizontal lines) occur.*

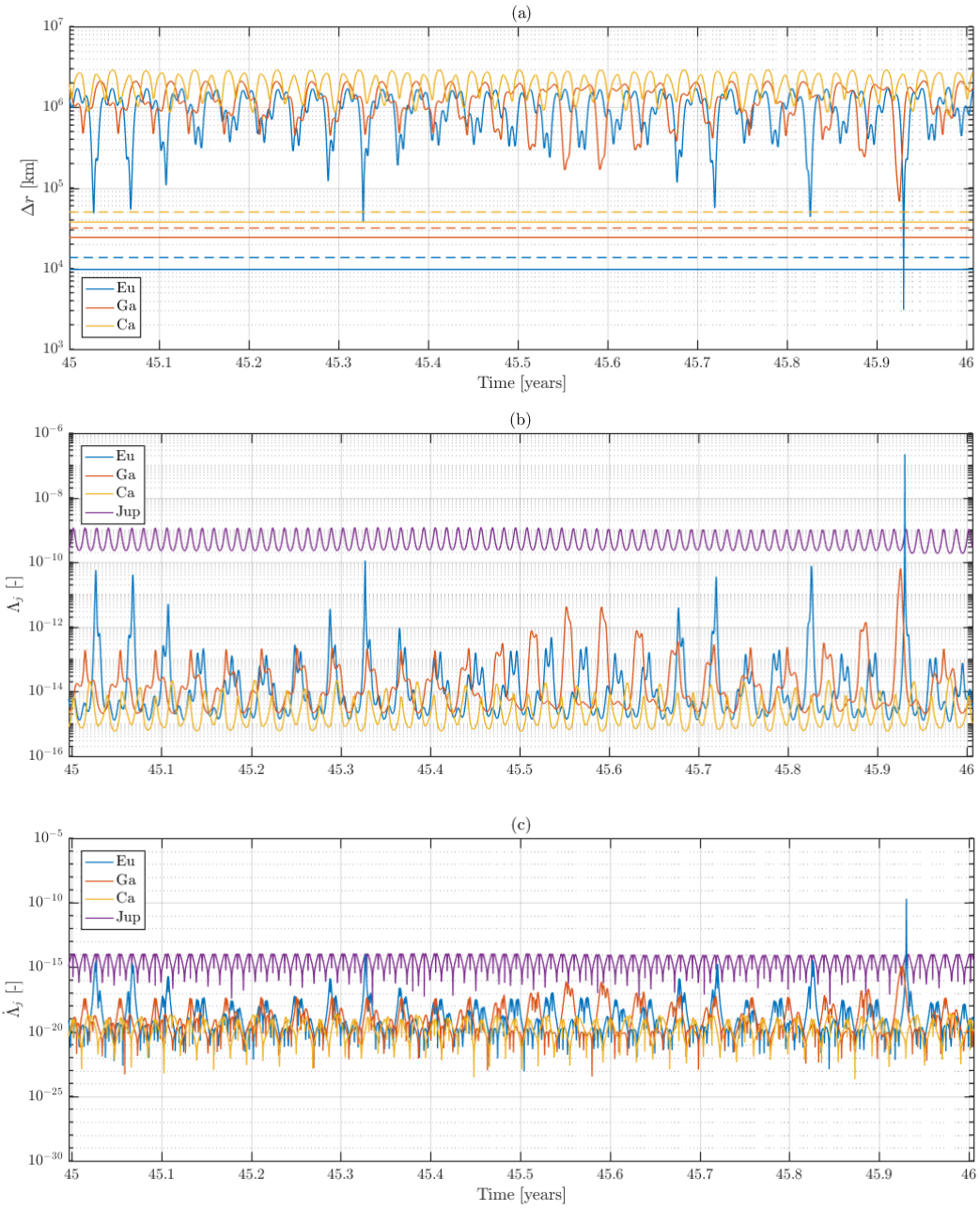

Figure 2.18: *Details of the plots in Figure 2.16showing how the trajectory is subject to close approaches according to the proposed definition even if no crossing of the SOI (continuous lines) and of the Hill spheres (dashed horizontal lines) occur.*

beneficial to the propagation, even when this is carried out in a n-body environment: when the distance between the small body being propagated and any planet is large, the symplectic formulation can keep the total energy of the system in bounded oscillation without a secular drift (which is present in case of non-symplectic methods), with a higher accuracy. The application to statistical analysis, finally, showed that the MC simulation is not affected by the selection of the integration method, thus allowing the application methods which were proved more accurate for single propagations method without suffering a loss of accuracy on a statistical level.

The tests also pointed out that numerical issues arise during close approaches and fly-bys, with steep rises in the energy and state errors, in a comparable way for symplectic and non-symplectic methods. The application of different techniques during these events can help in facing the higher non-linearity of the dynamics. For this reason, a criterion for identifying the conditions of fly-by during the propagation was devised, in order to recognise autonomously the conditions that trigger numerical error. This criterion uses the eigenvalues of the Jacobian matrix of the equations of motion to approximate the behaviour of the dynamics, and recognise when its non-linearity increases due to a close approach with a planet. The tests presented in this chapter showed that this method is more effective in recognising a close approach even when there is no clear crossing of the sphere of influence, thanks to a more general definition taking into account the relative velocity between the propagated object and the celestial body.

CHAPTER 3

Uncertainty sampling techniques and application to planetary protection

3.1 Introduction

Planetary protection policies require to verify that the probability of contaminating a celestial body due to non-scheduled impacts from mission-related objects is below a given threshold for any interplanetary mission. The maximum acceptable impact probability and the confidence level associated with it depend on the class of mission under examination [2], spanning from 10^{-3} up to 50-100 years after launch for a generic Mars mission, to 10^{-6} for sample return missions or missions to the Jovian moons, with a minimum confidence level of 99%.

Since the probability levels to be verified are generally low, the analysis can require a large number of orbital propagations with standard Monte Carlo simulations, resulting in high computational cost and time: the number of simulations required to estimate the probability, indeed, increases as the expected probability decreases and the confidence level to be guaranteed increases. For this reason, more efficient sampling methods were studied to increase the precision of the probability estimate, or reduce the amount of simulations, and thus the computational cost. The doctoral research focused on the Line Sampling method, which was chosen as alternative to standard Monte Carlo for application to planetary protection analysis after various comparisons with this and other methods, as it will be shown in section 3.4.4.

The Line Sampling (LS) method is a Monte Carlo-based approach for the estimation of small probabilities. It was originally developed for the reliability analysis of failure in complex structural systems [80, 99], and later applied to risk estimation for orbital conjunction analysis in combination with DA [53]. In this work, the method was adapted and applied to the estimation of impact probability of small objects with

major celestial bodies, mainly for the verification of planetary protection requirements for exploration missions, but including also Near Earth Asteroids [59, 100].

The main feature of the Line Sampling method is the analytical estimation of the probability, obtained by reducing the multi-dimensional integration problem across the uncertainty domain to many one-dimensional integrals along lines following a reference direction that are used to sample the initial distribution; this direction is determined so that it points toward an impact region of the domain (that is, a subset of initial conditions that will lead to an impact with a celestial body), and, if this is properly chosen, the method can considerably increase the accuracy of the solution or reduce the number of required system simulations with respect to a standard MC. Other advanced sampling methods were also considered, such as Subset Simulation (SS) [80, 101–103], which computes the impact probability as the product of larger conditional probability by progressively identifying intermediate conditional levels moving toward the impact event, reducing the overall number of samples that need to be evaluated. A comparison between SS and LS is presented in Section 3.4.4 as part of a work in collaboration with the Ph.D. Candidate Matteo Losacco, who developed and implemented the SS algorithm. This comparison serves to justify the choice of LS over SS due to its higher accuracy in estimating the small probabilities characterising the planetary protection problem.

Novelties

This chapter presents, in the first part, the LS algorithm and the theory behind it, studying the formulation that is given in the literature. This theoretical formulation was expanded further in order to better characterise the behaviour of the method according to the cases under analysis.

Later, a series of algorithms based on LS are introduced with the aim of creating a numerical procedure capable of analysing complex cases:

- an algorithm used to improve a first guess for the reference sampling direction to get it closer to an ideal case, thus increasing the accuracy of the analysis;
- an algorithm to identify time windows where impact regions could be found by analysing the close approaches that are recorded during a preliminary sampling;
- an iterative procedure to explore all possible impact regions and sample them if possible, with the goal of obtaining a wider overview of the distribution of impact regions within the initial uncertainty distribution, and estimating impact probability with higher accuracy and efficiency.

Two test cases regarding planetary protection analysis of interplanetary missions are provided with their results, as examples to demonstrate the performances of the presented techniques singularly or in the context of the overall procedure: the launcher upper stage of the Solar Orbiter mission, and orbiter of the Mars Sample Return mission. An additional test case represented by asteroid 99942 Apophis is reported to show the comparison between the LS and SS methods, and their performance with respect to standard MC.

3.2 Theory of Line Sampling for uncertainty sampling

3.2.1 The Line Sampling algorithm

The LS method is a Monte Carlo-based approach with the objective of estimating small probabilities (probabilities of failure that are generally in the range of $10^{-7} - 10^{-6}$ [80, 99]). It consists of four steps: 1) the mapping of random samples from the physical coordinate space into a normalised standard space; 2) the determination of the reference direction $\boldsymbol{\alpha}$; 3) the probing of the impact region along the lines following the reference direction; 4) the estimation of the impact probability. A summary of each step is provided hereafter, along with an introduction to the choices made for the numerical implementation of the LS technique.

Mapping onto the standard normal space

The first step of the LS procedure is the definition of this transformation: all the random vectors $\boldsymbol{x} \in R^n$ of physical coordinates (position and velocity) that are drawn from the nominal uncertainty distribution in the following phases need to be mapped onto a normalised coordinate space.

Each $\mathbf{x}$ vector is mapped to a new parameter vector $\boldsymbol{\theta} \in R^n$ whose components $\theta_j,\ j = 1, ..., n$ are all associated with a unit Gaussian distribution, each with a probability density function (pdf) ϕ_j defined as:

$$\phi_j(\theta_j) = \frac{1}{\sqrt{2\pi}} \exp\left(-\frac{\theta_j^2}{2}\right),\ j = 1, ..., n \tag{3.1}$$

The components of the vector $\boldsymbol{\theta}$ have the property of being independent and identically distributed (iid) random variables, meaning that each has the same probability distribution as the others and all are mutually independent [80]. As a consequence, the joint pdf ϕ of these random parameters is equal to the product of all the single pdfs:

$$\phi(\boldsymbol{\theta}) = \prod_{j=1}^{n} \phi_j(\theta_j) \tag{3.2}$$

Thanks to this property, this transformation grants efficiency to the method, especially for problems with high dimensionality: it reduces the problem to a series of one-dimensional analytical evaluations, thus enabling a simplification of the computation of the probability later in the procedure.

The direct and the inverse transformations, from the physical domain to the normalised one and vice versa, preserve the joint Cumulative Distribution Function (CDF) between the two coordinate spaces, and are defined as:

$$\Phi(\boldsymbol{\theta}) = F(\mathbf{x}) \tag{3.3}$$

$$\boldsymbol{\theta} = \Phi^{-1}[F(\mathbf{x})] \tag{3.4}$$

$$\mathbf{x} = F^{-1}[\Phi(\boldsymbol{\theta})] \tag{3.5}$$

with Φ and F being the CDF of the unit Gaussian distribution and the input uncertainty distribution of the problem, respectively.

Following the definition of the pdf ϕ, the joint CDF Φ is

$$\begin{aligned} \Phi(\boldsymbol{\theta}) &= \int_{-\infty}^{\boldsymbol{\theta}} \phi(\boldsymbol{u})\mathrm{d}\mathbf{u} = \prod_{j=1}^{n} \Phi_j(\theta_j) \\ \text{with } \Phi_j(\theta_j) &= \frac{1}{2}\left[1 + \text{erf}\left(\frac{\theta_j}{\sqrt{2}}\right)\right],\ j = 1, ..., n \end{aligned} \tag{3.6}$$

where $\text{erf}(x) = \frac{2}{\sqrt{\pi}} \int_0^x \exp\left(-u^2\right)\mathrm{d}u$ is the error function.

The Rosenblatt transformation [104] is applied in this work, since, for Gaussian-distributed uncertainty parameters (as in the cases under study), both the direct and the inverse transformations (respectively Equations 3.4 and 3.5) become linear [80, 104]. The transformation is reported in Appendix B, along with other similar mappings between physical and standard normal coordinates that were implemented for this work.

Determination of the reference sampling direction

The reference sampling direction $\boldsymbol{\alpha}$ can be determined in different ways. Zio et al. [80, 81] show interpretations of $\boldsymbol{\alpha}$ as the direction of a "design point" in the standard normal space, or of a normalized gradient of a performance function in the standard normal space, or of the normalized "center of mass" of the domain of interest. In this work, the latter solution is adopted, using the impact region as the domain of interest.

This region is approximated by applying the Metropolis-Hastings algorithm [105, 106] to generate a Markov Chain Monte Carlo (MCMC) lying entirely in the impact subdomain starting from an initial condition within it. MCMC simulation is a method for generating samples conditional on a region satisfying a given condition, according to any given probability distribution described by the pdf $p(\mathbf{x})$.

The starting condition of the MCMC can also be found in different ways (e.g. numerical minimisation of the distance to the planet, or prior knowledge). In this work, the initial point is determined via a preliminary sampling, as will be described in Section 3.3. It is important to notice that the specific method used to determine the sampling direction is not a core phase of the LS method, thus representing one of the degrees of freedom in the implementation of the whole procedure.

After the impact region has been populated with N_S samples, the reference direction $\boldsymbol{\alpha}$ is computed in the standard normal space as

$$\boldsymbol{\alpha} = \frac{1}{N_S} \sum_{u=0}^{N_S} \frac{\boldsymbol{\theta}^u}{||\boldsymbol{\theta}^u||} \tag{3.7}$$

where $\boldsymbol{\theta}^u,\ u = 1, ..., N_S$ are the points of the MCMC found inside the impact region, after being converted from the physical space into the standard normal space. The simulations performed for the Markov chain require additional computational effort with respect to standard MC methods. Nevertheless, this option provides a good coverage of the impact region and a resulting better accuracy of the final probability estimate.

Metropolis-Hastings algorithm for MCMC The algorithm to generate a sequence of N_S samples from a given sample $\mathbf{x}_1$ is briefly explained [101]:

1. from the current element $\mathbf{x}_u$, $\boldsymbol{\xi}$ is generated by randomly sampling a user-defined "proposal" pdf $p^*(\mathbf{x}_u)$;

2. compute the ratio $r = p(\boldsymbol{\xi})/p(\mathbf{x}_u)$;

3. set $\tilde{\mathbf{x}} = \boldsymbol{\xi}$ with probability $\min(1, r)$ and set $\tilde{\mathbf{x}} = \mathbf{x}_u$ with the remaining probability $1 - \min(1, r)$, where $\tilde{\mathbf{x}}$ is the candidate for the next element of the chain;

4. check whether the candidate $\tilde{\mathbf{x}}$ lies in the region of interest I or not: if $\tilde{\mathbf{x}} \in I$, accept it as the next sample $\mathbf{x}_{u+1} = \tilde{\mathbf{x}}$; else, reject it and take the current sample as the next sample $\mathbf{x}_{u+1} = \mathbf{x}_u$.

In this work, the "proposal" pdf $p * (\mathbf{x}_u)$ is determined by scaling the nominal pdf (which represents the initial uncertainty distribution) with a factor $f < 1$ to draw values as close to the impact region as possible. On the other hand, possible criteria for the choice of the number N_S of elements of the chain are discussed in Section 3.3.2.

Line sampling

After determining the reference sampling direction, N_T initial conditions $\boldsymbol{x}^k,\ k = 1, ..., N_T$ are randomly drawn from the nominal uncertainty distribution and then mapped to standard normal coordinates as $\boldsymbol{\theta}^k$ using the transformation in Eq. 3.4. For each sample in the standard normal space, a line starting from $\boldsymbol{\theta}^k,\ k = 1, ..., N_T$ and parallel to $\boldsymbol{\alpha}$ is defined according to the parameter c^k, such that

$$\boldsymbol{\theta}^k = c^k \boldsymbol{\alpha} + \boldsymbol{\theta}^k_\perp \tag{3.8}$$

$$\boldsymbol{\theta}^k_\perp = \boldsymbol{\theta}^k - \langle \boldsymbol{\alpha}, \boldsymbol{\theta}^k \rangle \boldsymbol{\alpha} \tag{3.9}$$

where $\langle \boldsymbol{\alpha}, \boldsymbol{\theta}^k \rangle$ is the scalar product between $\boldsymbol{\alpha}$ and $\boldsymbol{\theta}^k$. In this way, the problem is reduced to a series of one-dimensional evaluations associated with each sample, with c^k normally distributed in the standard space.

The standard domain is then explored along each line with the aim of identifying the impact region of an uncertainty set. For the problem under study, the occurrence of the events is expressed by the value of the non-dimensional performance function

$$g_\theta\left(\boldsymbol{\theta}(c)\right) = Y(c)/R_{imp} - 1 \tag{3.10}$$

where Y is a function that maps the value of the parameter c (corresponding to an initial condition $\mathbf{x}_0$) to a performance index, and R_{imp} is the selected critical distance. In this work, Y is the minimum distance from the celestial body of interest (e.g. the Earth) in the given time window, while R_{imp} represents the radius around the planet that is selected to define an impact (not necessarily equal to the planet radius). According to this definition, it follows that

$$g_\theta(\boldsymbol{\theta}(c)) \begin{cases} < 0 \rightarrow \text{Impact} \\ = 0 \rightarrow \text{Limit condition} \\ > 0 \rightarrow \text{No impact} \end{cases} \tag{3.11}$$

The limit condition $g_\theta(\boldsymbol{\theta}(c)) = 0$ is given by a trajectory reaching a minimum distance from the planet equal to the impact radius R_{imp} (the trajectory can be seen as "brushing" against the surface of the planet, while it enters its surface in the case of an impact).

The performance function is evaluated iteratively along each line $\boldsymbol{\theta}^k = c^k \boldsymbol{\alpha} + \boldsymbol{\theta}^k_\perp$ to identify the values of c^k corresponding to its intersections with the impact region, as displayed in Fig. 3.1. Due to the nature of the problem under analysis (that is, a single close approach event within a given time interval), the hypothesis if made that a maximum of two intersections between each line and the impact region are found, meaning that two values of c^k exist for each standard normal random sample $\boldsymbol{\theta}^k,\ k = 1, ..., N_T$ where the performance function is equal to zero: $g_\theta(\overline{c}^k_1) = 0$ and $g_\theta(\overline{c}^k_2) = 0$. These two values represent states leading to the limit condition, while the values of c^k in between represent states leading to impacts: $g_\theta(\overline{c}^k) = 0, \forall\ \overline{c}^k_1 < c^k < \overline{c}^k_2$. The main hypothesis is valid when the impact region extends across the uncertainty domain and can be approximated as a flat or slightly curved surface. On the contrary, if the impact region is limited in size, the line being sampled may not intersect the impact region and no root c^k is found. Finally, if the impact region has a twisted shape or disconnected shape due to many close approaches, more than two intersections (or none) with each line may be found.

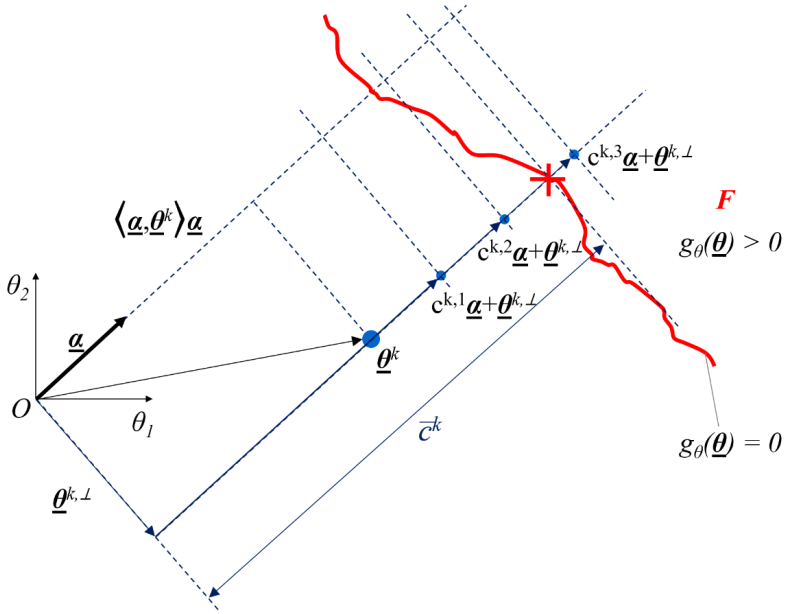

Figure 3.1: *Scheme of the iterative sampling procedure used to sample each line in the standard normal coordinate space. The impact region is labelled with F, with a single border highlighted as a red line.*

Iterative algorithm An iterative process is used to identify the intersections $(\overline{c}^k_1, \overline{c}^k_2)$, thus requiring extra propagations for each random sample $\boldsymbol{\theta}^k,\ k = 1, ..., N_T$ with respect a standard MC simulation. The method adopted here makes use of repeated interpolations of the performance function $g_\theta(\overline{c}^k)$ in order to obtain approximations of

the roots $(\overline{c}_1^k, \overline{c}_2^k)$ that get closer to the actual boundaries of the impact region at each iteration. In this algorithm, $g_\theta(\overline{c}^k)$ is supposed to have a parabola-like shape.

The procedure for a single line $\boldsymbol{\theta}^k = c^k\boldsymbol{\alpha} + \boldsymbol{\theta}_\perp^k$ is described as follows, and it is shown in Fig. 3.2:

1. values c_1,c_2, and c_3, corresponding to three points on the line, are selected based on the information about the impact region gained via the MCMC;

2. the corresponding initial states $\mathbf{x}_1$,$\mathbf{x}_2$, and $\mathbf{x}_3$ are obtained and propagated, evaluating the performance function at each point along the line as $g_\theta(c_1)$,$g_\theta(c_2)$, and $g_\theta(c_3)$;

3. a parabolic interpolation is performed over the three points and the associated values of $g_\theta(c)$ as $g(c_i) = a(c_i)^2 + b(c_i) + c,\ i = 1, 2, 3$, obtaining a linear system of three equations to be solved with the coefficient a, b, and c of the parabola as unknowns;

4. the roots (if any) of the interpolating parabola are searched:

   - if $\Delta = b^2 - 4ac \geq 0$, the two new roots exist, and they are computed as the solutions c_4 and c_5 of the quadratic equation with coefficients a, b, and c;
   - else, the minimum of the interpolating parabola is computed as $c_4 = -b/2a$ (this choice is made to obtain a new point useful for the next interpolation even in case no roots are found);

5. the performance function is evaluated at the new point(s) obtaining $g_\theta(c_4)$ (and $g_\theta(c_5)$);

6. out of the current four (or five) points, the three ones with the lowest value of the performance function are selected to repeat the interpolation;

7. the procedure is repeated from point 1 until a stopping condition is met.

The iterative process is stopped when one of three conditions is reached:

- a given maximum number of iterations is reached;

- a given maximum number of propagations is reached;

- the relative difference between the new guess of the roots (if any) and the previous one falls below a given tolerance (meaning that the guesses stop changing so much at each iterations):

$$\max(|c_4^{new} - c_4/|c_4|, |c_5^{new} - c_5|/|c_5|) \geq \varepsilon$$

- the value of the performance function evaluated at the new guess of the roots is below a given tolerance (meaning that the guesses are close enough to the zeros):

$$\max(|g_\theta(c_4^{new})|, |g_\theta(c_5^{new})|) \geq \delta$$

At the end of the process, the last valid guess of (c_4, c_5) is selected as estimates of $(\overline{c}_1^k, \overline{c}_2^k)$ to represent the intersections between the sampling line and the boundaries of the impact region. When no solution is found (whether because there are no zeros or because the algorithm was stopped before finding a guess), it is considered that the line does not intersect the impact region, and its contribution to the total impact probability will be counted as null.

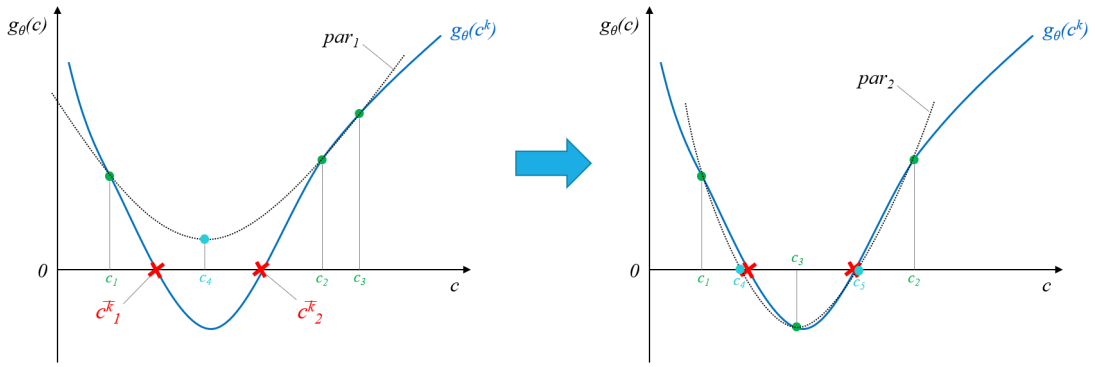

Figure 3.2: *Scheme representing two consecutive iterations of the algorithm designed to search for the roots of the performance function $g_\theta(\overline{c}^k)$ along a single sampling line. The blue curve represents the actual trend of $g_\theta(\overline{c}^k)$, the green dots represent the points used to compute the interpolating parabola (represented as a black dotted line), while the cyan dots represent the guesses used to skip to the next step, either the minimum of the parabola (as in the first step on the left) or two zeroes (as in the second step on the right).*

The choice of this approach over other root-finding algorithms is due to the hypothesis that more than one intersection can be found along each line: this implies that the performance function is not monotone along the sampling line, thus showing points where the derivative is null, and has multiple roots. This condition doesn't allow the use of numerical methods such as Newton's and fixed-point. Moreover, the derivative of $g_\theta(\overline{c}^k)$ for Newton's method would either be approximated numerically, using two propagations (e.g. in a forward scheme), or obtained via the integration of the variational equations (which requires the propagation of the state transition matrix), with an excessive increase in complexity and computational cost. Finally, the need to compute both roots at the same time with numerical efficiency, since each function evaluation requires an orbital propagation.

Estimation of the impact probability

Once the values $(\overline{c}_1^k, \overline{c}_2^k),\ k = 1, ..., N_T$ are known for all the sampling lines, the unit Gaussian CDF provides each random initial condition $\boldsymbol{\theta}^k,\ k = 1, ..., N_T$ with the conditional impact probability $\hat{P}^k(I)$. Thanks to the properties of the normalised coordinate space, each $\hat{P}^k(I)$ can be computed as a one-dimensional integrals along the

corresponding line:

$$\begin{aligned}\hat{P}^k(I) &= \hat{P}[\overline{c}_1^k < N(0,1) < \overline{c}_2^k] \\ &= \int_{\overline{c}_1^k}^{\overline{c}_2^k} \phi(u)\mathrm{d}u = \Phi(\overline{c}_2^k) - \Phi(\overline{c}_1^k),\ k = 1, ..., N_T\end{aligned} \tag{3.12}$$

If no intersections between a sampling line and the impact region were found, the value of the probability integral is equal to 0, and the associated conditional impact probability has a null contribution to the total probability.

The total probability of the event $\hat{P}(I)$ (which is identified with a planetary collision in the approach presented in this work) and the associated variance $\hat{\sigma}^2(\hat{P}(I))$ are then approximated as follows:

$$\hat{P}(I) = \frac{1}{N_T}\sum_{j=1}^{N_T}\hat{P}^k(I) \tag{3.13}$$

$$\hat{\sigma}^2(\hat{P}(I)) = \frac{1}{N_T(N_T-1)}\sum_{j=1}^{N_T}(\hat{P}^k(I) - \hat{P}(I))^2 \tag{3.14}$$

The total probability is estimated as the average of the conditional probabilities computed along each line (including those not intersecting the impact region as having a null partial probability). The variance is computed as the variance of all the conditional probabilities.

The number N_T of sampling lines should be chosen to guarantee a desired level of accuracy, according to the equations given above. Possible criteria to guide this choice are discussed in Section 3.3.2.

Equations 3.13 and 3.28 are presented here for a single impact region, but they can be easily generalised to the multi-impact case, which will be covered in Section 3.3. In such a case, the overall probability is computed as the average of the probabilities of each impact event weighted on the corresponding number of sampling lines.

As an example, consider a case where two non-overlapping impact regions I_1 and I_2 are found in the initial uncertainty domain. They are sampled separately using N_1 and N_2 lines obtaining the probability estimates $\hat{P}(I_1)$ and $\hat{P}(I_2)$, respectively:

$$\hat{P}(I_1) = \frac{1}{N_1}\sum_{k=1}^{N_1}\hat{P}^k(I_1) \qquad \hat{P}(I_2) = \frac{1}{N_2}\sum_{k=1}^{N_2}\hat{P}^k(I_2)$$

$$N_1\hat{P}(I_1) = \sum_{k=1}^{N_1}\hat{P}^k(I_1) \qquad N_2\hat{P}(I_2) = \sum_{k=1}^{N_2}\hat{P}^k(I_2)$$

Given the properties of the standard normal coordinate space introduced in Section 3.2.1, the conditional impact probabilities $\hat{P}^k(I_1)$ and $\hat{P}^k(I_2)$ obtained by evaluating the integrals in Eq. 3.12 can be summed together:

$$\begin{aligned}\sum_{k=1}^{N_1+N_2}\hat{P}^k(I_1 \cup I_2) &= \sum_{k=1}^{N_1}\hat{P}^k(I_1) + \sum_{k=1}^{N_2}\hat{P}^k(I_2) \\ &= N_1\hat{P}(I_1) + N_2\hat{P}(I_2)\end{aligned}$$

This allows to compute the total impact probability of the two events $\hat{P}(I_1 \cup I_2)$ as the average of all the conditional impact probabilities, similarly to the single impact case:

$$\hat{P}(I_1 \cup I_2) = \frac{N_1 \hat{P}(I_1) + N_2 \hat{P}(I_2)}{N_1 + N_2} \tag{3.15}$$

The expression of the variance $\hat{\sigma}^2(\hat{P}(I_1 \cup I_2))$ is obtained in a similar way.

This can be easily generalised for any number of impact regions.

3.2.2 Theoretical formulation of the LS method

The aim of this section is to give an introduction of the theoretical formulation of the LS method. In particular, it provides the analytical demonstration that LS has higher accuracy than standard MC. This treatise follows the explanation and the notation presented by Zio in [81], but is necessary in order to introduce the work presented in the next section.

In section 3.2.3, the theory presented here will be expanded, in order to characterise further the performance of LS with respect to standard MC. In particular, an approximated formula will be developed, showing how the accuracy of LS is related to the choice of the reference sampling direction and to the shape of the impact region being sampled.

As a short premise, the definitions of some relevant quantities will be given in order to exploit them to introduce the theoretical development of the LS method.

Let $\mathbf{X} \in \mathbb{R}^d$ be a random variable whose distribution is described by the multidimensional probability density function (pdf) $q_X(\mathbf{x})$, and let F be the subdomain of the variables $\mathbf{x}$ leading to an event of interest (which can be seen as the failure of a system or, in this case, an impact with a celestial body). A performance function $g_X(\mathbf{x})$ is defined such that $g_X(\mathbf{x}) \leq 0$ if $\mathbf{x} \in F$ and $g_X(\mathbf{x}) > 0$ otherwise. Similarly, an indicator function$I_F(\mathbf{x})$ is defined such that $I_F(\mathbf{x}) = 1$ if $\mathbf{x} \in F$ and $I_F(\mathbf{x}) = 0$ otherwise.

The probability of the event F can be expressed as a multidimensional integral in the form

$$P(F) = P(\mathbf{x} \in F) = \int_F I_F(\mathbf{x})\ q_X(\mathbf{x})\ \mathrm{d}\mathbf{x} = E[I_F(\mathbf{x})] \tag{3.16}$$

where $\mathbf{x} = (x_1, ..., x_d)^T \in \mathbb{R}^d$ is the vector of the uncertain variables of the system, and $E[\cdot]$ is defined as the expected value operator. Eq. 3.16 shows that $I_F(\mathbf{x})$ is also a random variable [81] and that $P(F)$ can be interpreted as the expected value of $I_F(\mathbf{x})$.

The variance σ^2 of $I_F(\mathbf{x})$ is then defined as

$$\begin{aligned} \sigma^2[I_F(\mathbf{x})] &= \int_F [I_F(\mathbf{x}) - P(F)]^2\ q_X(\mathbf{x})\ \mathrm{d}\mathbf{x} \\ &= E[I_F^2(\mathbf{x})] - E[I_F(\mathbf{x})]^2 \\ &= E[I_F^2(\mathbf{x})] - P(F)^2 \end{aligned} \tag{3.17}$$

Since $I_F^2(\mathbf{x}) = I_F(\mathbf{x})\ \forall \mathbf{x} \in \mathbb{R}^d$ due to $I_F(\mathbf{x})$ being defined as a binary function, it

follows that

$$\begin{aligned}\sigma^2[I_F(\mathbf{x})] &= E[I_F^2(\mathbf{x})] - E[I_F(\mathbf{x})]^2 \\ &= E[I_F(\mathbf{x})] - E[I_F(\mathbf{x})]^2 \\ &= P(F) - P(F)^2 = P(F)\,(1 - P(F))\end{aligned} \tag{3.18}$$

For the standard MC, an estimator $\hat{P}(F)$ of the probability $P(F)$ as expressed in Eq. 3.16 is obtained by dividing the number of times that $I_F(\mathbf{x}_k) = 1,\ k = 1, ..., N$ by the total number of samples drawn N:

$$\hat{P}(F) = \frac{1}{N} \sum_{k=1}^{N} I_F(\mathbf{x}_k) \tag{3.19}$$

If standard MC is interpreted as a Point Sampling method, in comparison with the LS, $I_F(\mathbf{x})$ becomes the random variable that is sampled in order to estimate the probability of event F.

In the application of LS, a coordinate transformation from the physical space to the standard normal space $T_{X\theta} : \mathbf{x} \rightarrow \boldsymbol{\theta}$ brings as advantages the normalisation of the physical variables through the covariance matrix, and the possibility to express the multidimensional pdf as a product of d unit Gaussian standard distributions $\phi_j(\theta_j)$:

$$\Phi(\theta) = \prod_{j=1}^{d} \phi_j(\theta_j) \tag{3.20}$$

With reference to Fig. 3.1, in the d-dimensional standard normal space, the subdomain F is the subspace for which the samples $\boldsymbol{\theta} = (\theta_1, ..., \theta_d)^T$ satisfy a given property (e.g. an impact with a planet or a system failure). With the assumption that θ_1 points in the direction of the sampling vector $\boldsymbol{\alpha}$ (this can always be assured by a suitable rotation of the coordinate axes), the subdomain F can be also expressed as

$$F = \{\boldsymbol{\theta} \in \mathbb{R}^d : \theta_1 \in F_1(\theta_1, ..., \theta_d)\} \tag{3.21}$$

with $F_1 \in \mathbb{R}^{d-1}$, in this way the region F corresponds to the values of $\boldsymbol{\theta}$ such that the performance function $g_\theta(\boldsymbol{\theta})$ satisfies the relation $g_\theta(\boldsymbol{\theta}) = g_{\theta,-1}(\boldsymbol{\theta}_{-1}) - \theta_1 \geq 0$, where $\boldsymbol{\theta}_{-1} = (\theta_2, ..., \theta_d)^T$.

Considering this change of variables and the definition in Eq. 3.21, the integral in Eq. 3.16 can be rewritten as

$$P(F) = \int_d I_F(\boldsymbol{\theta}) \prod_{j=1}^{d} \phi_j(\theta_j)\ \mathrm{d}\boldsymbol{\theta} = E[I_F(\boldsymbol{\theta})] \tag{3.22}$$

and manipulated as follows:

$$\begin{aligned} P(F) &= \int_d I_F(\boldsymbol{\theta}) \prod_{j=1}^{d} \phi_j(\theta_j)\, \mathrm{d}\boldsymbol{\theta} \\ &= \int_{d-1} ... \int \left(\int I_F(\boldsymbol{\theta}_{-1})\, \phi_1(\theta_1)\, \mathrm{d}\theta_1 \right) \prod_{j=2}^{d} \phi_j(\theta_j)\, \mathrm{d}\boldsymbol{\theta}_{-1} \\ &= \int_{d-1} ... \int \Phi(F_1(\boldsymbol{\theta}_{-1})) \prod_{j=2}^{d} \phi_j(\theta_j)\, \mathrm{d}\boldsymbol{\theta}_{-1} \\ &= E_{\boldsymbol{\theta}_{-1}}[\Phi(F_1(\boldsymbol{\theta}_{-1}))] \end{aligned} \tag{3.23}$$

where $\Phi(A) = \int I_A(\mathbf{x})\phi(\mathbf{x})\mathrm{d}\mathbf{x}$ is the definition of the Gaussian measure of A, where A is the subset of the random variables $\mathbf{x}$ which lead to a given result (e.g. an impact).

In case of the standard MC, $\Phi(F_1(\boldsymbol{\theta}_{-1}))$ is a discrete random variable equal to $I_F(\boldsymbol{\theta})$; as a consequence:

$$Phi^2(F_1(\boldsymbol{\theta}_{-1})) = \Phi(F_1(\boldsymbol{\theta}_{-1}))\ \forall \boldsymbol{\theta}_{-1} \in \mathbb{R}^{d-1}$$

On the contrary, for the LS method $\Phi(F_1(\boldsymbol{\theta}_{-1}))$ is a continuous random variable where $F_1(\boldsymbol{\theta}^k_{-1}) = -\overline{c}^k$. This is clear from Fig. 3.1, where the sampling procedure is represented highlighting the boundary of the region corresponding to the event F. As a consequence:

$$0 \leq \Phi(F_1(\boldsymbol{\theta}_{-1})) \leq 1\ \forall \boldsymbol{\theta}_{-1} \in \mathbb{R}^{d-1}$$
$$0 \leq \Phi^2(F_1(\boldsymbol{\theta}_{-1})) \leq \Phi(F_1(\boldsymbol{\theta}_{-1}))\ \forall \boldsymbol{\theta}_{-1} \in \mathbb{R}^{d-1}$$

The consequence of these properties is visible when considering the definition of variance of an estimator for the two methods. An estimator $\hat{P}(F)$ of the probability $P(F)$ as expressed in Eq. 3.23 can be computed as

$$\hat{P}(F) = \frac{1}{N_T} \sum_{k=1}^{N_T} \Phi(F_1(\boldsymbol{\theta}^k_{-1})) \tag{3.24}$$

where $\boldsymbol{\theta}^k = 1, ..., N_T$ are independent and identically distributed samples in the standard normal coordinate space. Given the generic definition of variance for $P(F)$ following Eq. 3.23 as

$$\begin{aligned} &\sigma^2(P(F)) \\ &= \int [\Phi(F_1(\boldsymbol{\theta}_{-1})) - P(F)]^2\, \phi(\boldsymbol{\theta}_{-1})\, \mathrm{d}\boldsymbol{\theta}_{-1} \\ &= E_{\boldsymbol{\theta}_{-1}}[\Phi^2(F_1(\boldsymbol{\theta}_{-1}))] - E^2_{\boldsymbol{\theta}_{-1}}[\Phi(F_1(\boldsymbol{\theta}_{-1}))] \\ &= E_{\boldsymbol{\theta}_{-1}}[\Phi^2(F_1(\boldsymbol{\theta}_{-1}))] - P(F)^2 \end{aligned} \tag{3.25}$$

the variance of the estimator $\hat{P}(F)$ is defined as

$$\sigma^2(\hat{P}(F)) = \sigma^2(P(F))/N_T = \sigma^2[\Phi(F_1(\boldsymbol{\theta}_{-1}))]/N_T \tag{3.26}$$

meaning that the variance of the estimator directly depends on the variance of the random variable $\Phi(F_1(\boldsymbol{\theta}_{-1}))$:

$$\begin{aligned}&\sigma^2[\Phi(F_1(\boldsymbol{\theta}_{-1}))]\\&= E_{\boldsymbol{\theta}_{-1}}[\Phi^2(F_1(\boldsymbol{\theta}_{-1}))] - E^2_{\boldsymbol{\theta}_{-1}}[\Phi(F_1(\boldsymbol{\theta}_{-1}))]\end{aligned} \tag{3.27}$$

Consequently, since $0 \leq \Phi(F_1(\boldsymbol{\theta}_{-1})) \leq 1$ and $0 \leq \Phi^2(F_1(\boldsymbol{\theta}_{-1})) \leq \Phi(F_1(\boldsymbol{\theta}_{-1}))$ are always true $\forall \boldsymbol{\theta}_{-1} \in \mathbb{R}^{d-1}$, the previous relation can be extended as follows:

$$\begin{aligned}&\sigma^2[\Phi(F_1(\boldsymbol{\theta}_{-1}))]\\&= E_{\boldsymbol{\theta}_{-1}}[\Phi^2(F_1(\boldsymbol{\theta}_{-1}))] - E^2_{\boldsymbol{\theta}_{-1}}[\Phi(F_1(\boldsymbol{\theta}_{-1}))]\\&\leq E_{\boldsymbol{\theta}_{-1}}[\Phi(F_1(\boldsymbol{\theta}_{-1}))] - E^2_{\boldsymbol{\theta}_{-1}}[\Phi(F_1(\boldsymbol{\theta}_{-1}))]\\&= P(F)\,(1 - P(F)) = \sigma^2[I_F(\boldsymbol{\theta})]\end{aligned} \tag{3.28}$$

Since $P(F)\,(1 - P(F))$ is the definition of the variance of the standard MC as given in Eq. 3.18, one can conclude from Eq. 3.28 that the variance obtained by the LS method is always smaller than the one given by standard MC, or at least equal to it.

A coefficient of variation (c.o.v.) $\delta = \sqrt{\sigma^2(\hat{P}(F))}/P(F)$ can be defined as a measure of the efficiency of the sampling method, with lower values of δ meaning a higher efficiency of the method in converging to the exact value of the probability. Eq. 3.28 demonstrates that the c.o.v. of estimator in Eq. 3.26 as given by the LS method is always smaller than the one given by the standard MC, implying that the convergence rate of the LS is always faster than, or as fast as, that of the standard MC.

3.2.3 Extension of the theoretical formulation

As introduced in the previous section, here the theory behind the LS method is taken further, to obtain more insight about it and about which parameters affect the the accuracy the method provides. The analytical formulas showing that the accuracy of the LS is always equal or higher to the accuracy given by standard MC were manipulated as part of the research work on LS. From this work, a formula based on approximations was obtained, showing how the accuracy of LS depends from important parameters such as the shape of the impact region and the determination of the sampling direction. This formula will be demonstrated and discussed.

The analytical development presented here follows the notation used in the previous section and taken from [81].

While in the case of the standard MC Eq. 3.28 is easy to treat, since $E_{\boldsymbol{\theta}_{-1}}[\Phi^2(F_1(\boldsymbol{\theta}_{-1}))] = E_{\boldsymbol{\theta}_{-1}}[\Phi(F_1(\boldsymbol{\theta}_{-1}))]$, in the LS case $E_{\boldsymbol{\theta}_{-1}}[\Phi^2(F_1(\boldsymbol{\theta}_{-1}))]$ is a continuous variable, defined through the integral

$$E_{\boldsymbol{\theta}_{-1}}[\Phi^2(F_1(\boldsymbol{\theta}_{-1}))] = \int_{d-1} \ldots \int \Phi^2(F_1(\boldsymbol{\theta}_{-1})) \prod_{j=2}^{d} \phi_j(\theta_j)\, \mathrm{d}\boldsymbol{\theta}_{-1} \tag{3.29}$$

which cannot be easily manipulated analytically due to the presence of $\Phi^2(F_1(\boldsymbol{\theta}_{-1}))$. For this reason, it is chosen to express this term with an approximation.

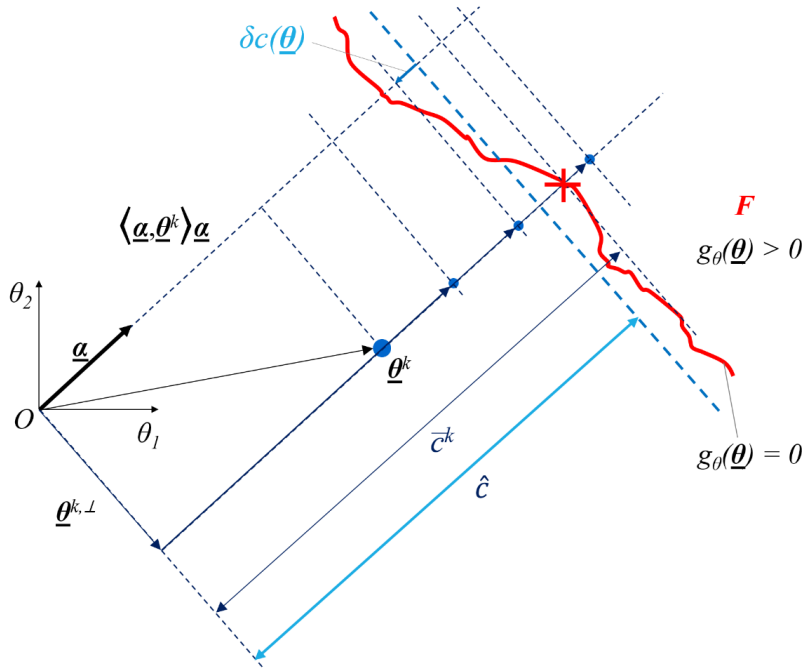

Figure 3.3: *Scheme representing the approximations used to express the variance of the LS method as a function of the probability estimate.*

The definition of $\Phi(F_1(\boldsymbol{\theta}_{-1}))$ given in Eq. 3.23 can be further expanded as

$$\begin{aligned}\Phi(F_1(\boldsymbol{\theta}_{-1})) &= \int_{-\infty}^{+\infty} I_F(\boldsymbol{\theta}_{-1})\ \phi_1(\theta_1)\ \mathrm{d}\theta_1 \\ &= \int_{\bar{c}(\boldsymbol{\theta}_{-1})}^{+\infty} \phi_1(\theta_1)\ \mathrm{d}\theta_1 = 1 - \Phi(\bar{c}(\boldsymbol{\theta}_{-1})) = \Phi(-\bar{c}(\boldsymbol{\theta}_{-1}))\end{aligned} \tag{3.30}$$

with $\bar{c}(\boldsymbol{\theta}_{-1})$ defined as the border of the region F displayed in Fig. 3.1 and Fig. 3.3 as a red line. $\bar{c}(\boldsymbol{\theta}_{-1})$ is then expanded as $\bar{c}(\boldsymbol{\theta}_{-1}) = \hat{c} + \delta c(\boldsymbol{\theta}_{-1})$, with the first term defined as an "average" value of $\bar{c}(\boldsymbol{\theta}_{-1})$ (represented as a dashed blue line in Fig. 3.3) such that $P(F) = E_{\boldsymbol{\theta}_{-1}}[\Phi(F_1(\boldsymbol{\theta}_{-1}))] = \Phi(F_1(\boldsymbol{\theta}_{-1})) = \Phi(\hat{c})$, and the second term as a variation with respect to this average value.

The hypothesis is made that $\delta c(\boldsymbol{\theta}_{-1})$ represents a small variation with respect to the average value $\hat{c}$, as in the case of a quasi rectilinear border of the region F orthogonal to the sampling direction $\boldsymbol{\alpha}$. Under this hypothesis, the integral in Eq. 3.30 can be rewritten as

$$\begin{aligned}&\Phi(F_1(\boldsymbol{\theta}_{-1})) \\ &= \int_{\bar{c}(\boldsymbol{\theta}_{-1})}^{+\infty} \phi_1(\theta_1)\ \mathrm{d}\theta_1 = \int_{\hat{c}+\delta c(\boldsymbol{\theta}_{-1})}^{+\infty} \phi_1(\theta_1)\ \mathrm{d}\theta_1 \\ &= \int_{\hat{c}}^{+\infty} \phi_1(\theta_1)\ \mathrm{d}\theta_1 - \int_{\hat{c}}^{\hat{c}+\delta c(\boldsymbol{\theta}_{-1})} \phi_1(\theta_1)\ \mathrm{d}\theta_1 \\ &\approx \Phi(\hat{c}) - \phi(\hat{c})\ \delta c(\boldsymbol{\theta}_{-1})\end{aligned} \tag{3.31}$$

resulting in

$$\begin{aligned}
&E_{\boldsymbol{\theta}_{-1}}[\Phi^2(F_1(\boldsymbol{\theta}_{-1}))] \\
&\approx E_{\boldsymbol{\theta}_{-1}}[(\Phi(\hat{c}) - \phi(\hat{c})\ \delta c(\boldsymbol{\theta}_{-1}))^2] \\
&= E_{\boldsymbol{\theta}_{-1}}[\Phi^2(\hat{c}) - 2\Phi(\hat{c})\ \phi(\hat{c})\ \delta c(\boldsymbol{\theta}_{-1}) + \phi^2(\hat{c})\ \delta c^2(\boldsymbol{\theta}_{-1})] \\
&= E_{\boldsymbol{\theta}_{-1}}[\Phi^2(\hat{c})] - E_{\boldsymbol{\theta}_{-1}}[2\Phi(\hat{c})\ \phi(\hat{c})\ \delta c(\boldsymbol{\theta}_{-1})] + E_{\boldsymbol{\theta}_{-1}}[\phi^2(\hat{c})\ \delta c^2(\boldsymbol{\theta}_{-1})] \\
&= P(F)^2 - P(F) \cdot 2\phi(\hat{c}) \cdot E_{\boldsymbol{\theta}_{-1}}[\delta c(\boldsymbol{\theta}_{-1})] + \phi^2(\hat{c}) \cdot E_{\boldsymbol{\theta}_{-1}}[\delta c^2(\boldsymbol{\theta}_{-1})]
\end{aligned} \tag{3.32}$$

Taking expression 3.32 into account, and defining in a compact way $\Delta c(\boldsymbol{\theta}_{-1}) = E_{\boldsymbol{\theta}_{-1}}[\delta c(\boldsymbol{\theta}_{-1})]$, the variance given by the LS in Equations 3.25 and 3.23 becomes

$$\begin{aligned}
&\sigma^2(P(F)) = \sigma^2[\Phi(F_1(\boldsymbol{\theta}_{-1}))] \\
&= E_{\boldsymbol{\theta}_{-1}}[\Phi^2(F_1(\boldsymbol{\theta}_{-1}))] - P(F)^2 \\
&\approx -P(F) \cdot 2\phi(\hat{c}) \cdot \Delta c(\boldsymbol{\theta}_{-1}) + \phi^2(\hat{c}) \cdot E_{\boldsymbol{\theta}_{-1}}[\delta c^2(\boldsymbol{\theta}_{-1})] \\
&\approx -P(F) \cdot 2\phi(\hat{c}) \cdot \Delta c(\boldsymbol{\theta}_{-1}) \\
&\leq P(F)\,(1 - P(F)) = \sigma^2[I_F(\boldsymbol{\theta})]
\end{aligned} \tag{3.33}$$

Highlighting the new terms in Eq. 3.33

$$\begin{aligned}
&\sigma^2(\Phi(F_1(\boldsymbol{\theta}_{-1}))) \approx -P(F) \cdot 2\phi(\hat{c}) \cdot \Delta c(\boldsymbol{\theta}_{-1}) \\
&\leq P(F)\,(1 - P(F)) = \sigma^2[I_F(\boldsymbol{\theta})]
\end{aligned} \tag{3.34}$$

this means that a new estimation for the worst covariance given by the LS method (nominally, from Eq. 3.28, equal to the one given by the standard MC) was obtained, which takes into account the probability level through the term $\phi(\hat{c})$, and the shape of the region F and the direction of sampling through the term $\Delta c(\boldsymbol{\theta}_{-1})$. When the approximation of small $\delta c(\boldsymbol{\theta}_{-1})$ is valid, meaning that the region F has a regular shape and is distributed across the initial uncertainty and the sampling direction is chosen properly so that it points toward it, and the probability level is low, the term $\phi^2(\hat{c}) \cdot E_{\boldsymbol{\theta}_{-1}}[\delta c^2(\boldsymbol{\theta}_{-1})]$ is also small, and we can say that the variance given by the LS is below a value $f(P(F), \Delta c(\boldsymbol{\theta}_{-1}))$ such that $\sigma^2(P(F))_{LS} \leq f(P(F), \Delta c(\boldsymbol{\theta}_{-1})) \leq \sigma^2(P(F))_{MC}$, thus increasing the convergence rate of LS with respect to standard MC. On the contrary, when the approximation does not hold (that is in cases with high probability levels, non-optimal sampling direction, or badly shaped impact regions), $f(P(F), \Delta c(\boldsymbol{\theta}_{-1}))$ grows toward the covariance level of the MC.

3.3 Extension to multi-event analysis

As will be presented in Section 3.4, LS can be more efficient (to reach the same accuracy) than the standard MC in estimating the impact probability for a single event, meaning for a close encounter with a specific body in a specific narrow time interval. However, analysing multiple close approaches over an extended period using the same sampling direction and the same number of samples can lead to less accurate results: as the sampling direction is computed according to one impact region, it would be "less optimal" for the other regions than any direction computed specifically for those cases.

This, in turn, increases the variance of the probability estimates corresponding to those impact regions, and thus reduce the accuracy of the final result.

For this reason, an algorithm to correct a first guess for the sampling direction based on a preliminary analysis. This algorithm will be used in the multi event analysis to ensure that each impact region is sampled according to an optimal direction.

3.3.1 Correction of the sampling direction

As pointed out in the development presented in section 3.2.3, the sampling direction is one of the key parameters determining the accuracy and efficiency of the Line Sampling method, where the ideal case is represented by the sampling direction being (almost) orthogonal to the boundary of the impact region.

While it is generally impossible to determine an optimal sampling direction a priori, Zio et al. [81] suggest a strategy to identify it as the one minimising the variance $\sigma^2(\hat{P}(F)_{N_T})$ of the probability estimator $\hat{P}(F)_{N_T}$. This strategy consists in an optimisation search having the variance $\sigma^2(\hat{P}(F)_{N_T})$ as the objective function to be minimised, requiring the iterative evaluation of hundreds or thousands of possible solutions $\boldsymbol{\alpha}_{guess}$ and $2N_T$ or $3N_T$ system model evaluations to be carried out to calculate the objective function $\sigma^2(\hat{P}(F)_{N_T})$ for each proposed solution. Therefore, the computational effort associated to this technique could be prohibitive with a system model code requiring hours or even minutes to run a single simulation.

The method that was implemented in SNAPPshot, instead, goes through a short preprocessing phase used to correct an initial guess for the sampling direction $\boldsymbol{\alpha}_{guess}$. This guess solution is obtained from the initial Markov Chain already described in Section 3.2.1, and is then used in a short line sampling analysis over a low number of samples to gain information about the general position and shape of the impact region; the solutions given by this preliminary sampling are used to approximate the impact region as a hyperplane according to a multilinear regression (assuming this approximation is valid), thus using the norm vector orthogonal to the hyperplane as new sampling direction.

The full algorithm represented in Fig. 3.4 follows the steps listed below:

1. The initial Markov Chain is performed and a guess for the sampling direction $\boldsymbol{\alpha}_{guess}$ is found

2. A short Line Sampling is performed using a few initial samples (drawn from the Markov Chain itself), obtaining the corresponding $\overline{c}^k$ values at the boundary of the impact region

3. The reference frame is rotated to an orthonormal base aligned with $\boldsymbol{\alpha}_{guess}$ (this in order to define the hyperplane during the regression more easily)

4. The $\overline{c}^k$ values are used to approximate the impact boundary of the impact region as a hyperplane, according to a multilinear regression scheme as $\overline{c}^k = b_1 + b_2\theta_2^{k,\perp} + b_3\theta_3^{k,\perp} + b_4\theta_4^{k,\perp} + ... = \left[\mathbf{1}\ \boldsymbol{\theta}^{k,\perp}\right] \cdot \mathbf{B}$, where $\mathbf{B} \in \mathbb{R}^d$ is the vector collecting the coefficients defining the d-dimensional hyperplane

5. The vector $\mathbf{B}$ orthogonal to the hyperplane is set as the new sampling direction

6. The main line sampling procedure is performed following the "corrected" direction.

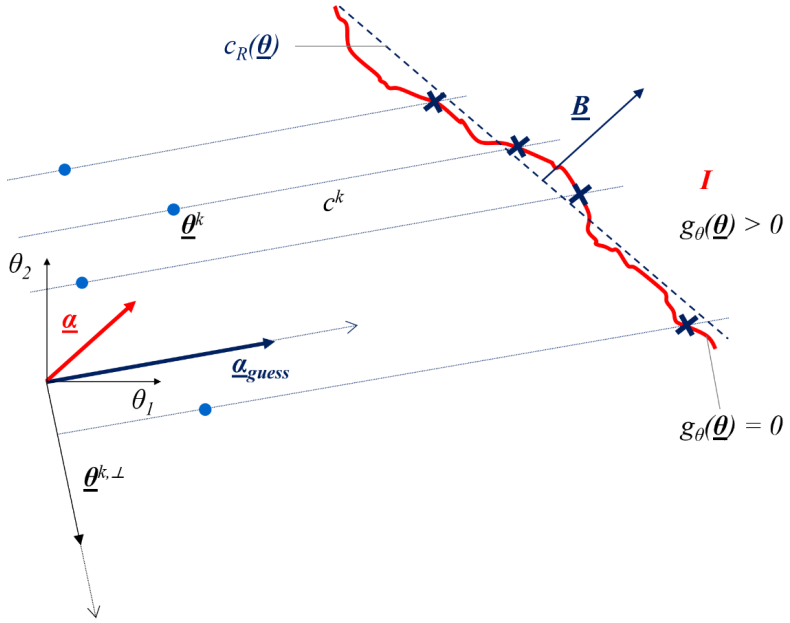

Figure 3.4: *Scheme representing the algorithm for the correction of the sampling direction using multilinear regression.*

The efficiency of this scheme relies on two main hypotheses: first, as already stated, that the impact region or its boundary can be approximated as a hyperplane; second, that the "corrected" sampling direction is "more optimal" than the initial one due to it being orthogonal to the boundary of the impact region, thus closer to the ideal case for the Line Sampling.

The application of this technique and its comparison with the line sampling using the standard procedure are shown in Section 3.4.

Definition of the orthonormal base

The orthonormal base used in the multilinear regression is generated according to the Gram-Schmidt orthogonalisation process [107] starting from the guess sampling direction, in order to obtain a base that is aligned with $\boldsymbol{\alpha}_{guess}$.

This algorithm constructs an orthonormal basis starting from a set of d linearly independent vectors $\mathbf{v}_i \in \mathbb{R}^d,\ i = 1, ..., d$ as $\mathbf{V} = [\mathbf{v}_1\ ...\ \mathbf{v}_d]$. Since an initial set is needed, it is set $\mathbf{v}_1 = \boldsymbol{\alpha}_{guess}$ in order to construct it starting from $\boldsymbol{\alpha}_{guess}$ only; the other vectors $\mathbf{v}_1, ..., \mathbf{v}_d$ of the initial set are generated as $\mathbf{v}_i = (\alpha_i, ..., \alpha_d, \alpha_1, ..., \alpha_{i-1}),\ i = 1, ..., d$ in order to avoid singularities.

The orthogonalisation algorithm proceeds as follows:

1. $\mathbf{u}_1 = \mathbf{v}_1 = \boldsymbol{\alpha}_{guess}$

2. $\mathbf{u}_i = \mathbf{v}_i - \sum_{j \leq i-1} \frac{\langle \mathbf{u}_j, \mathbf{v}_i \rangle}{\langle \mathbf{u}_j, \mathbf{u}_j \rangle} \mathbf{u}_j,\ i = 2, ..., d$

3. $\mathbf{y}_i = \frac{\mathbf{u}_i}{\|\mathbf{u}_i\|},\ i = 1, ..., d$

The operation $\langle \mathbf{u}, \mathbf{v} \rangle$ denotes the inner or scalar product between two vectors $\mathbf{u}, \mathbf{v} \in \mathbb{R}^d$, with $\frac{\langle \mathbf{u}, \mathbf{v} \rangle}{\langle \mathbf{u}, \mathbf{u} \rangle} \mathbf{u}$ being the projection of $\mathbf{v}$ onto $\mathbf{u}$. In this way, $\mathbf{Y} = [\mathbf{y}_1 ... \mathbf{y}_d]$ is defined as an orthonormal base, with $\mathbf{y}_1$ parallel to $\boldsymbol{\alpha}_{guess}$, making it possible to express the regression hyperplane in a more convenient way.

Algorithm for multilinear regression

Given a set of n dependent values $y_i,\ i = 1, ..., n$ and a set of n independent variables $\mathbf{x}_i = (x_{i1}, ..., x_{id})^T \in \mathbb{R}^d,\ i = 1, ..., n$, the linear regression model assumes that there exists a relationship $f(\mathbf{x}_i) = y_i \forall i = 1, ..., n$ which can be modelled linearly as

$$y_i = (b_0 + b_1 x_{i1} + b_2 x_{i2} + ... + b_d x_{id} + \varepsilon)_i = [1\ \mathbf{x}_i^T] \cdot \mathbf{B} + \boldsymbol{\varepsilon},\ i = 1, ..., n \tag{3.35}$$

with $\boldsymbol{\varepsilon} \in \mathbb{R}^d$ being an error variable representing the random noise due to the approximation.

Defining the following quantities

$$\mathbf{y} = \begin{pmatrix} y_1 \\ \vdots \\ y_n \end{pmatrix} \quad \mathbf{X} = \begin{bmatrix} 1 & \mathbf{x}_1^T \\ \vdots & \vdots \\ 1 & \mathbf{x}_n^T \end{bmatrix} \quad \mathbf{B} = \begin{pmatrix} b_0 \\ \vdots \\ b_d \end{pmatrix} \quad \boldsymbol{\varepsilon} = \begin{pmatrix} \varepsilon_1 \\ \vdots \\ \varepsilon_n \end{pmatrix}$$

the coefficients $\mathbf{B}$ are found by imposing the minimisation of the quadratic quantity

$$\sum_i \varepsilon_i^2 = \boldsymbol{\varepsilon}^T \boldsymbol{\varepsilon} = (\mathbf{y} - \mathbf{X}\mathbf{B})^T (\mathbf{y} - \mathbf{X}\mathbf{B}) \tag{3.36}$$

which gives as solution

$$\mathbf{B} = (\mathbf{X}^T \mathbf{X})^{-1} \mathbf{X}^T \mathbf{y} \tag{3.37}$$

The vector of coefficients $\mathbf{B}$ also contains the components of the defining vector orthogonal to the hyperplane. Thus, in the correction procedure described in Section 3.3.1, the new sampling direction $\boldsymbol{\alpha}$ is set parallel to the vector defined as $(b_1, ..., b_d, -1)^T$ in order to point toward the hyperplane approximating the boundary of the impact region.

3.3.2 Multi-event analysis

In order to maintain a high level of accuracy throughout the analysis, a repetitive process is presented, as schematised in Fig. 3.5. The proposed solution makes use of repeated Line Sampling procedures based on different sampling directions: these directions are identified according to close approach windows, that is the time intervals where close approaches with planets occur, which can be visualised in the example in Fig. 3.6, where each dot represents a fly-by (crossing of the sphere of influence) plotted according to the epoch and the distance, while the thin rectangles represent the time intervals used to look for impact regions; the colour identifies the order of sampling, starting from the intervals with the lowest distance. For each of these windows,

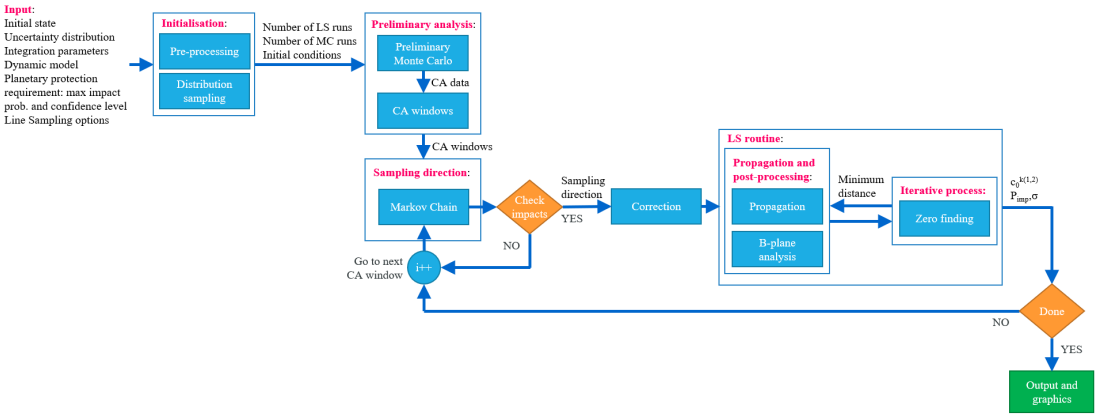

Figure 3.5: *Block scheme representing the algorithm implemented in SNAPPshot to perform the multi-event analysis with Line Sampling: the preliminary MC survey and identification of the CA windows, the Markov chain generation, the determination and correction of the sampling direction, and the estimation of the impact probability with line sampling.*

a Markov Chain is started, so that a sampling direction can be determined in case an impact region is present.

Particular attention should be given to the identification of the CA windows and their sampling in search of the impact regions. The correct determination of all possible CA windows is essential for the application of LS, as it allows to eventually identify all possible impact regions and explore them to provide an estimate of the impact probability as close to the real value as possible.

The full procedure, as it is described in the scheme in Fig. 3.5, follows the following steps:

1. A preliminary MC is performed, using a low number of initial samples, and every close approach occurring during the propagations (detected via the post-processing tools available in SNAPPshot) is stored in memory: this initial phase allows to obtain a first estimate of how many and where the impact regions might be;

2. The data about the fly-bys is analysed and the close approach (CA) window are identified and sorted according to the minimum distance (with priority given to the the window leading to the closest CA): this allows to focus on the impact regions corresponding to the most relevant impact events (if any);

3. A Markov Chain is started to search for an impact region inside the first close approach window: this allows to populate the impact region (if any) and determine a first guess for the sampling direction;

4. At the end of the Markov Chain

   (a) In case impacts were detected, A preliminary LS is performed using a first guess for the sampling direction, which is then corrected using the algorithm introduced in Section 3.3.1; this allows to obtain a new sampling direction

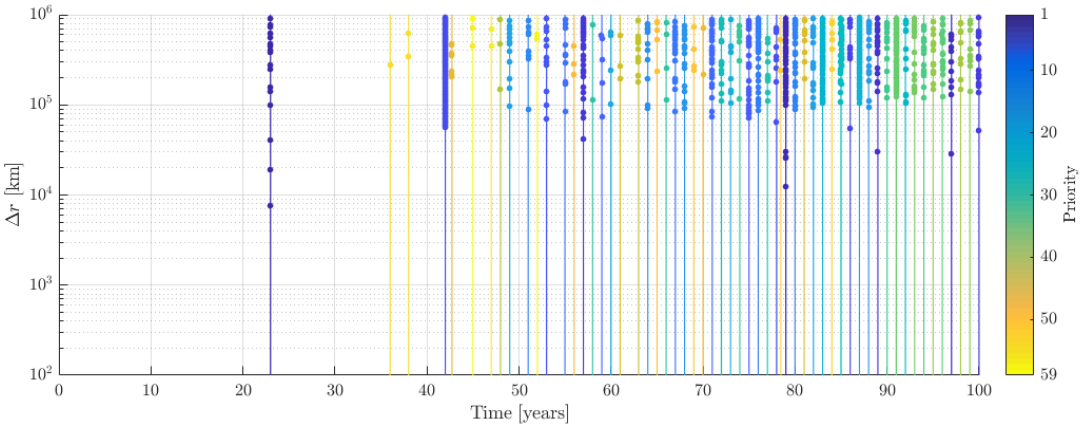

Figure 3.6: *Close approach window given by the preliminary MC analysis in the case of the post-Earth return trajectory of the Mars Sample Return mission. Each fly-by (crossing of the sphere of influence) is reported as a dot according to the epoch and the distance, and different close approach windows are reported as thin rectangles; the colour identifies the order of sampling, starting from the intervals with the lowest distance.*

that is ideally closer to the optimal case for LS, which in turns allows to improve its accuracy;

(b) A new set of random initial conditions is drawn from the distribution and a complete LS is performed as described in the previous sections to identify the impact region and compute the corresponding impact probability;

(c) In case no impacts were detected, the next CA window in the priority order is selected, and the procedure goes back to point 4 to start a new Markov chain;

5. After all CA windows have been analysed, the impact probability is given by the weighted sum of all the partial impact probabilities, as it was shown in Eq. 3.15 in Section 3.2.1.

Despite being computationally more complex and less memory efficient (due to the larger number of parameters involved and to the larger output size) than a single LS analysis, this method can ideally offer a complete overview of the impact regions inside the initial uncertainty distribution, providing additional information with respect to a normal planetary protection analysis, thus being able to be used directly in mission design.

Many parameters can affect the efficiency of this method in terms of number of propagations (compared with the standard MC) and its reliability in identifying correctly the impact regions (if any). In particular, the number of samples of preliminary Monte Carlo (determined by confidence level), the length of the Markov Chains, the number of sampling lines, the tolerances used in the iterative process to determine the intersections between each sampling line and the impact region were identified as key parameters in these regards. For each of them, a trade off is required: while higher

values would increase the accuracy of the determination of the impact regions and, consequently, of the probability estimate, the impact on the computational load may make the LS process less efficient than the standard MC; on the contrary, lower values would reduce substantially the number of orbital propagations needed to identify and sample the CA windows, but would not ensure the correct recognition of the impact regions. They are briefly discussed in the following paragraphs.

The number of samples in the preliminary MC phase affects both the correct identification of the CA windows (and, in turn, of the impact regions) and the computational load (since it requires extra propagations). In the test cases presented in Section 3.4, it is determined using the functionalities of SNAPPshot [5], which exploit the expression of the confidence interval by Wilson [51] to estimate in advance the number of MC samples needed to obtain a given value of probability with a given confidence level. Here this number is not directly used to compute a probability, but rather to obtain a coverage of the uncertainty domain aiming at identifying the as many CA windows as possible. Thus, the chosen values should depend on the value of the probability set by the planetary protection requirement: a scaling of a few orders of magnitude is adopted in this work, as a trade off between reliability and efficiency.

The length of the Markov chains used to explore each CA window is also a relevant parameter for both the accuracy and the efficiency of the method, as it allows to determine whether a CA window contains an impact region or not. While for large impact regions shorter chains may be enough to identify impacts inside a CA window, small impact regions may require longer chains, especially considering that more than one Markov chain sampling is performed. Also in this case the value should take as a reference the expected level of probability, or better the number of standard MC runs that would be required to verify that value of probability: as a trade off, $10^2 - 10^3$ chain elements should be chosen depending on the case.

The number of sampling lines defines the accuracy of the probability estimate for each impact region, and represents the largest contribution to the computational load, having multiple orbital propagations for each sampling line. Also in this case, the initial number is scaled of a few orders of magnitude with respect to the number of standard MC runs that would be needed to satisfy the same planetary protection requirement. The number so determined is then reduced or increased in case the desired accuracy is reached with fewer sampling lines during the analysis, or more of them are required.

Lastly, the choice of the the tolerances used to stop the iterations along each sampling line determines how accurately the boundaries of the impact region are identified, which in turn affects how accurately the conditional impact probabilities are estimated via the integrals in Eq. 3.12. This aspect is investigated in more detail in [100], where the effect of the accuracy of the iterative process on the probability estimate is quantified in a sensitivity analysis. In the algorithm described in Section 3.2.1 the iterations are stopped either by the residual value of the performance function or by the relative error between consecutive iterations: in both cases the tolerance is set to 10^{-3}, and a cap of 10 propagations per line is set as a trade off.

Algorithm for merging close approach intervals

Given n intervals $I^i = [t_1^i, t_2^i]$ with $t_1^i < t_2^i$ (corresponding, respectively, to the SOI entry and exit epochs of each close approach in the preliminary analysis), algorithm to

merge the close approach intervals proceeds as follow:

1. All intervals are sorted from earliest to latest starting epoch t_1^i (SOI entry) and put into a main stack
2. The interval on top of the main stack $I^1 = [t_1^1, t_2^1]$ is compared with the following one $I^2 = [t_1^2, t_2^2]$
   (a) If $t_1^1 \leq t_2^2 \; AND \; t_1^2 \leq t_2^1$, the two intervals I^1 and I^2 overlap, and thus are merged into a new $I = [t_1^1, t_2^2]$ which becomes the interval on top of the stack I^1
   (b) Else, I^1 is moved to an output stack and the comparison starts again from the interval on top of the main stack
3. The comparisons are carried out until the main stack is empty

The maximum complexity of this algorithm is of order $O(N \log N)$ (e.g., as used for sorting the minimum and maximum range values), with N being the number of recorded CAs. However, since the procedure is applied only once, it does not increase the computational load of the whole analysis in a relevant way.

3.4 Test case applications

The aim of this section is to apply the LS method and the algorithms developed to improve its performance to the selected test cases of planetary protection analysis (the launcher upper stages of the Solar Orbiter and of the Mars Sample Return missions). The results obtained from the LS simulations will be compared with the standard MC, in order to assess the performance of the proposed method in terms of accuracy and efficiency.

3.4.1 Choice of the performance parameters

The comparison between the standard MC and the proposed approach based on LS is performed by analysing the following parameters:

- the total number of orbital propagations N_{prop};
- for the LS only, the total number of sampling lines N_{lines};
- the impact probability estimate $\hat{P}(I)$;
- the sample standard deviation $\hat{\sigma}$ of $\hat{P}(I)$;

The overall number of propagations N_P is selected as a measure of the computational burden of the methods, while the standard deviation $\hat{\sigma}$ is instead used as indicator of the accuracy of the result, with lower values corresponding to lower variability [53, 80].

The total computational time is also reported and discussed among the results, however is not included the evaluations of the efficiency of the method due to the variability intrinsic to the choice of the machine and its workload.

3.4.2 Selection of test cases

Two test cases were selected to show how the proposed procedure works and its performance in identifying impact regions shaped differently with different probability levels:

1. The launcher upper stage of Solar Orbiter:
   - the data refers to an old option for a launch in October 2018, later discarded during the mission design (initial data in Table 3.1 taken from [5]);
   - the analysis focuses on the trajectory of the launcher upper stage following the injection into the interplanetary transfer orbit (aiming to a fly-by with Venus) and the separation from the spacecraft;
   - the planetary protection requirement applied in this case is the same used to protect Mars for a generic mission, with a probability level of 10^{-4}, as reported in Table 1.1 in Chapter 1.
2. The Mars Sample Return mission:
   - the analysis focuses on the return trajectory from Mars after performing an Earth-avoidance manoeuvre;
   - the uncertainty distribution is built assuming errors of 1 m on all position components and 5 m/s on all velocity components within a 3σ confidence level
   - the planetary protection requirement applied in this case is the same used to protect Earth for all sample return missions, with a probability level of 10^{-6}, as reported in Table 1.1 in Chapter 1.

For both cases, the initial state uncertainty is expressed as a 6x6 covariance matrix over the state only, and all initial data (epochs, states and uncertainties) is reported, and defined with respect to the EME2000 inertial reference frame. The propagations are carried out in normalised units (with reference length and time equal to 1 AU and 1 solar year, respectively) using the adaptive Dormand-Prince Runge-Kutta scheme of 8^{th} order (RK78), with absolute and relative tolerances both set to 10^{-12}.

For all the cases, the stopping tolerance of the iterative process for the line sampling is 10^{-3} with a maximum of 12 propagations per line. The dynamics equations of the RNBP presented in section 2.2 of Chapter 2 are integrated using the RK78 method with absolute and relative tolerances equal to 10^{-12}.

3.4.3 Planetary protection analysis

Launcher upper stage of Solar Orbiter

Table 3.1 reports the initial state, associated covariance matrix, and reference epoch for this mission case, which are the same ones reported in [5].

A preliminary MC simulation was performed to obtain information about the CA windows for the multi-event analysis. The number of runs was determined using the probability, confidence level, and maximum number of samples reported in Table 3.2:

Table 3.1: *Initial conditions for the simulations of the state inaccuracy of the launcher upper stage of Solar Orbiter: epoch, position, velocity, and the associated covariance matrix are reported, defined in the inertial EME2000 reference frame centred in the Sun.*

Epoch, MJD2000	**r**, km, **v**, km/s (EME2000 centred in the Sun)				
6868.6194	132048839.01817, 63140185.879734, 27571915.378760 -12.199001757542, 20.240166264928, 9.767449779832				
Covariance matrix (EME2000)					
x, km	y, km	z, km	v_x, km/s	v_y, km/s	v_z, km/s
$5.351{\cdot}10^{4}$	$5.409{\cdot}10^{4}$	$-2.562{\cdot}10^{4}$	$2.482{\cdot}10^{-1}$	$2.744{\cdot}10^{-1}$	$-1.205{\cdot}10^{-1}$
$5.409{\cdot}10^{4}$	$1.355{\cdot}10^{5}$	$4.508{\cdot}10^{3}$	$2.337{\cdot}10^{-1}$	$7.100{\cdot}10^{-1}$	$3.427{\cdot}10^{-2}$
$-2.562{\cdot}10^{4}$	$4.508{\cdot}10^{3}$	$1.728{\cdot}10^{5}$	$-1.370{\cdot}10^{-1}$	$5.015{\cdot}10^{-2}$	$8.333{\cdot}10^{-1}$
$2.482{\cdot}10^{-1}$	$2.337{\cdot}10^{-1}$	$-1.370{\cdot}10^{-1}$	$1.156{\cdot}10^{-6}$	$1.179{\cdot}10^{-6}$	$-6.485{\cdot}10^{-7}$
$2.744{\cdot}10^{-1}$	$7.100{\cdot}10^{-1}$	$5.015{\cdot}10^{-2}$	$1.179{\cdot}10^{-6}$	$3.724{\cdot}10^{-6}$	$3.078{\cdot}10^{-7}$
$-1.205{\cdot}10^{-1}$	$3.427{\cdot}10^{-2}$	$8.333{\cdot}10^{-1}$	$-6.485{\cdot}10^{-7}$	$3.078{\cdot}10^{-7}$	$4.019{\cdot}10^{-6}$

Table 3.2: *Input data and results of the preliminary MC for the multi-event analysis for the Solar Orbiter mission.*

Probability, CL	10^{-2}, 0.99
# samples	1000
# recorded CAs	660
# CA windows	108
# impact regions found	1

that value was obtained by scaling the probability set by the planetary protection requirement by two orders of magnitude. The table also shows the number of close approaches that were recorded and the number of CA windows that were identified via the merging algorithm introduced in Section 3.3.2, while Fig. 3.7 shows their distribution in time.

Fig. 3.7 shows the distribution in time of the CA windows found with the preliminary MC analysis, indicating each encounter with a planet as a dot according to its epoch and minimum distance from the encountered planet. The color scale indicates the sampling priority that is given to each CA window, starting from the one with the closest CAs. In particular, Fig. 3.8 shows a close-up of the CA window that was assigned the highest priority, which, in this case, is also the only CA window where an impact region was found via the sampling with a Markov Chain. This was an expected result, since, in this launch option, the upper stage injects the spacecraft into a trajectory aiming for a direct gravity assist with Venus in the first year of the mission [108].

In the case of the launcher upper stage of Solar Orbiter, the LS was applied both without and with the correction of the sampling direction. The solution without the correction is shown in Fig. 3.9 and 3.10, while the one where the correction was applied is shown in Fig. 3.11 and 3.12: in both cases, the figures show the Δv distribution as

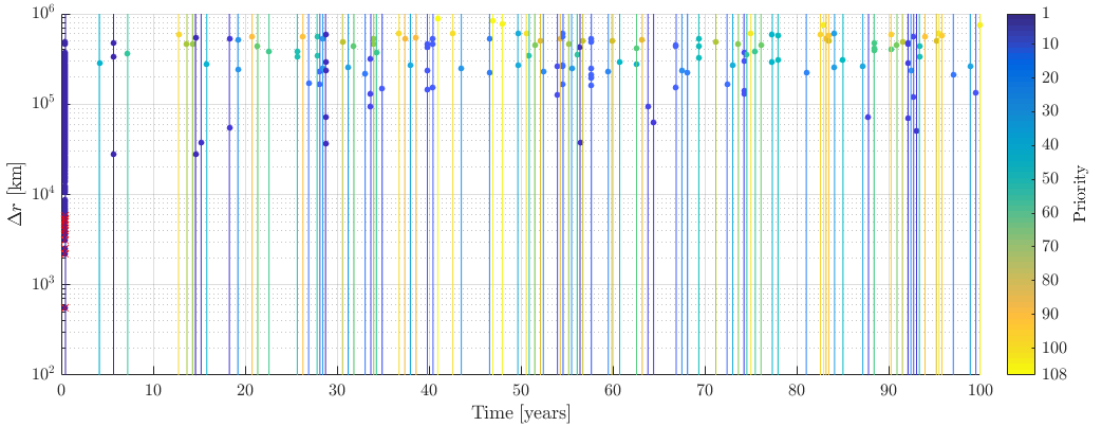

Figure 3.7: *Distribution in time of the close approach windows recorded during the preliminary Monte Carlo sampling of the uncertainty for the Solar Orbiter mission: dots represent close approaches reported with their minimum distance epoch and miss distance, while the thin rectangles represent the time intervals used to look for impact regions; the colour identifies the order of sampling, starting from the intervals with the lowest distance.*

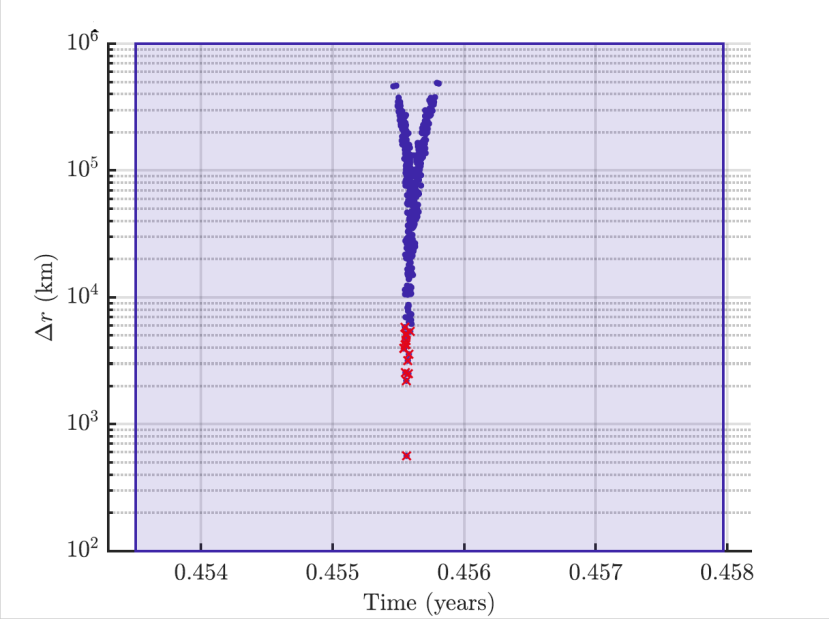

Figure 3.8: *Detail of the CA window identified as the first impact region for the Solar Orbiter mission.*

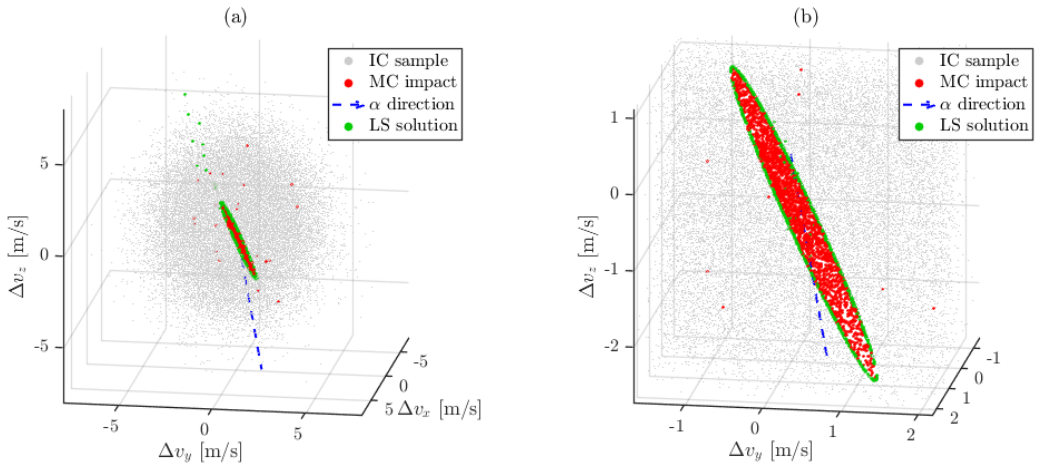

Figure 3.9: *Results of the application of the LS method to the case of the post-Earth return trajectory of the Solar Orbiter mission, without the correction of the sampling direction: (a) the whole initial dispersion (grey dots), impact region found with MC (red) and boundary found with LS (green); (b) the impact region in more detail.*

Table 3.3: *Results of the application of standard MC and LS (without correction and with correction of the sampling direction) for the case of the upper launcher stage of Solar Orbiter: number of propagations, number of sampling lines used by the LS, probability estimate and associated variance, and computational time.*

	N_{prop}	N_{lines}	$\hat{P}(I)$	$\hat{\sigma}$	CPU time (h)
MC	54114	-	$4.34{\cdot}10^{-2}$	$8.75{\cdot}10^{-4}$	0.80
LS (1st CA)	96164	10564	$4.00{\cdot}10^{-2}$	$8.75{\cdot}10^{-4}$	1.22
LS (1st CA), α correction	9437	1330	$4.02{\cdot}10^{-2}$	$8.75{\cdot}10^{-4}$	0.16

grey dots and the impact region as red (solution of the standard MC simulation) and green dots (boundary found via LS), and the convergence of the solutions given by standard MC and LS, in terms of estimated value of the impact probability and its associated standard deviation. Table 3.3 reports the numerical solutions in both cases, comparing them with the solution given by the standard MC simulation.

The results reported in Table 3.3 show the benefit given by the application of LS over standard MC, as the proposed method is able to reach the same variance of the probability estimate given by the standard MC using a much lower number of propagations when the sampling direction is chosen properly: not only the number of sampling lines is reduced by almost 8 times, but the number of necessary propagations is reduced as well by almost 6 times. In fact, a "less optimal" choice of the sampling direction affects not only the efficiency of the LS (with a higher number of sampling lines necessary to obtain the same accuracy), but also the accuracy of the iterative process itself, as in average 9 propagations per line are needed against the 7 propagations per line in case the sampling direction is corrected to be "more optimal". In both cases, the number of

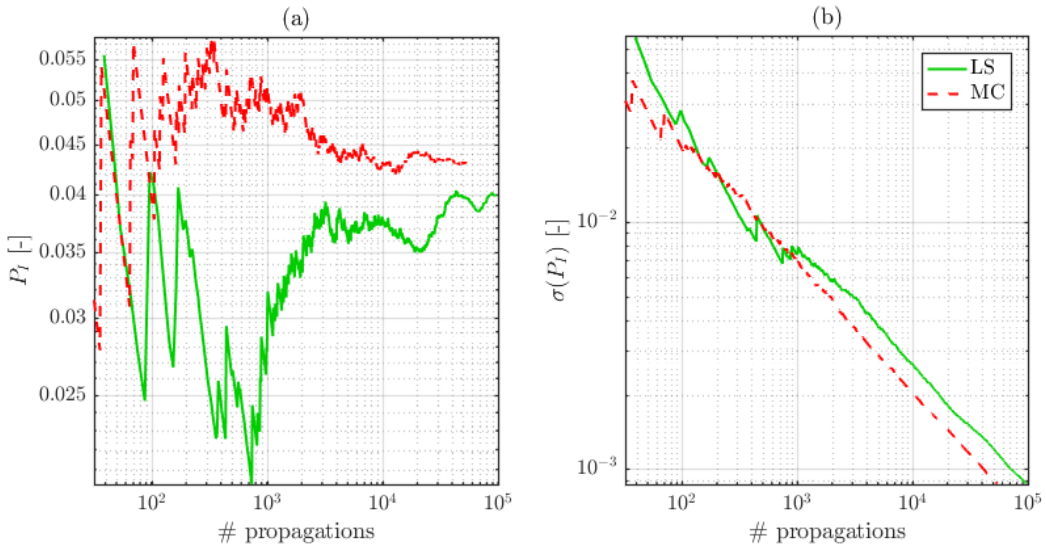

Figure 3.10: *Convergence of the solution given by LS compared with the convergence of standard MC in terms of impact probability in (a) and associated variance in (b) in the case of the Solar Orbiter mission, without the correction of the sampling direction.*

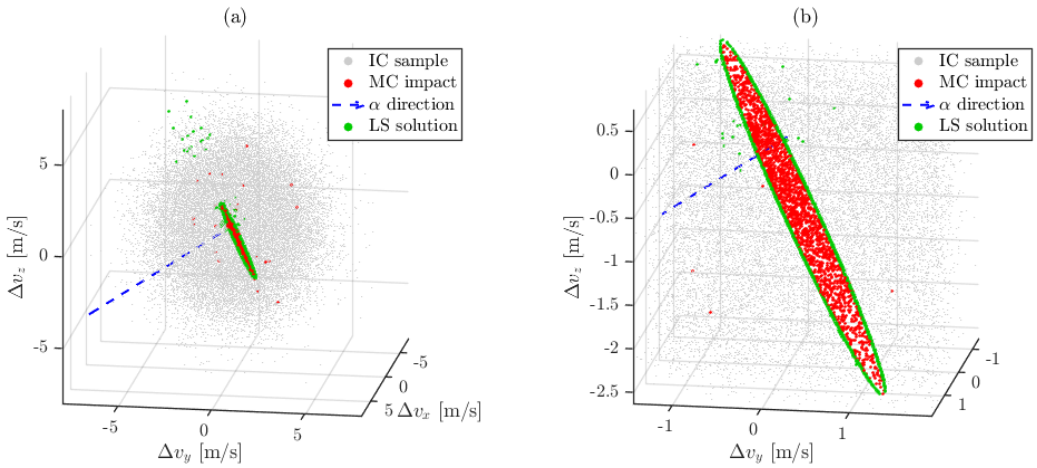

Figure 3.11: *Results of the application of the LS method to the case of the post-Earth return trajectory of the Solar Orbiter mission, after the correction of the sampling direction: (a) the whole initial dispersion (grey dots), impact region found with MC (red) and boundary found with LS (green); (b) the impact region in more detail.*

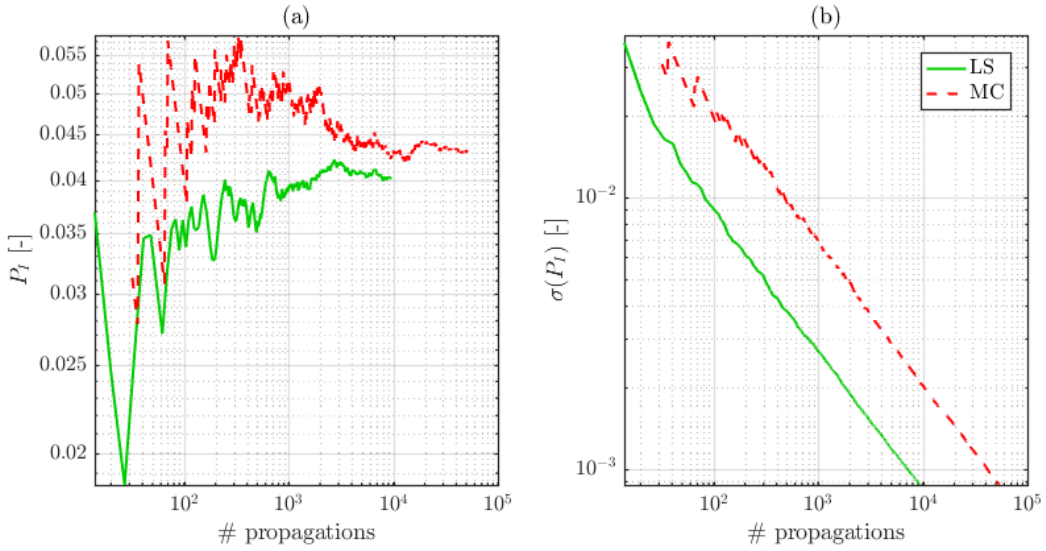

Figure 3.12: *Convergence of the solution given by LS compared with the convergence of standard MC in terms of impact probability in (a) and associated variance in (b) in the case of the Solar Orbiter mission, after the correction of the sampling direction.*

Table 3.4: *Numerical performance of LS with correction of the sampling direction compared to standard MC in the case of the launcher upper stage of Solar Orbiter.*

		# propagations	CPU time (h)
LS	Preliminary MC	1000	0.02
	Markov Chains	20800	0.35
	LS phases	9437	0.16
	Total	31237	0.53
MC	Total	54114	0.80

lines is initially determined based on the value of the probability set by the planetary protection requirement, and it is then increased to reach the same accuracy given by the standard MC in the non corrected case, or reduced when that accuracy is reached in the corrected case.

The differences in the values of the estimated impact probability are due both to the determination of the sampling direction, as already pointed out, and to the accuracy of the iterative process used to identify the boundary of the impact region. This also confirms the theoretical considerations made in Sections 3.2.2 and 3.2.3 about the importance of a proper determination of the sampling direction for a good accuracy of the LS solution.

It must be pointed out that the difference between the probability values estimated by the two methods is due to LS identifying only the main impact region, as seen in Fig. 3.9 and 3.11, and ignoring the isolated impacts found by standard MC. These may belong to extremely thin impact regions, which may be captured by LS with different values of simulation parameters (e.g. number of preliminary MC runs, length of Markov Chains), or may be outliers, which would require a different approach to be sampled. However, since the impact probability associated with the main impact region contributes the most to the overall estimation, the values computed via MC and LS do not differ substantially.

Table 3.4, instead, shows the computational load given by the whole multi-event procedure compared with the one given by the standard MC, for the analysis with the correction of the sampling direction, highlighting the various phases of the LS-based procedure, which is split into:

- preliminary MC, used to identify the CA windows;
- Markov Chains, one per CA window;
- LS phases, that is those phases where the impact regions found using the Markov chains (if any) are sampled using lines.

In this case, a maximum limit of 200 samples per Markov chain was set following the considerations made in Section 3.3.2. It is clear that the Markov Chains are the most demanding phases with 66% of the total computational load of LS, since each CA window is sampled to search for an impact region, while, as expected, the preliminary MC phase does not increase significantly the computational time.

Mars Sample Return mission

Table 3.5 reports the initial state, associated covariance matrix, and reference epoch for this mission case: the uncertainty was arbitrarily set to 1 m in position and 5 m/s in velocity, uniformly over all the components.

A preliminary MC simulation was performed to obtain information about the CA windows for the multi-event analysis. The number of runs was determined using the probability, confidence level, and maximum number of samples reported in Table 3.6: that value was obtained by scaling the probability set by the planetary protection requirement by three orders of magnitude. The table also shows the number of close approaches that were recorded and the number of CA windows that were identified, while Fig. 3.13 shows their distribution in time.

Table 3.5: *Initial conditions for the simulations of the spacecraft state inaccuracy for the Mars Sample Return mission: epoch, position, velocity, and the associated covariance matrix are reported, defined in the inertial EME2000 reference frame centred in the Sun.*

Epoch, MJD2000	**r**, km, **v**, km/s (EME2000 centred in the Sun)				
11601.8193	145474529.75119, 33739755.347356, -532320.51350861 -9.2557070719419, 30.974849145494, -3.5619719210297				
Covariance matrix (EME2000)					
x, km	y, km	z, km	v_x, km/s	v_y, km/s	v_z, km/s
$1.111{\cdot}10^{-7}$	0.0	0.0	0.0	0.0	0.0
0.0	$1.111{\cdot}10^{-7}$	0.0	0.0	0.0	0.0
0.0	0.0	$1.111{\cdot}10^{-7}$	0.0	0.0	0.0
0.0	0.0	0.0	$2.778{\cdot}10^{-6}$	0.0	0.0
0.0	0.0	0.0	0.0	$2.778{\cdot}10^{-6}$	0.0
0.0	0.0	0.0	0.0	0.0	$2.778{\cdot}10^{-6}$

Table 3.6: *Input data and results of the preliminary MC for the multi-event analysis for the Mars Sample Return mission.*

Probability, CL	10^{-4}, 0.99
# samples	10000
# recorded CAs	8754
# CA windows	59
# impact regions found	1

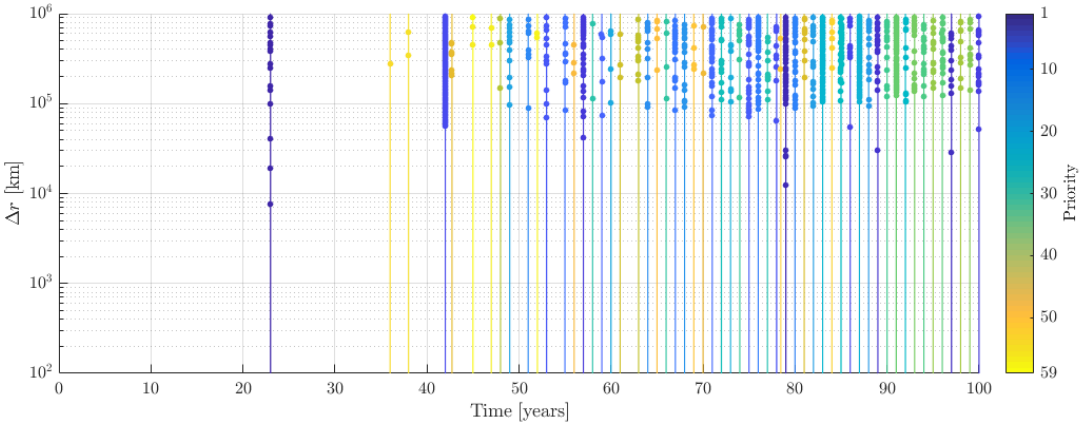

Figure 3.13: *Distribution in time of the close approach windows recorded during the preliminary Monte Carlo sampling of the uncertainty for the Mars Sample Return mission: dots represent close approaches reported with their minimum distance epoch and miss distance, while the thin rectangles represent the time intervals used to look for impact regions; the colour identifies the order of sampling, starting from the intervals with the lowest distance.*

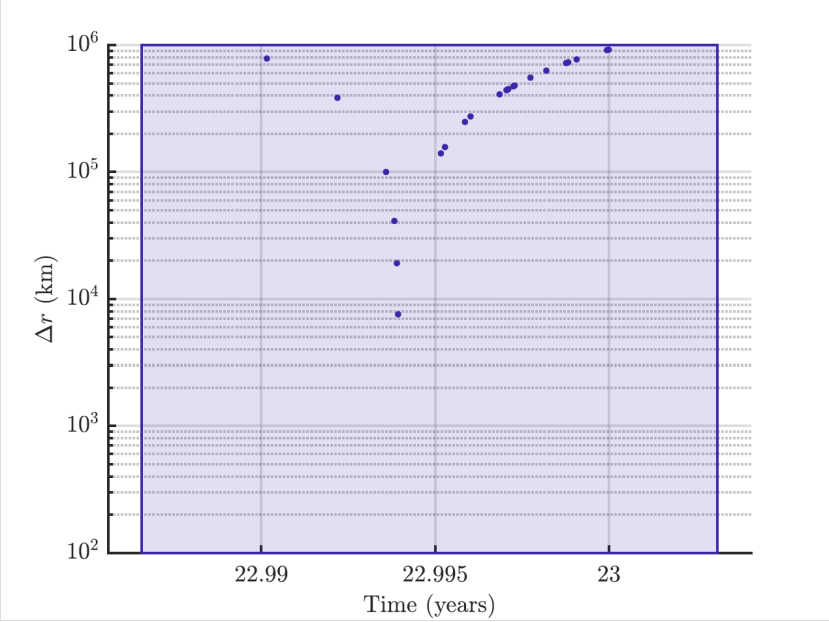

Figure 3.14: *Detail of the CA window identified as the first impact region for the Mars Sample Return mission.*

Table 3.7: *Results of the application of standard MC and LS (with correction of the sampling direction) for the case of the Mars Sample Return mission: number of propagations, number of sampling lines used by the LS, probability estimate and associated variance, and computational time.*

	N_{prop}	N_{lines}	$\hat{P}(I)$	$\hat{\sigma}$	CPU time (h)
MC	10^6	-	$4.70{\cdot}10^{-5}$	$6.85{\cdot}10^{-4}$	31.22
LS (1st CA), α correction	4879	729	$3.98{\cdot}10^{-5}$	$8.60{\cdot}10^{-9}$	0.15

Fig. 3.13 shows the distribution in time of the CA windows found with the preliminary MC analysis. In particular, Fig. 3.14 shows a close-up of the CA window that was assigned the highest priority, which, in this case, is also the only CA window where an impact region was found via the sampling with a Markov Chain, corresponding to an encounter window with Earth after 23 years from the beginning of the propagation period.

In the case of the Mars Sample Return mission, the LS was applied only with the correction of the sampling direction. In Fig. 3.15 the solution is shown in terms of the Δv distribution as grey dots and the impact region as red (solution of the standard MC simulation) and green dots (boundary found via LS), while in Fig. 3.16 as the convergence of the solutions given by standard MC and LS. Table 3.7 reports the numerical solutions by LS comparing it with the solution given by the standard MC simulation.

Also in this case, the benefit of using LS is visible, as both the number of prop-

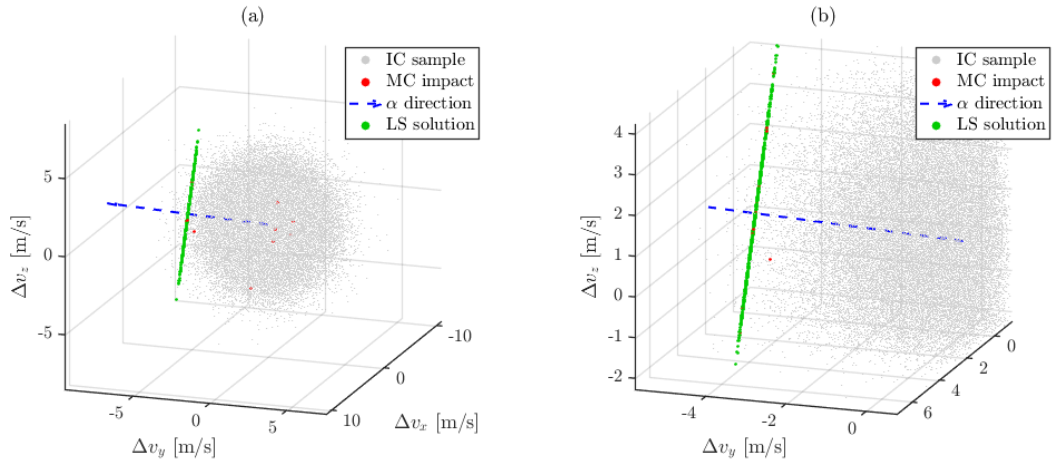

Figure 3.15: *Results of the application of the LS method to the case of the post-Earth return trajectory of the Mars Sample Return mission: (a) the whole initial dispersion (grey dots), impact region found with MC (red) and boundary found with LS (green); (b) the impact region in more detail.*

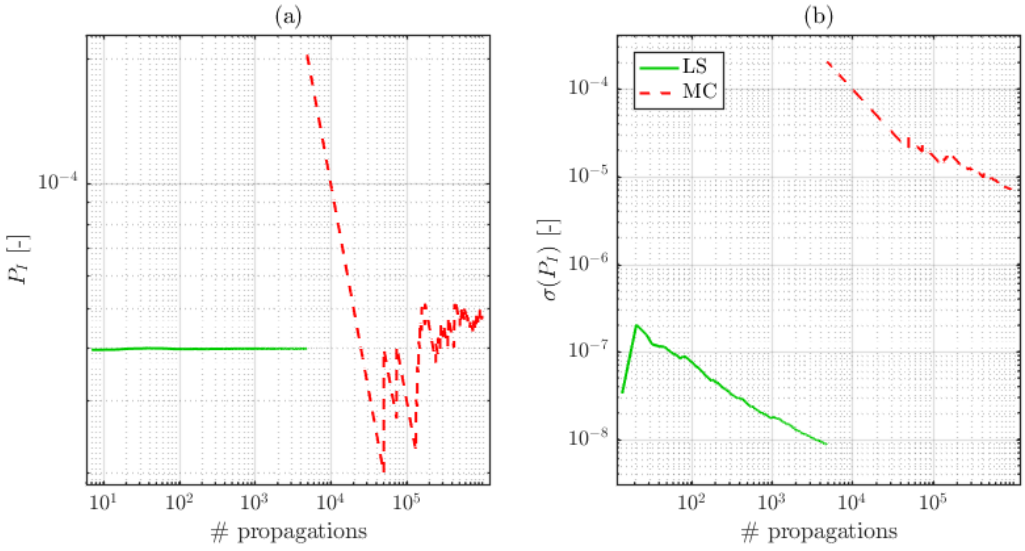

Figure 3.16: *Convergence of the solution given by LS compared with the convergence of standard MC in terms of impact probability in (a) and associated variance in (b) in the case of the Mars Sample Return mission.*

Table 3.8: *Numerical performance of LS compared to standard MC in the case of the Mars Sample Return mission.*

		# propagations	CPU time
LS	Preliminary MC	10000	0.31
	Markov Chains	59000	1.84
	LS phases	4879	0.15
	Total	73879	2.31
MC	Total	10^6	31.22

agations and the variance of the probability are reduced by orders of magnitude with respect to the standard MC in identifying the main impact region. In particular, this test case is very close to the optimal case of the application of LS: not only the probability value to be estimated is very low, but also the impact region has a planar shape extended across the uncertainty distribution, and the sampling direction is almost orthogonal to it thanks to the application of the correction algorithm (these observations follow the ones already done in [109]).

Again, it must be pointed out that the difference between the probability values estimated by the two methods is due to LS identifying only the main impact region, as seen in Fig. 3.15, and ignoring the the isolated impacts found by standard MC. These may belong to extremely thin impact regions, which may be captured by LS with different values of simulation parameters ((e.g. number of preliminary MC runs, length of Markov Chains), or may be outliers: in the first case, a proper choice of those parameters (following criteria already discussed in Section 3.3.2) would allow a correct identification with a limited increase in computational cost; in the second case, a different approach would be required to sample them. Since the impact probability associated with the main impact region contributes the most to the overall estimation, the values computed via MC and LS do not differ substantially. However, in such cases the LS approach might underestimate the value of the overall probability: thus, performing more than one analysis would allow to account for the variable effect of the different parameters involved in the algorithm.

Also in this case, the computational efficiency of the whole multi-event analysis is compared with the standard MC simulation, through the data reported in Table 3.8, highlighting the various phases of the LS-based procedure as defined in the previous test case. In this case, a maximum limit of 1000 samples per Markov chain was set following the considerations made in Section 3.3.2. Again, the Markov Chains sampling of each CA window is the most demanding phase, with almost 80% of the total computational load of LS. However, both in this case and in the previous one, the complete LS-based procedure reduces the computational time with respect to the MC analysis.

3.4.4 Comparison with Subset Simulation

The comparison between the LS and SS methods was done in collaboration with the Ph.D. candidate Matteo Losacco: the dynamical model for the simulations was implemented by the author of this thesis, along with the simulations using the LS, while the

simulations using SS were run by Matteo Losacco. The results of this joint work are reported in [59] and [100]. This section summarises the main considerations presented in those articles.

Both techniques sample the initial uncertainty region in different ways, with the result of either providing a more accurate estimation of the impact probability or reducing the number of samples required during the simulation with respect to standard MC techniques. LS probes the impact region of the uncertainty domain by using lines instead of points and estimates the impact probability as one-dimensional integrals along such lines: these integrals are evaluated analytically (see Section 3.2.1), resulting in a more accurate solution). Meanwhile, SS computes the impact probability as the product of larger conditional probabilities, by progressively identifying intermediate conditional levels moving towards the impact event: this reduces the overall number of samples required for the estimation [101–103].

The performance of the two methods were compared against standard MC in different test cases regarding single NEO impacts with Earth, one of which is reported here to provide a brief overview of their efficiency. The case under exam is the fly-by of asteroid 99942 Apophis with Earth in 2036, according to the initial conditions reported in [100], with an expected impact probability of $3.00 \cdot 10^{-5}$. Fig. 3.17 shows the initial distribution in the uncertainty space (δa,δl) in equinoctial parameters (where a is the semi-major axis of the orbit and l is the mean longitude [92]), highlighting the impact regions found according to the three methods, while Table 3.9 report the results of the numerical simulations in terms of number of orbital propagations N_P, estimated impact probability $\hat{P}(I)$, and the associated standard deviation $\hat{\sigma}(P(I))$. The results were obtained in one case using a number of samples granting the same accuracy level of standard MC (σ^{MC}), and in another case by performing the same number of propagations of the standard MC (N_P^{MC}).

The performance comparison in Table 3.9 confirms the benefits provided by both LS and SS over the standard MC, as both outperform the standard method in terms of both achieved accuracy and computational cost. More in detail, the same accuracy level of the standard MC simulation can be obtained by both LS and SS with a number of propagations that is one order of magnitude lower, or, alternatively, LS and SS achieve a higher accuracy level with the same number of samples adopted for the standard MC. This is true in particular for this case due to the very low probability value to be estimated, as both LS and MS are more efficient for low probability levels [80, 81].

In addition, the relative performance of LS against SS can be assessed here: while SS is very efficient in providing reliable impact probability results for relatively low number of samples, LS definitely provides the most accurate results as the number of initial samples (and thus of sampling lines) increases. This is the main reason behind the focus on LS for the doctoral research, as planetary protection analysis requires the verification of the impact probability values with generally strict confidence levels, thus making the greater accuracy of LS more suitable for this kind of problem with respect to SS.

Finally, further analysis in [100] has shown that the performance of each method can suffer from particular choices of the parameters characterising their implementation, either affecting the accuracy of the probability estimate or the computational load.

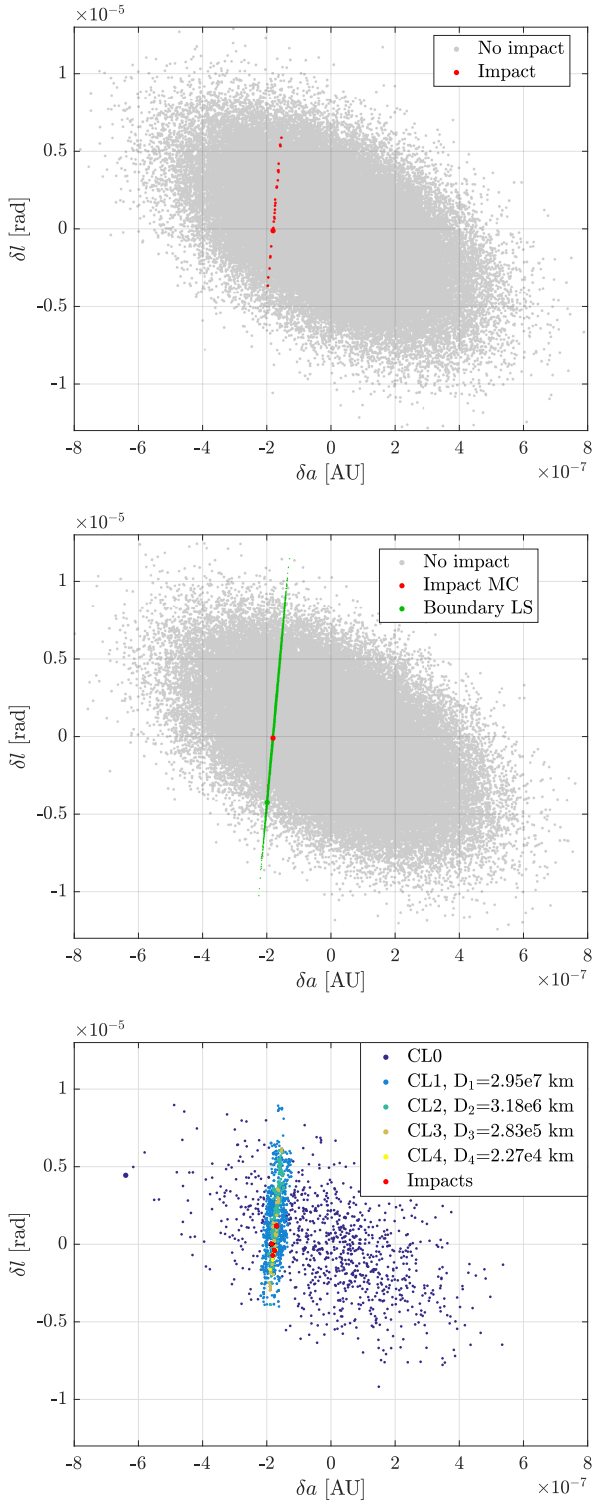

Figure 3.17: *Samples dispersion in the initial uncertainty space (δa,δl) for the case of asteroid 99942 Apophis: initial conditions leading to impact obtained via standard MC (top), boundaries of the subdomain identified via LS (middle), samples per conditional level obtained with SS (bottom).*

Table 3.9: *Performance comparison between standard MC, LS and SS when applied to the case of asteroid 99942 Apophis.*

	N_P	$\hat{P}(I)$	$\hat{\sigma}(P(I))$
MC	10^6	$3.00{\cdot}10^{-5}$	$5.48{\cdot}10^{-6}$
LS (σ^{MC})	2511	$3.19{\cdot}10^{-5}$	$5.48{\cdot}10^{-7}$
LS (N_P^{MC})	10^6	$3.10{\cdot}10^{-5}$	$2.56{\cdot}10^{-8}$
SS (σ^{MC})	6900	$3.27{\cdot}10^{-5}$	$5.30{\cdot}10^{-6}$
SS (N_P^{MC})	$1.01{\cdot}10^6$	$3.25{\cdot}10^{-5}$	$4.58{\cdot}10^{-7}$

3.5 Summary

This chapter focused on the improvement of the uncertainty sampling techniques currently used in planetary protection analysis. Under the premise of high computational cost for estimating low impact probabilities using standard Monte Carlo simulation methods, the Line Sampling method was presented as an alternative aimed to reducing the computational load of the statistical analysis by sampling the initial uncertainty distribution in a more efficient way.

The performance of LS was analysed in comparison with standard MC both numerically, by applying both methods to different mission cases, and analytically, by developing an approximated formula which highlights how the accuracy of LS depends on the geometry of the impact regions found within the initial uncertainty domain. The results presented in the previous sections showed that LS is able to identify the impact regions and to estimate the impact probability with a higher precision with respect to the standard MC, reaching a lower variance of the solution for the same number of orbital propagations, or a higher efficiency, using fewer propagations to reach the same accuracy. The results also showed cases in which the application of the LS is not favourable, as confirmed by the theoretical developments, thus providing a direction for the future improvement of the method.

Moreover, while the early phases of the doctoral research focused on the use of LS for single events, the method was later improved by extending it to cases where multiple impacts with planets are possible over long periods of time, as the majority of cases in planetary protection analysis fall in this category, by developing and implementing in SNAPPshot a new algorithm making use of a correction of an initial guess for the sampling direction with the aim of getting closer to the ideal case, and of repeated LS phases to analyse multiple events.

Various aspects of this approach were discussed from the numerical and implementation point of view. In particular, several parameters were identified as having a relevant influence on both the accuracy and the computational efficiency of the LS analysis, involved in the various phases of of the procedure: the preliminary MC analysis used to gather information about the possible impact regions; the building of the Markov chains used to identify the possible impact regions; the sampling of the impact regions using lines, and the estimation of the impact probability. A discussion about their ef-

fects on the performance of LS and possible criteria to choose their values was made, while some numerical values were shown when presenting the numerical application of the proposed approach.

CHAPTER 4

Uncertainty propagation methods

4.1 Introduction and novelties

Accurate uncertainty propagation in orbital dynamics can be carried out in different ways. The simplest method that is commonly adopted is Monte Carlo simulations, which sample an uncertainty distribution (representative of the errors over the measurement of the state of a spacecraft or debris at a given time) into several initial conditions, then propagate them to study the evolution of the initial uncertainty or to estimate the probability of an event via statistical processing [61]. Due to their great adaptability to complex problems and simplicity to implement in simulation environments, MC-based methods are particularly suited to be applied to orbital propagation, where the non-linearity of the n-body dynamics hinder the long-term precision of other techniques based on linearised or other simplified models. However, one major flaw of MC methods is the high number of orbital propagations that are required to provide adequate accuracy.

As already introduced in Section 1.3.3 of Chapter 1, planetary protection analysis is a phase of the design of a space mission aiming to verify that the probability of impacts between spacecraft and launcher stages is below a given threshold. Since this kind of analysis has a direct impact on the design of the mission, studying the evolution of the initial uncertainty is desirable to obtain more information about the long-term effects it has on the trajectory of the objects under study. Generally, the initial estimation of the uncertainty over the state of these objects is obtained through measurements, analysis of the flight telemetry (in case of a functioning spacecraft), and prior knowledge about the design parameters (e.g. the area-to-mass ratio), but in can increase when other factors are considered, such as errors in the execution of manoeuvres.

Given the nature of this problem, planetary protection analysis may have to con-

sider large uncertainties, especially in cases where random events occur or when flight data from the spacecraft is not available. These uncertainties, when representing the error over the knowledge of the orbital state, are often represented by a covariance matrix. This makes techniques for covariance propagation, especially GMM, a more suited choice with respect to other techniques, which may fail to correctly represent its transformation during the propagation due to the non-linear orbital dynamics. For this reason, techniques to split the uncertainty distribution in smaller ones to maintain the accuracy during the propagation exist, and are applicable to GMM methods.

These methods are more commonly used for studying the motion of space debris, and for conjunction analysis and collision risk assessment for Earth orbiting satellites [69, 110]. On the contrary, this thesis applies the GMM to study the interplanetary propagation of an uncertainty distribution described by a covariance matrix, and to estimate the impact probability with celestial bodies for planetary protection analysis. For this reason, GMM represents a novel approach to this field, whose challenges derive from long term propagation in the n-body environment, with the possibility of close approaches with celestial bodies strongly perturbing the trajectory.

In this chapter, GMM is proposed as a way to study the evolution of the covariance matrix describing the state uncertainty of a spacecraft or launcher stage. In particular, the adopted propagation technique makes use of the unscented transformation to propagate each Gaussian component forward in time, and of techniques to split it further adaptively to preserve the accuracy of the approximation. In the first part of the chapter, the theory behind GMM and the splitting of Gaussian distributions will be presented, along with the explanation of the propagation and adaptation techniques. An approach to estimate the probability of impacts with celestial bodies during the propagation is also shown. In the second part, the techniques will be applied to an example test case for planetary protection, presenting the arising problems and the possible solutions.

4.2 Theory

As already introduced in Chapter 1, the evolution in time of an uncertainty distribution is described by a partial differential equation known as the Fokker-Plank Equation (FPE) [60]. Given the pdf $p(\mathbf{x}, t)$ of a continuous random variable $\mathbf{x} \in R^n$, the FPE has the form

$$\begin{aligned}\frac{\partial p(\mathbf{x},t)}{\partial t} = &- \sum_{i=1}^{n} \frac{\partial}{\partial x_i}[\mathbf{f}(\mathbf{x},t)p(\mathbf{x},t)] \\ &+ \frac{1}{2}\sum_{i=1}^{n}\sum_{j=1}^{n} \frac{\partial^2}{\partial x_i \partial x_j}\{[\mathbf{g}(\mathbf{x},t)\mathbf{Q}(t)\mathbf{g}^T(\mathbf{x},t)]p(\mathbf{x},t)\}\end{aligned} \tag{4.1}$$

Equation 4.1 is applied to the stochastic dynamical system described as

$$\dot{\mathbf{x}} = \mathbf{f}(\mathbf{x},t) + \mathbf{g}(\mathbf{x},t)\eta(t) \tag{4.2}$$

where $\mathbf{f}(\mathbf{x},t)$ represents the equations of motion with initial conditions $\mathbf{x}(t_0) = \mathbf{x}_0$, $\eta(t)$ is a stochastic forcing term representing modelling errors modelled as a Gaussian white noise with the specified correlation function $\mathbf{Q}(t) \in R^{n\times n}$, and $\mathbf{g}(\mathbf{x},t)$ is a multiplicative function defining the coupling of the system to $\eta(t)$.

Since in the work presented in this thesis, uncertainties over the dynamical model are not considered, the second part of the FPE disappear, thus simplifying the description of the time evolution of a pdf. Despite this, solving the FPE remains a difficult task, due to the high dimensionality of the problem and the highly non-linear behaviour of the perturbed orbital dynamics equations. For this reason, alternative methods to solve the problem are adopted. In particular, in the applications presented here, the uncertainty over the state of a spacecraft or launcher stage is represented through a covariance matrix, making the use of techniques based on a Gaussian description of the problem, such as GMM, more suited to address the problems faced here.

For completeness, this section also presents the definitions of the mean and covariance of a pdf. These quantities, together with the higher order moments (which are not treated here) describe the shape of the pdf, respectively its average value and how the distribution is spread around the mean. The two definitions for the pdf $p(\mathbf{x}, t)$ of a continuous random variable $\mathbf{x} \in R^n$ are [61]

$$\begin{aligned} \mathbf{m}(t) &= E[\mathbf{x}(t)] = \int \mathbf{x} p(\mathbf{x}, t) d\mathbf{x} \\ \mathbf{P}(t) &= E[(\mathbf{x} - \mathbf{m})(\mathbf{x} - \mathbf{m})^T] = \int (\mathbf{x} - \mathbf{m})(\mathbf{x} - \mathbf{m})^T p(\mathbf{x}, t) d\mathbf{x} \end{aligned} \tag{4.3}$$

respectively for the mean $\mathbf{m}$ and the covariance $\mathbf{P}$, where $E[\cdot]$ represents the expected value operator. The time derivatives are also reported:

$$\begin{aligned} \dot{\mathbf{m}}(t) &= E[\dot{\mathbf{x}}(t)] = E[\mathbf{f}(\mathbf{x}, t)] \\ \dot{\mathbf{P}}(t) &= E[\dot{\mathbf{x}}\mathbf{x}^T + \mathbf{x}\dot{\mathbf{x}}^T] - \dot{\mathbf{m}}\mathbf{m}^T + \mathbf{m}\dot{\mathbf{m}}^T \end{aligned} \tag{4.4}$$

4.3 Gaussian Mixture Models

The underlying concept of GMM is the approximation of a generic pdf with a weighted sum of Gaussian pdfs [68]. Given a Gaussian random variable $\mathbf{x} \in R^n$, with mean $\mathbf{m} \in R^n$ and covariance matrix $\mathbf{P} \in R^{n \times n}$, the pdf is written as

$$\mathcal{N}(\mathbf{x}; \mathbf{m}, \mathbf{P}) = \frac{1}{\det(2\pi\mathbf{P})}^{1/2} \exp\left\{ -\frac{1}{2}(\mathbf{x} - \mathbf{m})^T \mathbf{P}^{-1} (\mathbf{x} - \mathbf{m}) \right\} \tag{4.5}$$

where $\det(\cdot)$ represents the matrix determinant.

A GMM representation of a generic pdf $p(\mathbf{x})$ is given by

$$p(\mathbf{x}) = \sum_{i=1}^{L} \alpha_i \mathcal{N}(\mathbf{x}; \mathbf{m}_i, \mathbf{P}_i) \tag{4.6}$$

where L represents the number of Gaussian components, α_i, $\mathbf{m}_i$, and $\mathbf{P}_i$ are the weights, mean, and covariance associated with each component. The weights are computed to be a convex combination (that is, a linear combination where all coefficients must be non-negative and sum to 1) to preserve the properties of a pdf:

$$\alpha_i \geq 0, i = 1, ..., L \quad \text{and} \quad \sum_{i=1}^{L} \alpha_i = 1 \tag{4.7}$$

The GMM approximation converges to the original pdf as the number of Gaussian components increases to infinity [111].

4.3.1 Splitting a Gaussian distribution

At the beginning of the propagation and during it, GMM components are split in order to reduce the effects induced by the non-linear dynamics with the consequences of making the Gaussian description of the uncertainty less accurate. Each component is replaced by one or several smaller ones, according to a scheme that is subject to constraints aiming to preserve the accuracy of the approximation and the properties of the starting pdf. While the propagation of the mean and the covariance of the distribution follows the rules presented in the next section, most algorithms focus on the determination of the initial weights of the GMM components.

Different algorithms are already available in the literature to determine the initial values of the weights used to split a distribution into a sum of weighted Gaussian components. Vishwajeet and Singla proposed a method to obtain the weights, means, and covariances of the splitting components based on the conservation of weight, mean, and covariance, and by distributing them according to the sigma-points of the original Gaussian distribution [112]. Horwood et al. proposed a splitting method by solving a constrained L_2 optimisation problem [113] to obtain the coefficients.

The method adopted here is the one presented by DeMars et al. [68] also based on a constrained L_2 optimisation problem. In this case, the GMM is constrained to be homoscedastic, meaning that all the components have the same variance, in order to reduce the complexity of the optimisation problem. The goal of the process is the minimisation of the distance between the original distribution $p(x)$ and the approximating one $\tilde{p}(x)$, which is defined as in Eq. 4.6:

$$\tilde{p}(x) = \sum_{i=1}^{L} \tilde{\alpha}_i \mathcal{N}(x; \tilde{m}_i, \tilde{\sigma}_i^2) \tag{4.8}$$

where $x \in R$ is a univariate random variable. The cost function to be optimised has the form

$$J = L_2 + \lambda \tilde{\sigma}^2, \text{with} \sum_{i=1}^{L} \tilde{\alpha}_i = 1 \tag{4.9}$$

where λ is a weight for the minimisation of $\tilde{\sigma}$ and L_2 is defined as

$$L_2 = \frac{1}{2}\|p(x) - \tilde{p}(x)\|^2 = \int_S [p(x) - \tilde{p}(x)]^2 \mathrm{d}x \tag{4.10}$$

The splitting is first applied to a univariate Gaussian distribution, then is extended to multivariate ones using an eigenvalue decomposition: starting from a GMM component with weight α, mean $\mathbf{m}$, and covariance matrix $\mathbf{P}$, the spectral factorisation of the latter is given by $\mathbf{P} = \mathbf{V}\mathbf{\Lambda}\mathbf{V}^T$, where $\mathbf{\Lambda} = \text{diag}\{\lambda_1, ..., \lambda_n\}$ is the diagonal matrix of eigenvalues and $\mathbf{V}$ is the matrix whose columns are the eigenvectors of $\mathbf{P}$. The

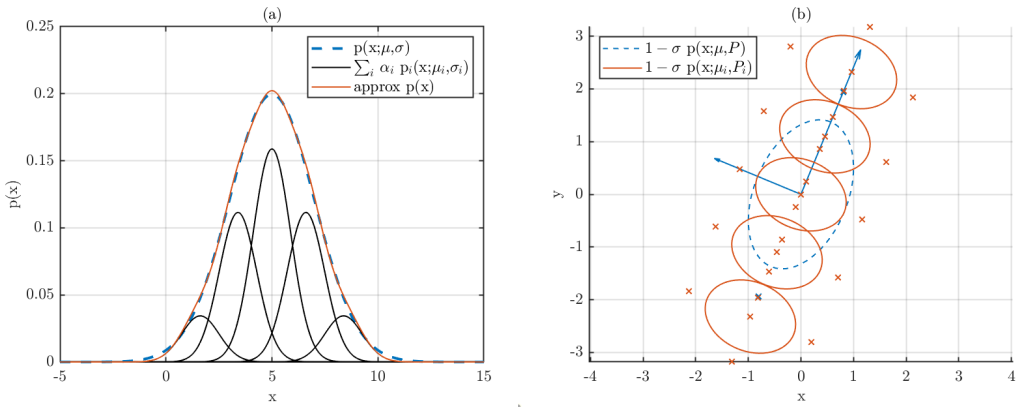

Figure 4.1: *Example of five-component split for a univariate (a) and a bivariate (b) distribution. The bivariate case shows the 1-σ ellipses of the original pdf in blue (with the arrows indicating the principal axes) and of the GMM components in red, while the crosses represent the sigma-points of the distributions.*

multivariate splitting is the defined as

$$\begin{aligned} \alpha_i &= \tilde{\alpha}_i \alpha \\ \mathbf{m}_i &= \mathbf{m} + \sqrt{\lambda_k}\tilde{m}_i \mathbf{v}_k \\ \mathbf{P}_i &= \mathbf{V}\mathbf{\Lambda}_i\mathbf{V}^T \end{aligned} \tag{4.11}$$

where $\mathbf{v}_k$ is the k^{th} eigenvector of $\mathbf{P}$, used as splitting direction, and

$$\mathbf{\Lambda}_i = \text{diag}\{\lambda_1, ..., \tilde{\sigma}^2\lambda_k, ..., \lambda_n\}$$

is the eigenvalues set of the new i^{th} GMM component. The process is applied iteratively to split a GMM component along multiple eigenvectors. Choosing the eigenvector associated with the largest eigenvalue as the splitting direction represents a splitting along the direction with the highest uncertainty.

An alternative definition uses the square root matrix $\mathbf{S}$ of $\mathbf{P}$ defined by $\mathbf{P} = \mathbf{S}\mathbf{S}^T$: in this case the sigma points are not aligned with the principal axes of the covariance matrix.

Several splitting libraries (collections of coefficients for the weight, mean, and covariance of each Gaussian component) based on this criterion are already available in the literature, e.g. the ones provided by Vittaldev and Russel [69] or by DeMars et al. [68], which were obtained by applying the procedure here described to the unit Gaussian distribution $\mathcal{N}(x; 0, 1)$. Fig. 4.1 show the application of the five-component splitting library from [68] to the unit Gaussian distribution, for a univariate (a) and a bivariate (b) distribution, in which the 1-σ ellipses are plotted in blue for the original pdf (with the arrows indicating the principal axes) and in red for the GMM components, while the crosses represent the sigma-points of the distributions (as defined in the next section).

4.3.2 Propagation via Unscented Transformation

The Unscented Transformation is an uncertainty propagation method which approximates the evolution of a probability distribution in time by non-linearly integrating forward a set of weighted samples derived from the sigma points of the distribution. These points are deterministically chosen to capture the moments of the initial distribution, meaning that the set has the same mean and covariance of the original distribution. Several definition of the sigma-point set exist in the available literature, depending on the choice of the number of points and on the definition of the weights. In this work, the symmetric set of $2n$ sigma points is used [62].

With the same notation used in [68], applying the spectral factorisation (or the square root matrix) of the covariance matrix already defined in the previous section, each sigma point $\boldsymbol{\chi}_{i,j}$ of the i^{th} GMM component is given by

$$\begin{aligned} \boldsymbol{\chi}_{i,j} &= \mathbf{m}_i + \sqrt{n}\sqrt{\lambda_j}\mathbf{v}_j \\ \boldsymbol{\chi}_{i,j+n} &= \mathbf{m}_i - \sqrt{n}\sqrt{\lambda_j}\mathbf{v}_j \quad j = 1, ..., n \end{aligned} \tag{4.12}$$

The corresponding weight associated with each sigma points is, in the case of the symmetric set, $w_i = 1/2n$. As the sigma points are defined in order to have the same mean and covariance of the initial distribution, it can be verified that

$$\begin{aligned} \mathbf{m}_i &= \sum_{j=1}^{2n} w_i \boldsymbol{\chi}_{i,j} \\ \mathbf{P}_i &= \sum_{j=1}^{2n} w_i (\boldsymbol{\chi}_{i,j} - \mathbf{m}_i)(\boldsymbol{\chi}_{i,j} - \mathbf{m}_i)^T \end{aligned} \tag{4.13}$$

At this point, the propagation of the GMM is carried out by numerically integrating the dynamics forward in time each sigma point set for all Gaussian components. Starting from time t_{s-1} with initial conditions $\boldsymbol{\chi}_{i,j}(t_{s-1}) = \boldsymbol{\chi}_{i,j,s-1}$ and $\alpha_i(t_{s-1}) = \alpha_{i,s}$, the equations are written in the form

$$\begin{aligned} \dot{\alpha}_i(t) &= 0 \\ \dot{\boldsymbol{\chi}}_{i,j}(t) &= \mathbf{f}(\boldsymbol{\chi}_{i,j}(y), t), \quad j = 1, ..., 2n \end{aligned} \tag{4.14}$$

The weights associated with each GMM component are held constant throughout the integration, since they are not updated according to a differential equation, but by stopping the propagation when growing non-linear effects are detected and then split. The adaptive procedure is explained in the following section.

The UT method integrates the sigma points according to the actual dynamics of the problem, thus accounting for all non-linear effects: this allows a more accurate description of the evolution of uncertainty distribution during the propagation, but still under the hypothesis that the Gaussian description is valid. On the contrary, linearised methods, such as those based on the Extended Kalman filter (EKF) cannot capture the evolution of the uncertainty as accurately when long propagation times or strongly non-linear dynamics (due to fast perturbations or close approaches with planets) are

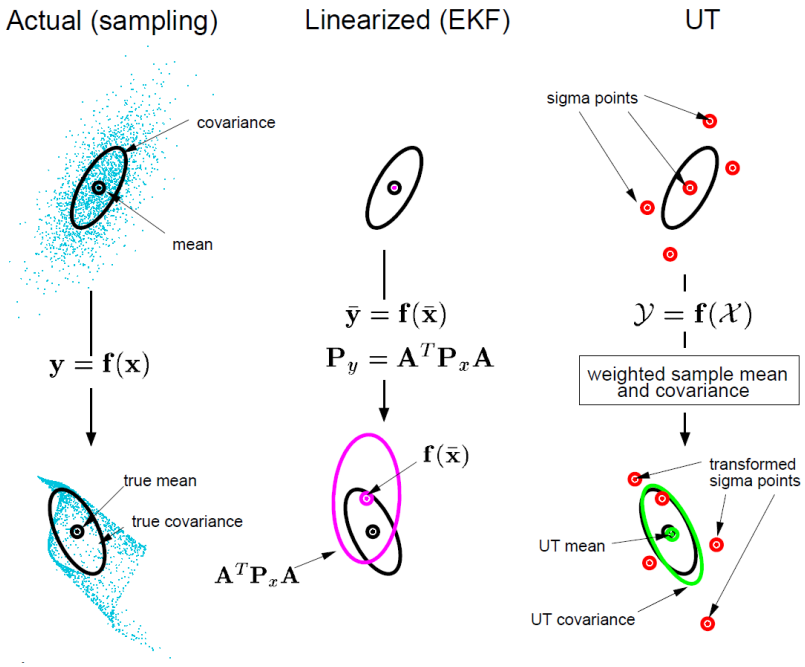

Figure 4.2: *Example of the UT for mean and covariance propagation. a) actual, b) first-order linearisation (EKF), c) UT. Image taken from [1].*

involved. Being conceptually simpler, however, they have a lower computational burden on the simulation with respect to non-linear models. This is well summarised in Fig. 4.2, which shows schematically the working principles of the fully non-linear UT and of a linearised model, comparing them with a MC sampling representing the actual transformation of the initial distribution.

In the EKF-based technique, the dynamical system is approximated via a local linearisation for each GMM component. In this way, the linearised equations describing the evolution of the weights, the mean, and the covariance of each components can be defined, by doing the derivative of the ones reported in Eq. 4.4:

$$\begin{aligned} \dot{\alpha}_i(t) &= 0 \\ \dot{\mathbf{m}}_i(t) &= \mathbf{f}(\mathbf{m}_i(t), t) \\ \dot{\mathbf{P}}_i(t) &= \mathbf{F}(\mathbf{m}_i(t), t)\mathbf{P}_i(t) + \mathbf{P}_i(t)\mathbf{F}^T(\mathbf{m}_i(t), t), \quad j = 1, ..., 2n \end{aligned} \tag{4.15}$$

where $\mathbf{F}(\mathbf{m}, t)$ represents the Jacobian of the equations of motion, defined as

$$\mathbf{F}(\mathbf{m}, t) = \left.\frac{\partial \mathbf{f}(\mathbf{x}(t), t)}{\partial \mathbf{x}(t)}\right|_{\mathbf{x}(t)=\mathbf{m}(t)}$$

4.3.3 Adaptive splitting

As already mentioned in the previous section, the adaptation of the weights during the propagation is not done continuously by integrating a differential equation, but by splitting the GMM component being propagated when non-linear effects distort the

distribution to the point that is cannot be considered Gaussian any more. The criterion to decide when a GMM component should be split evaluates at each time step of the propagation an estimator parameter, which measures the non-linear effects acting on the component and affecting the accuracy of its approximation as a Gaussian distribution.

Different approaches are proposed in the literature. Vishwajeet and Singla make use of the Kolmogorov equation error feedback to select the component to be split [112], considering the contributions of each GMM component to the error until one of them grows over a certain threshold. A different approach considers the variation of the differential entropy of each Gaussian component over the course of the propagation [68]. This latter approach was adopted in this work ans is summarised in this section.

Differential entropy is a measure of the average amount of information content associated with a randomly distributed variable [114,115]. For a given pdf $p(\mathbf{x})$ is defined as

$$H(\mathbf{x}) = -\int_S p(\mathbf{x}) \log p(\mathbf{x}) \mathrm{d}\mathbf{x} = E[-\log p(\mathbf{x})] \tag{4.16}$$

For a Gaussian distribution with covariance matrix $\mathbf{P}$, the differential entropy takes the form

$$H(\mathbf{x}) = \frac{1}{2} \log \det(2\pi e \mathbf{P}) \tag{4.17}$$

where $\det(\cdot)$ represents the matrix determinant.

From these definitions, the time derivative of the differential entropy for a Gaussian distribution can be expressed as

$$\dot{H}(\mathbf{x}) = \frac{1}{2} \mathrm{trace}\{\mathbf{P}^{-1}\dot{\mathbf{P}}\} = \mathrm{trace}\{\mathbf{F}(\mathbf{m}, t)\} \tag{4.18}$$

considering the expression for the time derivative of $\mathbf{P}$ in Eq. 4.15 where the Jacobian matrix $\mathbf{F}(\mathbf{m}, t)$ of the dynamics is highlighted. In particular, if a dynamical system has the property that $\mathrm{trace}\{\mathbf{F}(\mathbf{m}, t)\} = 0$, then the differential entropy is constant, being $\dot{H}(\mathbf{x}) = 0$.

The criterion proposed by DeMars et al. integrates Eq. 4.18 alongside the equations of motion, using H as an additional state variable. This equation is decoupled from the rest, allowing a simple evaluation of $\dot{H}(\mathbf{x})$ at each time step of the propagation. The criterion monitors the difference between two values: the value of the linearised differential entropy, obtained by numerically integrating Eq. 4.18, and the value of the non-linear estimation give by integrating Eq. 4.17. This difference is selected as an indicator of how accurately a GMM component can be described using a Gaussian definition: this difference grows during the propagation, meaning that the GMM component gradually becomes non-Gaussian. Whenever its value grows beyond a given control threshold for a GMM component, the propagation is stopped and a split is performed to mitigate the non-linear effects impacting the component. This control threshold is defined as a fraction of the value of the differential entropy for the initial distribution:

$$|H^{lin}(\mathbf{x}) - H^{nonlin}(\mathbf{x})| \geq \varepsilon |H_0| \tag{4.19}$$

with $\varepsilon < 1$ being set as the tolerance used to determine when a split is necessary during the propagation.

4.4 Application

This section presents a numerical example of the application of GMM to the propagation of an uncertainty distribution over an initial state for the estimation of impact probability with a planet. The selected test case is the launcher upper stage of the Solar Orbiter mission. The initial conditions are the same reported in Table 3.1 of Chapter 3.

In this test case, the analysis focuses exclusively on propagating the initial state uncertainty of the launcher stage until the first close encounter with Venus, six months after the initial epoch, and on giving an estimation of the probability of impact with the planet. This choice was done due to problems arisen during the propagation of the GMM: the number of Gaussian components exploded early in the integration, even for relatively large values of the control tolerance used to determine when a component should be split. This anomalous performance makes the GMM approach less efficient than a standard MC simulation.

In the simulation, the probability of impact was estimated by stopping the propagation of a GMM component at the moment of the closest approach with Venus, by then sampling a number of states from each component, and then evaluating the distance of each particle from the surface of the planet. This approach does not require any additional propagation, since the states are generated at the moment of the close approach, but only scalar evaluations.

Table 4.1: *Results of the application of GMM for the case of the upper launcher stage of Solar Orbiter: number of propagations, probability estimate, and computational time. The GMM simulation was performed for different values of the splitting tolerance ε.*

	N_{prop}	$\hat{P}(I)$	CPU time (h)
MC	54114	$3.40{\cdot}10^{-2}$	0.004
GMM ($\varepsilon = 10^{-1}$)	36	$3.18{\cdot}10^{-2}$	0.025
GMM ($\varepsilon = 10^{-2}$)	>10^3	n/a	n/a

Table 4.1 shows the issue using preliminary numerical results (number of propagations, probability estimate, and computational time) for two values of the splitting tolerance ε to show the sensitivity of the splitting process, and comparing them with the ones obtained for the MC analysis already presented in Table 3.3 from Chapter 3, but considering only the impacts occurring during the first close encounter with Venus. In particular, the number of propagations represents, in the case of MC, the number of initial conditions propagated forward in time, and, in the case of GMM, the total number of Gaussian components that were obtained by splitting during the propagation. Fig. 4.3 shows the state uncertainty distribution at the epoch of the closest approach projected onto the reference planes in the equatorial reference frame centres in the solar system barycentre, highlighting the means of the GMM components (red dots) and the constant-value curves of the resulting pdf.

These partial results show that even a relatively large value splitting tolerance ε, equal to 10^{-1} in this case, is enough to obtain an estimate for the impact probability that is in line with the results validated via MC simulation. However, a stricter tolerance

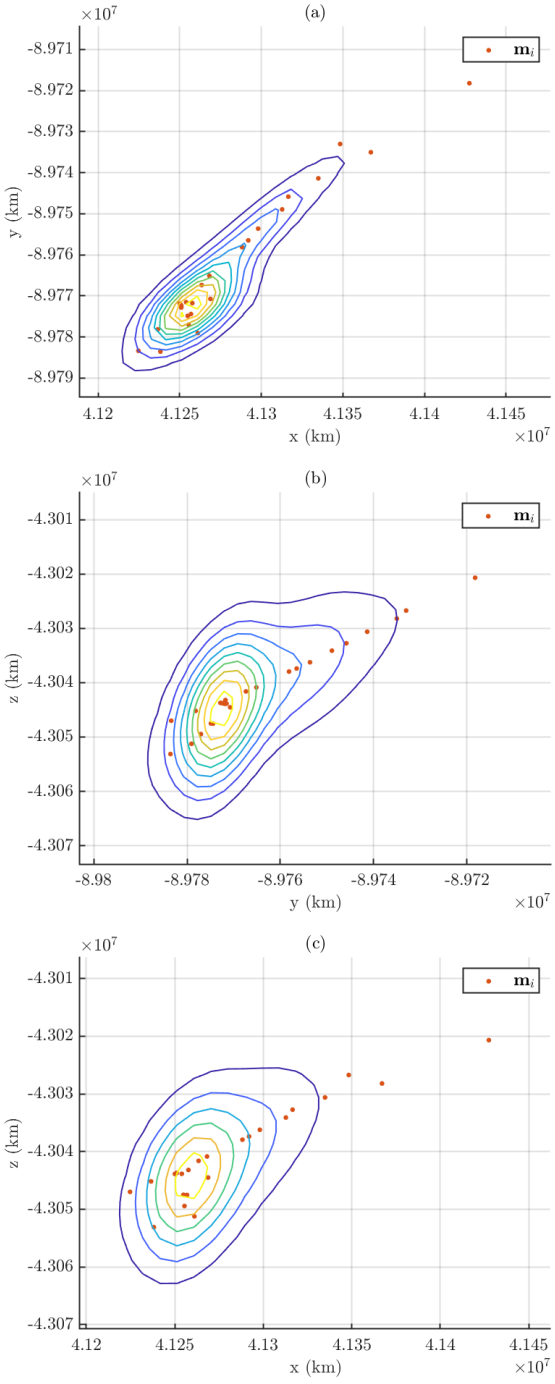

Figure 4.3: *Plot of the pdf representing the uncertainty of the launcher upper stage of the Solar Orbiter mission on the epoch of the impact with Venus, on the x-y plane (a), the y-z plane (b), and the x-z plane (c), obtained using a splitting tolerance of 10^{-1}. The red dots indicate the means of the GMM components, while the contour lines represent the level curves of the approximated pdf.*

equal to 10^{-2}, only one order of magnitude lower, causes the GMM set to split out of control even before reaching the close encounter with Venus, with no possibility to obtain any results regarding the impact probability.

The most likely explanation to this phenomenon may reside in the lack of an updating step aimed at maintaining the overall accuracy of the approximated uncertainty distribution. Instead of focusing simply on the single components separately and on how accurately each of them can be described as Gaussian, the analysis should also focus on how well the properties of the overall pdf are maintained during the propagation: whenever the number of components is changed, the weights of the GMM set should be recomputed to account for the new elements. This would allow the GMM approximation to preserve the properties of the global pdf more accurately.

The author of this thesis points out that they are aware that the tolerance value reported in Table 4.1 is large. However, this value was chosen only to show how the adaptive GMM propagation works and how it was used to estimate the probability of an impact without relying on the splitting process to carry out the propagation. The adaptive splitting of the GMM components is of course necessary to maintain a high level of accuracy for a planetary protection analysis, but this topic will be addressed in future work.

Possible solutions to this issue are proposed in the next section.

4.5 Summary

This chapter focused on the application of GMM techniques for uncertainty propagation to planetary protection analysis, with the aim of improving the estimation of impact probability required to verify the compliance of a space mission to the requirements. Initially, this would be achieved by analysing the evolution of the initial uncertainty distribution without the limitations of sampling techniques, such as the need to propagate large number of random initial conditions to provide high accuracy to the solution, with high computational cost.

In the first part, the theoretical background and the main numerical algorithms adopted here were introduced, focusing on the reasons behind the choice of GMM to propagate the initial state uncertainty of the subjects of planetary protection analysis. In particular, a propagation method based on the Unscented Transformation is adopted, to allow the propagation of the GMM set without resorting to linearised methods. Together with the UT, a method to adapt the number of GMM components based on differential entropy was applied to reduce the effects of the non-linear dynamics on the approximated representation of the pdf during the propagation.

In the second part of the chapter, an example was presented, both to show how the probability of impact can be estimated with the use of GMM, and to address numerical problems related to the splitting algorithm generating an excessive number of components during the propagation, due to missing control routines to maintain the accuracy of the overall uncertainty approximation. Possible solutions to this issue and improvements of the selected algorithm are discussed in the next section.

Possible solutions and improvements

As already hinted at in the previous section, the main cause of the uncontrolled splitting during the propagation may be the lack of a step to check the accuracy of the whole approximated uncertainty distribution. While monitoring the differential entropy for a single Gaussian component (or any other estimator of the non-linear effects acting on it) ensures that its representation of the uncertainty remains faithful to the Gaussian description during the propagation, the accuracy of the probability distribution represented by the GMM set is not guaranteed to remain accurate when considered in its entirety.

Two solutions can be adopted in order to reduce the growing inaccuracy of the GMM approximation, that are an update of the weights associated with each Gaussian component, and a check to determine whether and when two or more components should be merged into a single one, or pruned to reduce the computational complexity. The first solution has already been addressed by Terenjanu et al. [65] and Vishwajeet et al. [112], who proposed algorithms to update the weights of the GMM every time the number of components is changed, by minimising the error related to the Fokker-Plank equation over the entire distribution. The second solution has also been explored by Vishwajeet et al., who measure the distance between two components via the Kullback-Leibler divergence [116] two determine whether they should be merged, and by DeMars et al. [117], who use instead the L_2 distance.

On a different note, the estimation of the impact probability itself can be improved: one possible approach, still based on sampling each Gaussian components, would be using of Line Sampling instead of a standard MC in order to increase the accuracy of the results; another approach, instead, would rely on the numerical evaluation of integrals defined over the intersection volume between the Gaussian components and the planet, in a way similar to the ones proposed by Vittaldev and Russel [69] and DeMars et al. [110] for conjunction analysis between Earth-orbiting satellites and space debris. Some of these improvements will be addressed in future work.

CHAPTER 5

SNAPPshot

5.1 Introduction

As introduced in section 1.3.4 of Chapter 1, SNAPPshot is a software tool suite originally developed in 2016 at the University of Southampton under a contract for the European Space Agency in order to support Mission Analysis activities at ESOC related to planetary protection [5, 56, 57].

The work on SNAPPshot has been continued at Politecnico di Milano as part of this research and several modifications have been introduced into the software during the PhD research, following two main needs: on the one hand, implementing all the numerical algorithms developed during the doctoral research into a software which already provided functionalities such as propagators, ephemeris models, routines for Monte Carlo analysis, routines for the study of the b-plane and resonance, and others that will be explained later in this chapter; on the other hand, sustaining the effort of the Mission Analysis team at ESOC of establishing SNAPPshot as the single tool capable of dealing with all analyses related to planetary protection, as part of the NPI activities and the COMPASS project. For this last reason, a final version of the software will be delivered to ESA at the end of the PhD research.

In this chapter, a general introduction on the architecture of the software will be given, followed by a breakdown of the functionalities that were present at the start of the project, and in the current version, including all the modifications to the code made by the author of this thesis as part of the PhD research.

5.2 General architecture of the code

The software, written in Modern Fortran, is organised in drivers and modules: the drivers, when compiled, provide the executables that are called by the user; the modules collect all the subroutines and functions used in the code. Different drivers are available depending on the execution mode that is chosen by the user.

When calling the drivers, the user also provides a fixed-format input file, which sets the main parameters and data for the simulation to be run: execution mode, settings for the propagator, initial conditions and other trajectory-related data, paths to secondary files providing additional data, paths to save the output files.

A configuration file is also present, containing some parameters related to memory allocation (e.g. maximum size of arrays) and general settings for the simulation, which are expected to be kept constant among different cases.

The results of the simulations are then saved into different output files to be later analysed in post-processing by the user.

5.3 Functionalities available at the start of the PhD research

Execution modes

The tool provides three separate execution modes:

- verification of the compliance with planetary protection requirements in the case when the uncertainty of the initial state is described by a covariance matrix, as in the case of the study of the dispersion of the trajectory of a launcher;
- verification of the compliance with planetary protection requirements in the case when the uncertainty of the initial state is described by a distribution of $\Delta\mathbf{v}$ vectors, reproducing the case where the execution of a manoeuvre is affected by errors;
- verification of the compliance with planetary protection requirements in the case of a failure of the propulsion system of the spacecraft;
- verification of the compliance with planetary protection requirements in the case when an uncertainty in the initial epoch is present;
- verification of the compliance with planetary protection requirements in the case when the trajectory of the object and its dispersion evolution are given in separate files;
- propagation of a single initial condition.

Initial conditions and uncertainty

The initial conditions are specified by the user in the input file:

- epoch,
- position and velocity vectors,

- reference system where the initial conditions are provided (centred in the Sun or in the solar system barycentre, and oriented as the ecliptic plane or as the equatorial plane);

The initial uncertainty is also set in the input file or files as:

- a 6×6 covariance matrix defined in the J2000 reference frame, or
- a distribution of $\Delta\mathbf{v}$ vectors expressed in magnitude and direction, or
- a time window when the failure of the propulsion system can happen, and the points along the trajectory where the failure can occur, indicating a secondary fixed-format file containing the trajectory data, or
- a distribution of initial epochs, or
- a series of covariance matrices defined at different epochs on a reference trajectory.

Dynamics model

The propagator considers three perturbations

- the gravitational perturbation of an external celestial body (the user can select only 11 bodies, the planets from Mercury to Neptune, Pluto, the Sun, and the Earth's moon, in a fixed-ID format),
- the Earth oblateness perturbation (J_2 effect),
- the solar radiation pressure effect according to a cannonball model (the user specifies the type of area-to-mass ratio distribution, the parameters describing it, and the reflectivity coefficient).

The ephemeris model is chosen by the user among:

- a built-in analytical model, or
- a routine by ESA, or
- SPICE (in which case a metakernel file has to be provided).

All physical constants are either hardcoded or defined via the ephemeris files.

Propagator setup

The user selects the integration scheme:

- classical Runge-Kutta (with regularised step control),
- Dormand-Prince RK4(3) (adaptive step) [118],
- Runge-Kutta-Fehlberg (with regularised step control) [119],
- Dormand-Prince R5(4) (adaptive step) [23],
- Runge-Kutta of 8^{th} order (with regularised step control) [120],
- Dormand-Prince R8(7) (adaptive step) [25].

Simulation and post-processing

How the tool works was already described in Fig. 1.1 in Chapter 1.

The initial data provided by the user is used to sample the uncertainty distributions provided by the user and generate the random initial conditions to be propagated in the MC analysis. During the integration of each trajectory, the tool verifies the occurrence of impacts, halting the simulation if any is detected.

In post-processing, the trajectories are re-analysed using the b-plane representation to:

- verify the presence of possible impacts that were not detected during the integration,
- verify the presence of orbital resonances with any of the selected bodies.

The output files contain information about all close approaches detected during the MC simulation, as well as for the nominal trajectory:

- body of the close approach,
- epoch of SOI entry,
- b-plane coordinates at SOI entry,
- epoch of closest approach,
- b-plane coordinates at closest approach,
- whether an impacts with the body occurs,
- whether resonances with any of the bodies included in the simulation are present after the fly-by,
- the state (position and velocity vectors) of the propagated object at each time step of the propagation (only for the nominal trajectory).

A parallel execution mode is available, the number of threads to be used must be specified by the user.

5.4 Modifications made during the PhD research

5.4.1 General changes

The changes to the general structure of the code include major modifications to the ephemeris model and to the propagation setup, especially the equations of motion and the detection of events. Some of the changes that were implemented during this period required significant alterations of the code structure.

The management of the ephemerides was changed to be able to identify any body in the solar system without a fixed-ID input format. The Sun, planets, moons, asteroids, comets and spacecraft are now identified via their NAIF IDs using the JPL Horizons ephemeris system (`https://ssd.jpl.nasa.gov/horizons.cgi`)

via the SPICE toolkit (`https://naif.jpl.nasa.gov/naif/`)), on the condition that the necessary ephemeris data is also provided. This is done in the ephemerides reading process, in the propagation of the selected body (asteroid or spacecraft) and in the detection process (e.g. impacts or close approaches detection).

The user is now able to overwrite the physical constants defined by the tool (using hardcoded values or according to the selected ephemeris model) using an additional input file.

Also, the user is now able to select a reference system centred in any of the bodies included in the simulation using a second input file, while the previous setup allowed to integrate with respect to the solar system barycentre only.

The equations of motion were changed to allow the user to switch on/off all perturbations, which include the 3rd body perturbation when the selected integration centre the solar system barycentre, and Jupiter's oblateness perturbation.

The propagator is also capable of detecting the escape of the propagated object from a sphere of influence and of stopping the integration.

5.4.2 Modifications related to the PhD research

Together with the modifications that were agreed upon with the Mission Analysis team of ESA, all the algorithms used to carry on this PhD research that were described in the previous chapters were also implemented. In this case, the new functionalities were added to SNAPPshot by defining ad hoc drivers and separate modules which maintain the same structure of the main code in the matters of executables and of input and output files.

Line Sampling analysis

The LS-based algorithm that is represented in section 3.3 from Chapter 3 was also implemented in SNAPPshot, modifying the structure of the tool from the way described in in Fig. 1.1 in Chapter 1 to what is schematised in Fig. 5.1.

In this kind of analysis, the user provides an additional input file to define the main parameters used to run the LS analysis and the associated algorithms:

- the maximum number of LS runs,
- the number of samples used in the Markov Chains, and the scaling factor for the proposal distribution,
- the maximum number of iterations used to sample the lines during the numerical LS analysis, and the interpolation tolerance to stop the iterative process,
- whether to use the algorithm to correct the main sampling direction or not,
- whether to perform a multi event analysis or not, indicating also the maximum number of runs for the preliminary MC and its probability and confidence levels.

The analysis is performed as described in Fig. 3.5 from Chapter 3:

1. the tool reads the input files;

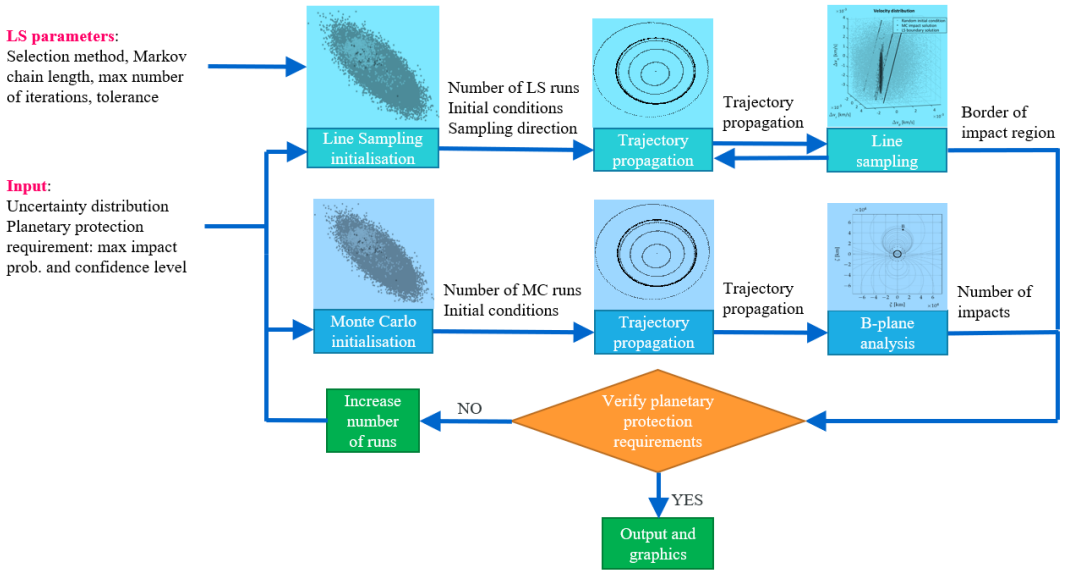

Figure 5.1: *SNAPPshot building blocks including the LS procedure.*

2. the preliminary MC is run according to the parameters specified by the user;
3. the data about the close approaches is post-processed to identify the close approach windows and assign a priority to each of them;
4. for each window, a Markov Chain is started until the maximum length is reached or impacts with any body included in the propagation are detected;
5. if no impacts are detected, the analysis moves to the next close approach window with the highest priority;
6. if impacts are detected, an initial guess for the sampling direction is estimated, and then corrected using the algorithm presented in section 3.3.1 of Chapter 3;
7. the main LS analysis is run, estimating the impact probability for each impact region and the associated standard deviation.

The output files include all data computed during the various phases of the analysis and the final results:

- the initial states used for the preliminay MC run, and the data related to recorded close approaches (if any),
- the initial states generated by the Markov Chain sampling phases;
- the points along the sampling lines corresponding to the borders of the identified impact regions, in terms of the c parameter (as defined in section 3.2.1 of Chapter 3), and the relative sampling direction;
- the probability and standard deviation associated with each impact region;

- performance data, such as number of propagations and computational time.

Each of the steps of the analysis required the implementation of different algorithms, which were described in detail in Chapter 3:

- the algorithm for merging the time intervals of each fly-by found via the preliminary MC and define the CA windows (Section 3.3.2);
- the Metropolis-Hastings algorithm for generating the Markov Chains used to explore the CA windows (Section 3.2.1);
- the algorithm for correcting the initial guess of the sampling direction (Section 3.2.1), with:
  - the definition of the orthonormal base,
  - the multi-linear regression;
- the LS algorithm 3.2.1, with:
  - the transformation to the normalised coordinate space (Section 3.2.1 and Appendix B),
  - the iterative algorithm to sample the impact region along each line and identify its boundary (Section 3.2.1).

GMM propagation

Similarly to what was done for the LS implementation, the algorithms that are presented in Chapter 4 were also implemented in SNAPPshot.

Also in this kind of analysis, the user provides an additional input file to set up the simulation and the algorithms used for the GMM propagation:

- the number of elements to split the GMM components;
- the tolerance used to stop the propagation and split a component when necessary;
- the maximum number of GMM components being propagated at a time, and the maximum number of times a component is allowed to be split;
- whether to pre-split the initial covariance before the analysis;
- the number of random samples generated when computing the impact probability during a fly-by, with the desired confidence level.

The analysis is performed as described Chapter 4:

1. the tool reads the input files;
2. the propagation is set up by computing the differential entropy of the nominal distribution, and by splitting it if requested by the user;
3. a GMM component is selected, the sigma points are computed, and the propagation is started, monitoring the differential entropy error at any time step;

4. when the error grows beyond the given tolerance, the propagation is stopped and the component currently being propagated is split (if possible);
5. the propagation is resumed, starting from the next element in line;
6. if a close approach with a celestial body occurs, the propagation is stopped at the closest point and the probability of impact for the single GMM is estimated;
7. the propagation is continued until a split occurs or the final time is reached;
8. the simulation stops when all the GMM components have reached either the maximum number of splits or the final time of the propagation.

The output files include all data related to the GMM components at the end of the propagation:

- the weight, mean, and covariance matrix of each Gaussian component, together with the reference epoch;
- the associated partial impact probability;
- final results and performance data, such as the total impact probability, the number of propagations and the computational time.

Each of the steps of the analysis required the implementation of different algorithms, which were described in detail in Chapter 4:

- the algorithm for splitting a Gaussian distribution (section 4.3.1);
- the algorithm for computing the sigma points of a Gaussian distribution (Section 4.3.3);
- the algorithm for propagating the set of sigma points and adaptively split the corresponding Gaussian distribution (Section 4.3.2).

5.5 Work in progress

Work is being currently done to expand further the functionalities of the SNAPPshot tool. This expansion follows the work done for this PhD research, as well the work done by Alessandro Masat from Politecnico di Milano for his M.Sc. Thesis "B-plane orbital resonance analysis and applications, Perturbed semi-analytical model for planetary protection and defence applied to ballistic resonant flyby design" [91] which is co-supervised by Prof. Colombo and the author of this thesis:

- inclusion of additional integration methods in the available pool of the tool;
- improvement of the current implementations of the LS and GMM methods;
- new model to account for relativistic effects during the propagation (by A. Masat);
- new analytical b-plane representation and definition of orbital resonances, extending the theory of Valsecchi et al. [95] (by A. Masat).

CHAPTER 6

Conclusions

Exploration missions to other celestial bodies increase the risk of unintentionally contaminating them with biological material from Earth, due to collisions between uncontrolled spacecraft or launcher stages and planets and moons that may present extraterrestrial life. For this reason, all interplanetary mission must comply to internationally agreed-upon guidelines aimed at reduce the chance of these kind of events. However, chaotic n-body dynamics and uncertainties in the initial state determination of spacecraft or other mission-related objects make tackling this problem difficult when high precision is require.

This thesis presented a variety of numerical techniques aimed at improving the current approach to planetary protection analysis. Some of these techniques were adapted and applied in a context different from the one originally intended, others were developed for this specific purpose.

This chapter provides an overview of the work done in this research, summarising and commenting the main results. Some remarks for future work will be given starting from the considerations previously made.

6.1 Summary and contributions of the thesis

As introduced already in Chapter 1, the main goal of the research presented in this thesis is to improve the accuracy and the efficiency of planetary protection analysis for interplanetary space missions, reducing the cost of the verification that said missions are compliant with the planetary protection requirements. The complexity of this task arises from different aspects of the problem under study, some related to the available tools to solve it and other related to the problem itself.

Depending on the outcome of the analysis, the design of the mission may have to be

adjusted, meaning that the verification of the compliance to the requirements demands efficiency and accuracy. Commonly applied methods, such as Monte Carlo simulations, while managing to capture the non-linearity of the orbital dynamics, fail to to approach the problem efficiently when high precision is need. For this purpose, the research focused on bring improvement in three primary aspects: numerical orbital propagation, uncertainty sampling, and uncertainty propagation.

The main findings of this research were validated through numerical simulations with the use of several test cases:

- propagation of Near-Earth Asteroids to validate the integration methods presented in Chapter 2 due to their known orbits:
  - 99942 Apophis,
  - 2010 RF_{12},
  - 2007 UD_6;
- planetary protection analysis of different interplanetary missions:
  - the launcher upper stage of the Bepi Colombo mission, to validate the proposed integration methods on a statistical level;
  - the orbiter of the JUICE mission, to validate the proposed technique to detect close approaches based on the Jacobian of the equations of motion;
  - the launcher upper stage of the Solar Orbiter mission, to validate the LS algorithms and the GMM propagation;
  - the orbiter of the Mars Sample Return mission,to validate the LS algorithms.

Numerical orbital propagation

The work done about numerical propagation was aimed at studying how the numerical errors grow during the integration of single trajectories, and how this affects the overall planetary protection analysis when scaled up to statistical levels, with thousands of trajectories considered. This task was carried out by analysing the performance of a selection of integration methods (including standard Runge-Kutta methods, Runge-Kutta methods based on Gauss-Legendre quadrature, Runge-Kutta-Nystrom methods, and the symplectic Yoshida method) when applied to different problems of orbital propagation, ranging from single trajectories of asteroids to planetary protection analyses of interplanetary missions. The test cases were chosen taking into account the effects of the non-linear n-body dynamics over the integration process, studying in particular the influence of close approaches with planets on the orbital state error and on the conservation of the integrals of the motion (the total mechanical energy firstly). For this reason, some of the selected methods were in the class of symplectic methods, which are formulated in order to preserve the conserved quantities of the dynamic system.

The results of the various numerical simulations allowed to reach different conclusions on the effectiveness of the selected methods in various situations, and to develop new approaches to the problem.

In particular, the propagations of asteroids (chosen for their well known orbits and for their resonant close passages to the Earth's orbit) showed that, out of the analysed

methods, the symplectic Yoshida method can provide better energy conservation during the integration at a similar computational cost with respect to standard methods such as explicit Runge-Kutta schemes. However, this result was valid only until the distance between the object being propagated and the other massive celestial bodies is large enough. During close approaches, in fact, the faster dynamics magnifies the small numerical errors that had accumulated up to that point, in a manner that is common to all the selected integration schemes. In this cases, the implicit Gauss-Legendre RK method showed the best behaviour among the selected methods, despite its performance being worse with respect to the cases with no close encounters. The same methods were also applied to impact analysis, using both asteroids and interplanetary missions as test cases, finally, to prove that the differences in the propagation of single trajectories do not strongly influence the result of a Monte Carlo simulation.

These tests allowed to select the implicit symplectic Gauss-Legendre RK method to be implemented in SNAPPshot along with the already available explicit schemes due to its accurate performance in both kinds of test cases.

Finally, to address the problems observed when propagating planetary close encounters with any integration method, a novel technique for identifying those conditions was proposed, in order to recognise autonomously the conditions that increase the numerical error during the integration.

This method introduces a criterion to detect when a close approach with a massive body is occurring during the integration of a trajectory without relying on a threshold based on a fixed distance (e.g. the radius of the sphere of influence or of the Hill sphere) or a fixed relative velocity. It exploits the Jacobian matrix of the equations of motion to provide a less strict definition of close approach: this definition is based on the eigenvalues of the matrix and on their derivatives, separating the various contributions given by each planet included in the propagation. In this way, a close approach can be defined when the contributions given by a planet grows larger than the one given by the central body of the system (the one with the greatest gravitational influence on the trajectory), meaning that the body whose effect on the dynamics is becoming dominant is the one being approached.

This criterion results in a definition of close approach based not only on the relative distance between the body being propagated and the approached body, but also to the relative speed, comparing these quantities between the approached body and the central body. This allows to identify close approaches, or to detect those conditions that affect the quality of the numerical integration, even when there is no clear crossing from one SOI to another. This carries the advantage of not missing those fly-bys that, despite occurring relatively far from the planet, still have an impact on the numerical propagation. These considerations were proven in different examples comparing distance-based definitions to the proposed one.

Uncertainty sampling techniques

The work about sampling was aimed at making the statistical analysis performed to verify the planetary protection requirements more efficient, to reduce its computational cost. In fact, high accuracy is needed to perform such analysis, as the probability values to be verified are often very small, with strict confidence levels associated to them.

For this reason, different sampling techniques were studied and the Line Sampling method was selected, based on a comparison with standard MC and Subset Simulation, as an alternative to standard Monte Carlo simulation.

The LS method uses lines following a reference direction instead of points to sample the uncertainty space, identifying the boundaries of the impact regions inside of it and computing the impact probability using integrals along these lines where they intersect the impact regions. The integrals are evaluated analytically, in this way the LS method can provide an estimation of the impact probability that has a lower variance (thus can be considered more accurate) than the one given by standard MC when the same number of samples are used, or reach a similar accuracy using fewer samples.

The higher accuracy of LS is also proven theoretically in the available literature, which points out two significant aspects of this sampling technique: the LS method is always more accurate than standard MC, or at least as accurate in the worst case; the reference direction used to define the sampling lines is one of the parameters the affect the performance of LS the most. In particular, an ideal case for the technique is represented by the sampling direction being orthogonal to the border of the impact region. This finding was confirmed by this work with further analysis of the theoretical formulation, which also showed the dependency of the numerical performance of LS from the shape and the extension off the impact region inside of the uncertainty space.

The application of the LS method to planetary protection analysis was divided in two phases: the first part of the work focused on assessing the capabilities of LS at estimating the probability of impact with a celestial body when a single event is considered, while the second part extended its application to cases with multiple events (as found in most cases) by introducing newly developed algorithms to support it.

The first findings confirmed the higher accuracy of LS in estimating low probability levels, after being applied to impact analyses of asteroids and interplanetary missions: when compared to standard MC, the LS method was capable of correctly estimating the impact probability and identifying the boundaries of the impact region, reaching the same accuracy after fewer propagations, or, vice-versa, returning more accurate results when the same number of propagations was preformed.

Moreover, the theoretical formulation of LS already existing in the literature, which illustrates analytically the higher accuracy of the method with respect to standard MC, was extended further through analytical manipulation. An approximate formula was developed to give a more in-depth view on how LS compare to MC, highlighting the dependency of the overall accuracy from the determination of the main sampling direction and from the shape of the impact region. These aspects were confirmed by the results of the simulations: sampling an impact region with a flat (or almost flat) and extended shape gives more accurate results than sampling one with a clumped shape; a sampling direction that is orthogonal, or quasi orthogonal, to the boundary of the impact region allows a more accurate estimation of the probability.

In the second part, two novel algorithms were devised to support the application of LS to cases where multiple close approaches with planes, and thus multiple impact regions, are expected, as more commonly found in planetary protection analysis, where

propagation times up to 100 years are considered.

One algorithm uses the information gained from a preliminary MC analysis to identify the time intervals where most close approaches are clustered in the considered time frame, by recording the encounters and then merging them to define close approach windows.

The second algorithm, instead, uses an initial guess for the sampling direction to perform a short LS analysis and obtain a general idea of the position and phase of an impact region. This is then approximated as a hyperplane using linear regression: a new guess for the sampling direction is obtained, in a way that is closer to the ideal case of a sampling direction orthogonal to the boundary of the impact region, under the hypothesis that this approximation is valid. This greatly improves the accuracy of the method without increasing significantly the computational load, since it allows to sample the impact region in a more optimal way.

These algorithms were used in a numerical procedure based on LS, which first identifies the close approach windows and the explores them to find actual impact regions: in case one is found, it is sampled using LS to estimate the impact probability associated with that event, and the process is repeated for all close approach windows. The numerical test using interplanetary mission cases confirmed the greater efficiency of this LS-based procedure with respect to standard MC.

Moreover, in this chapter the main parameters which affect the performance of the LS method were identified. Their influence on the accuracy of the final result and on the computational load was discussed: in particular, the sample size for the preliminary analysis, the length of the Markov chains, and the number of sampling lines greatly affect the capabilities of the method to identify the impact regions and to sample them correctly to obtain an accurate estimation of the impact probability. Some criteria useful for quantifying these parameters depending on the expected probability level to be verified were suggested based on trade offs, and values were suggested based on the test cases that were presented.

Uncertainty propagation methods

Uncertainty propagation techniques were also studied as an alternative to sampling the initial uncertainty distribution, for studying the evolution of the initial uncertainty and estimate the probability of impacts without the limitations of sampling techniques, such as the need to propagate large number of random initial conditions to provide high accuracy to the solution, with high computational cost. On the contrary, the direct propagation of the initial uncertainty distribution allows deeper analysis during and after the propagation.

The approach that was adopted makes use of Gaussian Mixture Models to approximate the uncertainty as a weighted sum of Gaussian distributions, allowing the exploitation of their properties. The Unscented transformation was adopted to propagate the GMM set in a fully non-linear model, without relying on linear or other kind of approximations, thus capturing the true physics of the problem. Moreover, during the propagation, the number of GMM components was varied by making use of splitting techniques to contain the effects of the non-linear dynamics, which distorts the distributions until a Gaussian description is not valid any more.

This approach was used to propagate the initial uncertainty of an interplanetary mission and to estimate the probability of an impact. However, numerical problems related to the splitting algorithm generating an excessive number of components were observed and commented. Possible solutions to this issue and improvements of the selected algorithm were discussed, proposing control techniques to maintain the accuracy of the overall uncertainty approximation based on the analysis of the overall GMM instead of focusing only on the single components.

6.2 Limitations and remarks for future work

Along with numerous positive findings, the numerical tests performed to apply the techniques presented in this thesis and assess their performance for planetary protection analysis also revealed issues and possible improvements that are discussed in this section.

On the side of numerical propagation, two main aspects which would benefit from different approaches for improving them were found.

On the one hand, the selection of integration methods itself could be expanded, in order to include more symplectic methods, such as the SABA methods by Laskar and Robutel [15], or methods to account for close approaches with planets such as the ones from Duncan et al. [17] and Chambers [16]. Moreover, non-symplectic methods different other than RK could also be studied, for example Adams-Bashforth methods and other variable-order variable-step schemes. Future work will also focus on improving the implementation of the methods that were already considered, such as the implicit symplectic Gauss-Legendre RK.

On the other hand, more effective ways to represent a close approach during the propagation should be considered or developed. For starters, future work will focus on the consistent application of the Jacobian-based technique for fly-by detection to improve the propagation methods currently available, especially for the determination of close approach windows in the LS analysis: this will ensure that no potential impact region is missed during the preliminary survey with MC for identifying the close approach windows. Then, an analysis of the evolution of the b-plane coordinates during the integration of a close approach will also be addressed.

From the point of view of the LS-based techniques, various topics can be subject of future studies to improve the effectiveness and precision of the proposed approach.

To improve the efficiency of the LS-based procedure, a study aimed at quantifying the sensitivity of the proposed approach on the various parameters affecting its performance shall be done: the number of runs in the preliminary MC, the length of the Markov chains, the iterative method to sample the lines are some of the most important factors on which the LS techniques work. Several numerical simulations are required to assess the effect of their variability on the algorithm and to identify optimal values to obtain a good trade off between accuracy and efficiency. Moreover, the application of other advanced sampling methods, such as Subset Simulation, together with the LS could improve the overall efficiency of the planetary protection analysis: in particular, SS could be employed to improve the preliminary MC analysis for the identification of

potential impact regions.

Another relevant aspect that will be addressed in future work is the determination of the exact number of runs that are required to reach a given confidence level using LS, as already available in SNAPPshot for the standard MC. This will require to further expand the theoretical definition of the methods as presented in Section 3.2.3 of Chapter 3: in particular, an expression of the confidence level obtained via LS that correlates the number of sampling lines and the estimated probability level shall be determined.

Finally, improvements in the general time and memory management of the LS procedure would also be desirable, along with the generalisation of the algorithms to make them applicable also to problems that are not related to planetary protection analysis.

Finally, regarding the use of uncertainty propagation techniques, different aspects could be improved, on top of the issues that were already observed and discussed in Chapter 4.

Alternative criteria and methods to split the distributions will be studied in future work, with the aim of increasing the accuracy and the efficiency of the GMM propagation. To fulfil this particular goal, merging techniques in particular will be considered in an effort to reduce the computational cost of the simulation, along with the pruning of those Gaussian components with weights so low that their contributions to impact probability would be negligible.

As already introduced as a final remark in Chapter 4, different ways of estimating the impact probability will be analysed, to exploit the higher precision of Line Sampling or integral evaluation.

APPENDIX $\mathcal{A}$

Implemented integration methods

This appendix reports the coefficients used to construct the integration methods introduced in Section 2.3 of Chapter 2 and then used to perform orbital propagations in Section 2.4.

Runge-Kutta integration methods

For the RK and GLRK methods, the coefficients are reported using their Butcher's tableau. This is defined again here, as it was defined in Section 2.3 from Chapter 2.

A single step of integration from t_n to $t_{n+1} = t_n + h$ following an explicit RK scheme is expressed as [22]:

$$x_{n+1} = x_n + hF(t_n, x_n, h; f), n \geq 0 \tag{A.1}$$

$$F(t_n, x_n, h; f) = \sum_{i=1}^{s} b_i K_i \tag{A.2}$$

$$K_i = f(t_n + c_i h, x_n + h \sum_{j=1}^{s} a_{ij} K_j), \quad i = 1, 2, \ldots, s \tag{A.3}$$

where x_n is the solution at the current step, t_n the value of the independent variable at the current step, h the step size, f the function to integrate, F is the increment function, s is the number of stages of the method, and a_{ij}, b_i, c_i are the coefficients that define a specific Runge-Kutta method. They are usually indicated as the Runge-Kutta matrix (a_{ij}), the vector of weights (b_i), and the vector of nodes (c_i); they are collected in the *Butcher tableau* $(\mathbf{a}, \mathbf{b}, \mathbf{c})$

$$\begin{array}{c|ccc} c_1 & a_{11} & \dots & a_{1s} \\ \vdots & \vdots & & \vdots \\ c_s & a_{s1} & \dots & a_{ss} \\ \hline & b_1 & \dots & b_s \end{array}$$

that completely define a Runge-Kutta method.

Classical Runge-Kutta method RK4 Four stages, fourth order, explicit, fixed step:

0				
1/2	1/2			
1/2	0	1/2		
1	0	0	1	
	1/6	1/3	1/3	1/6

Dormand-Prince RK5(4) Seven stages, fifth order, explicit, variable step, from Dormand and Prince (1980) [23]:

0							
1/5	1/5						
3/10	3/40	9/40					
4/5	44/45	-56/15	32/9				
8/9	19372/6561	-25360/2187	64448/6561	-212/729			
1	9017/3168	-355/33	64732/5247	49/176	-5103/18656		
1	35/384	0	500/1113	125/192	-2187/6784	11/84	
	5179/57600	0	7571/16695	393/640	-92097/339200	187/2100	1/40
	35/384	0	500/1113	125/192	-2187/6784	11/84	0

Gauss-Legendre Runge-Kutta GLRK4 Two stages, fourth order, fixed step, from Butcher (1964) [121]:

$$\begin{array}{c|cc} 1/2 - \sqrt{3}/6 & 1/4 & 1/4 - \sqrt{3}/6 \\ 1/2 + \sqrt{3}/6 & 1/4 + \sqrt{3}/6 & 1/4 \\ \hline & 1/2 & 1/2 \end{array}$$

Gauss-Legendre Runge-Kutta GLRK6 Three stages, sixth order, fixed step, from Butcher (1964) [121]:

$$\begin{array}{c|ccc} 1/2 - \sqrt{15}/10 & 5/36 & 2/9 - \sqrt{15}/15 & 5/36 - \sqrt{15}/30 \\ 1/2 & 5/36 + \sqrt{15}/24 & 2/9 & 5/36 - \sqrt{15}/24 \\ 1/2 + \sqrt{15}/10 & 5/36 + \sqrt{15}/30 & 2/9 + \sqrt{15}/15 & 5/36 \\ \hline & 1/2 & 1/2 & \end{array}$$

Gauss-Legendre Runge-Kutta GLRK8 Four stages, eighth order, fixed step, from Butcher (1964) [121]:

$\sum_{j=1}^{4} a_{1j}$	w_1	$w_{11} - w_3 + w_{44}$	$w_{11} - w_3 - w_{44}$	$w_1 - w_5$
$\sum_{j=1}^{4} a_{2j}$	$w_1 - w_{33} + w_4$	w_{11}	$w_{11} - w_{55}$	$w_1 - w_{33} - w_4$
$\sum_{j=1}^{4} a_{3j}$	$w_1 + w_{33} + w_4$	$w_{11} + w_{55}$	w_{11}	$w_1 + w_{33} - w_4$
$\sum_{j=1}^{4} a_{4j}$	$w_1 + w_5$	$w_{11} + w_3 + w_{44}$	$w_{11} + w_3 - w_{44}$	w_1
	$2w_1$	$2w_{11}$	$2w_{11}$	$2w_1$

with $w_1 = 1/8 - \sqrt{30}/144$, $w_{11} = 1/8 + \sqrt{30}/144$, $w_2 = \sqrt{(15 + 2\sqrt{30})/35}/2$, $w_{22} = \sqrt{(15 - 2\sqrt{3})/35}/2$, $w_3 = w_2(1/6 + \sqrt{30}/24)$, $w_{33} = w_{22}(1/6 - \sqrt{30}/24)$, $w_4 = w_2(1/21 + 5\sqrt{30}/168)$, $w_{44} = w_{22}(1/21 - 5\sqrt{30}/168)$, $w_5 = w_2 - 2w_3$, $w_{55} = w_{22} - 2w_{33}$.

Runge-Kutta-Nyström methods

The RKN methods use two different sets of coefficients to integrate the coordinates and the momenta separately. For the integration step of length h which brings $(\mathbf{r}_n(t_n), \mathbf{v}_n(t_n))$ onto $(\mathbf{r}_{n+1}(t_{n+1}), \mathbf{v}_{n+1}(t_{n+1}))$ the algorithm follows:

$$\begin{cases} \mathbf{r}_{n+1} = \mathbf{r}_n + h\mathbf{v}_n + h^2 \sum_{i=1}^{s} b_i f(t_n + c_i h, \mathbf{K}_i) \\ \mathbf{v}_{n+1} = \mathbf{v}_n + h \sum_{i=1}^{s} d_i f(t_n + c_i h, \mathbf{K}_i) \\ \mathbf{K}_i = \mathbf{r}_n + c_i h \mathbf{v}_n + h^2 \sum_{j=1}^{s} a_{ij} f(t_n + c_j h, \mathbf{K}_j), \quad i = 1, ..., s \end{cases} \tag{A.4}$$

with a Butcher's tableau $(\mathbf{a}, \mathbf{b}, \mathbf{c}, \mathbf{d})$, where $\mathbf{b}$ are the coefficients used for the coordinates, and $\mathbf{d}$ the coefficients for the momenta:

c_1	a_{11}	$\dots$	a_{1s}
$\vdots$	$\vdots$		$\vdots$
c_s	a_{s1}	$\dots$	a_{ss}
	b_1	$\dots$	b_s
	d_1	$\dots$	d_s

Runge-Kutta-Nyström RKN8 Thirteen stages, eighth order, fixed step, from Calvo and Sanz-Serna (1993) [78]:

- $c_1 = 0$, $c_2 = 0.60715821186110352503$, $c_3 = 0.96907291059136392378$, $c_4 = -0.10958316365513620399$, $c_5 = 0.05604981994113413605$, $c_6 = 1.30886529918631234010$, $c_7 = -0.11642101198009154794$, $c_8 = -0.29931245499473964831$, $c_9 = -0.16586962790248628655$, $c_{10} = 1.22007054181677755238$, $c_{11} = 0.20549254689579093228$, $c_{12} = 0.86890893813102759275$, $c_{13} = 1$,
- $b_1 = c_2/2$, $b_i = (c_{i+1} - c_{i-1})/2, 2 \le i \le s-1$, $b_s = (1 - c_{s-1})/2$,
- $d_i = b_i(1 - c_i),\ i = 1, ..., s$,
- $a_{ij} = b_j(c_i - c_j),\ i = 2, ..., s,\ j = 1, ..., i-1$.

Yoshida method

The Yoshida methods are not defined using a Butcher's tableau. Given the initial state $\mathbf{x}_0 = (\mathbf{r}_0, \mathbf{v}_0)^T$ at time t_0, the nth order solution at time $t_0 + h$ is given as a composition of elementary symplectic mappings of lower order, which is equal to the product of the operators:

$$\mathbf{x}(h) = \left[\sum_{i=1}^{k} \exp(c_i h D_T) \exp(d_i h D_V) \right] \mathbf{x}_0 \tag{A.5}$$

where D_T and D_V are differential operators associated with the kinetic and potential terms of the separable Hamiltonian defined in Eq. 2.14, and $\exp(\cdot)$ represents the exponential function. The map above gives a succession of k explicit mappings:

$$\begin{cases} \mathbf{r}_{i+1} = \mathbf{r}_i + c_i h \frac{\partial \mathcal{T}}{\partial \mathbf{v}}(\mathbf{v}_i) \\ \mathbf{v}_{i+1} = \mathbf{v}_i - d_i h \frac{\partial \mathcal{V}}{\partial \mathbf{r}}(\mathbf{r}_{i+1}) \\ i = 1, ..., k \end{cases} \tag{A.6}$$

with $\mathbf{x}_k = (\mathbf{r}_k, \mathbf{v}_k)$ being the solution at time step $t_0 + h$.

Canonical Yoshida method SY4 Four stages, fourth order, fixed step, from Yoshida (1990) [14]:

- $c_1 = 1/(4 - 2b)$, $c_2 = (1 - b)/(4 - 2b)$, $c_3 = c_2$, $c_4 = c_1$,
- $d_1 = 1/(2 - b)$, $d_2 = -b/(2 - b)$, $d_3 = d_1$, $d_4 = 0$,

with $b = 2^{1/3}$.

Canonical Yoshida method SY6 Eight stages, sixth order, fixed step, from Yoshida (1990) [14]:

- $c = \{w_3/2, (w_3+w_2)/2, (w_2+w_1)/2, (w_1+w_0)/2, (w_0+w_1)/2, (w_1+w_2)/2, (w_2+w_3)/2, w_3/2\}$,
- $d = \{w_3, w_2, w_1, w_0, w_1, w_2, w_3, 0\}$,

with $w_1 = -1.17767998417887$, $w_2 = 0.235573213359375$, $w_3 = 0.784513610477560$, $w_0 = 1 - 2\sum w$.

Canonical Yoshida method SY8 Sixteen stages, eighth order, fixed step, from Yoshida (1990) [14]:

- $c = \{w_7/2, (w_7 + w_6)/2, ..., (w_1 + w_0)/2, (w_0 + w_1)/2, ..., (w_6 + w_7)/2, w_7/2\}$,
- $d = \{w_7, ..., w_1, w_0, w_1, ..., w_7, 0\}$,

with $w_1 = 0.102799849391985$, $w_2 = -1.960610232975491$, $w_3 = 1.93813913762276$, $w_4 = -0.158240635368243$, $w_5 = -1.44485223686048$, $w_6 = 0.253693336566229$, $w_7 = 0.91484424622974$, $w_0 = 1 - 2\sum w$.

Dormand-Prince RK8(7) Thirteen stages, eighth order, explicit, variable step, from Prince and Dormand (1981) [25]:

0	0													
1/18	1/18													
1/12	1/48	1/16												
1/8	1/32	0	3/32											
5/16	5/16	0	-75/64	75/64										
3/8	3/80	0	0	3/16	3/20									
59/400	29443841/614563906	0	0	77736538/692538347	-28693883/1125000000	23124283/1800000000								
93/200	16016141/946692911	0	0	61564180/158732637	22789713/633445777	545815736/2771057229	-180193667/1043307555							
5490023248/9719169821	39632708/573591083	0	0	-433636366/683701615	-421739975/2616292301	10030283 1/723423059	790204164/839813087	800635310/3783071287						
13/20	246121993/1340847787	0	0	-37695042795/15268766246	-309121744/1061227803	-12992083/490766935	6005943493/2108947869	393006217/1396673457	123872331/1001029789					
120114681 1/1299019798	-1028468189/846180014	0	0	8478235783/508512852	1311729495/1432422823	-10304129995/1701304382	-48777925059/3047939560	15336726248/1032824649	-45442868181/3398467696	3065993473/597172653				
1	185892177/718116043	0	0	-3185094517/667107341	-477755414/1098053517	-703635378/230739211	5731566787/1027545527	5232866602/850066563	-4093664535/808688257	3962137247/1805957418	65686358/487910083			
1	403863854/491063109	0	0	-5068492393/434740067	-411421997/543043805	652783627/914296604	11173962825/925320556	-13158990841/6184727034	3936647629/1978049680	-160528059/685178525	248638103/1413531060			
0	13451932/455176623	0	0	0	0	-808719846/976000145	1757004468/5645159321	656045339/265891186	-3867574721/1518517206	465885868/322736535	53011238/667516719	2/45		
0	14005451/335480064	0	0	0	0	-59238493/1068277825	181606767/758867731	56129285/797845732	-1041891430/1371343529	760417239/1151165299	118820643/751138087	-528747749/2220607170	1/4	

APPENDIX $\mathcal{B}$

Transformations between probability distributions

This appendix presents the transformations used to map the physical coordinates to the standard normal coordinates and viceversa, as described in Section 3.2.1 of Chapter 3. Treated here are the univariate normal, uniform, and triangular distributions (which are used in SNAPPshot to define the uncertainties on parameters such as the spacecraft area-to-mass ratio and the Δv vector representing a manoeuvre), and the multivariate normal distribution (which is used to define the initial state uncertainty via an input covariance matrix).

All the transformations described here are based on the mapping shown in Equation 3.3, which preserves the CDF between the starting uncertainty and the standard normal distribution that characterises the normalised coordinate space used in the LS algorithm. The latter is represented by the pdf and CDF already expressed in Equations 3.2, 3.1, and 3.6. The direct and inverse transformations follow Equations 3.4 and 3.5, respectively.

Mapping based on multivariate normal distribution (Rosenblatt's transformation)

The explanation presented here follows the one given in [104], using a different notation.

Given the starting distribution of the random vector $\mathbf{X} = (x_1, ..., x_k)^T \in \mathbb{R}^k$ described by the pdf

$$f(\mathbf{x}) = \mathcal{N}(\mathbf{x}; \mathbf{M}, \mathbf{\Lambda}) = \frac{1}{\sqrt{|2\pi\mathbf{\Lambda}|}} \exp\left(-\frac{1}{2}(\mathbf{x}-\mathbf{M})^T\mathbf{\Lambda}^{-1}(\mathbf{x}-\mathbf{M})\right)$$

with average $\mathbf{M} \in \mathbb{R}^k$ and covariance matrix $\mathbf{\Lambda} \in \mathbb{R}^d \times \mathbb{R}^d$, the CDF (defined as $F(\mathbf{x}) = \mathbb{P}(\mathbf{X} \leq \mathbf{x}),$ where $\mathbf{X} \sim \mathcal{N}(\mathbf{x}; \mathbf{M}, \mathbf{\Lambda})$) cannot be obtained in closed form, but only estimated numerically, due to the multidimensionality of the problem.

For this reason, the transformation is treated making use of conditional probabilities, as

$$\begin{aligned}\mathbb{P}(X_1 \leq x_1) &= F(x_1)\\ \mathbb{P}(X_2 \leq x_2|X_1 = x_1) &= F(x_2|x_1)\\ &\vdots\\ \mathbb{P}(X_k \leq x_k|X_{k-1} = x_{k-1}, ..., X_1 = x_1) &= F(x_k|x_{k-1}, ..., x_1)\end{aligned}$$

In this way, the mapping in Equation 3.3 conserving the CDF of the distribution can be rewritten in a more simple way:

$$\begin{aligned}F(x_1) &= \Phi\left(\frac{x_1 - m_1}{\sqrt{\lambda_{11}}}\right) = \Phi(\theta_1)\\ F(x_2|x_1) &= \Phi\left(\frac{x_2 - m_2 + (\Lambda^{(2)}_{21}/\Lambda^{(2)}_{22})(x_1 - m_1)}{\sqrt{\Lambda^{(2)}/\Lambda^{(2)}_{22}}}\right) = \Phi(\theta_2)\\ &\vdots\\ F(x_k|x_{k-1}, ..., x_1) &= \Phi\left(\frac{x_k - m_k + \sum_{j=1}^{k-1}(\Lambda^{(k)}_{kj}/\Lambda^{(k)}_{kk})(x_j - m_j)}{\sqrt{\Lambda^{(k)}/\Lambda^{(k)}_{kk}}}\right) = \Phi(\theta_k)\end{aligned}$$

where $\Lambda^{(r)}$ is the determinant of the minor of Λ defined as $[\lambda ij],\ i, j = 1, ..., r \leq k$, and $\Lambda^{(r)}_{ij}$ is the cofactor of the element (ij) of the minor $\Lambda^{(r)}$.

This way, the direct and the inverse transformations become linear and assume the forms, respectively:

$$\theta_i = \frac{x_i - m_i + \sum_{j=1}^{i-1}(\Lambda^{(i)}_{ij}/\Lambda^{(i)}_{ii})(x_j - m_j)}{\sqrt{\Lambda^{(i)}/\Lambda^{(i)}_{ii}}},\ i = 1, ..., k$$

$$x_i = m_i + \theta_i\sqrt{\Lambda^{(i)}/\Lambda^{(i)}_{ii}} - \sum_{j=1}^{i-1}(\Lambda^{(i)}_{ij}/\Lambda^{(i)}_{ii})(x_j - m_j),\ i = 1, ..., k$$

Mapping based on univariate normal distribution

This mapping can be treated as a particular case of Rosenblatt's transformation for one-dimensional random variables, but is reported here for completeness.

Given the starting distribution with average μ and covariance σ^2, the pdf $f(x)$ and CDF $F(x)$ have the expressions:

$$f(x) = \mathcal{N}(x; \mu, \sigma^2) = \frac{1}{\sqrt{2\pi\sigma^2}}\exp\left(-\frac{(x-\mu)^2}{2\sigma^2}\right) \qquad F(x) = \frac{1}{2}\left[1 + \text{erf}\left(\frac{x-\mu}{\sigma\sqrt{2}}\right)\right]$$

The direct and the inverse transformation have linear expressions, as in the previous case:

$$\theta = \frac{x - \mu}{\sigma} \qquad x = \mu + \sigma\theta$$

Mapping based on uniform distribution

Given the pdf $f(x)$ and CDF $F(x)$ of the starting distribution defined over the interval $[a, b] \in \mathbb{R}$:

$$f(x) = \begin{cases} \frac{1}{b-a} & \text{if } a < x < b \\ 0 & \text{elsewhere} \end{cases} \qquad F(x) = \begin{cases} 0 & \text{if } x \leq a \\ \frac{x-a}{b-a} & \text{if } a < x < b \\ 1 & \text{if} x \geq b \end{cases}$$

The direct and the inverse transformations have the expressions

$$\theta = \begin{cases} -\infty & \text{if } x = a \\ \sqrt{2}\,\text{erf}^{-1}\left[2\frac{x-a}{b-a} - 1\right] & \text{if } a < x < b \\ +\infty & \text{if } x = b \end{cases}$$

$$x = \begin{cases} a & \text{if } -\infty \leftarrow \theta \\ \frac{1}{2}\left[1 + \text{erf}\left(\frac{\theta}{\sqrt{2}}\right)\right](b-a) + a & \text{if } a < x < b \\ b & \text{if } \theta \rightarrow +\infty \end{cases}$$

Mapping based on triangular distribution

Given the pdf $f(x)$ and CDF $F(x)$ of the starting distribution defined over the interval $[a, b] \in \mathbb{R}$ with $a < c < b$

$$f(x) = \begin{cases} \frac{2(x-a)}{(b-a)(c-a)} & \text{if } a < x \leq c \\ \frac{2(b-x)}{(b-a)(b-c)} & \text{if } c < x < b \\ 0 & \text{elsewhere} \end{cases} \qquad F(x) = \begin{cases} 0 & \text{if } x \leq a \\ \frac{(x-a)^2}{(b-a)(c-a)} & \text{if } a < x \leq c \\ 1 - \frac{(b-x)^2}{(b-a)(b-c)} & \text{if } c < x < b \\ 1 & \text{if } x \geq b \end{cases}$$

The direct and the inverse transformations have the expressions

$$\theta = \begin{cases} -\infty & \text{if } x = a \\ \sqrt{2}\,\text{erf}^{-1}\left[\frac{2(x-a)^2}{(b-a)(c-a)} - 1\right] & \text{if } a < x \leq c \\ \sqrt{2}\,\text{erf}^{-1}\left[1 - \frac{2(b-x)^2}{(b-a)(b-c)}\right] & \text{if } c < x < b \\ +\infty & \text{if } x = b \end{cases}$$

$$x = \begin{cases} a & \text{if } -\infty \leftarrow \theta \\ \sqrt{(b-a)(c-a)\Phi(\theta)} + a & \text{if } \Phi(\theta) \leq \frac{c-a}{b-a} \\ b - \sqrt{(1-\Phi(\theta))(b-a)(b-c)} & \text{if } \Phi(\theta) > \frac{c-a}{b-a} \\ b & \text{if } \theta \rightarrow +\infty \end{cases}$$

Bibliography

[1] E. A. Wan and R. Van Der Merwe, "The unscented Kalman filter for nonlinear estimation," in *Proceedings of the IEEE 2000 Adaptive Systems for Signal Processing, Communications, and Control Symposium (Cat. No. 00EX373)*, pp. 153–158, Ieee, 2000.

[2] G. Kminek, "ESA planetary protection requirements, Technical Report ESSB-ST-U-001," *European Space Agency*, 2012.

[3] "COSPAR Planetary Protection Policy," latest version.

[4] ESA NEO Coordination Centre, "WT1190F comes back: ESA NEOCC watching rare reentry," Oct. 2015. [Online; accessed 12 Nov 2019].

[5] C. Colombo, F. Letizia, J. V. den Eynde, and R. Jehn, "SNAPPshot, ESA planetary protection compliance verification software. Final report," *ESA ref. ESA-IPL-POM-MB-LE-2015-315, European Space Agency*, 2016.

[6] NASA, "Galileo End of Mission, Press Kit," Sept. 2003.

[7] NASA, "Cassini End of Mission, Grand Finale," Sept. 2018. [Online; accessed 12 Nov 2019].

[8] J. Laskar, "Large scale chaos and marginal stability in the solar system," *Celestial Mechanics and Dynamical Astronomy*, vol. 64, pp. 115–162, Mar 1996.

[9] D. M. Hernandez, S. Hadden, and J. Makino, "Are long-term n-body simulations reliable?," 2019.

[10] D. Brouwer, "On the accumulation of errors in numerical integration," *The Astronomical Journal*, vol. 46, pp. 149–153, 1937.

[11] A. Milani and A. M. Nobili, "Integration error over very long time spans," *Celestial mechanics*, vol. 43, pp. 1–34, Mar 1987.

[12] E. Hairer, G. Wanner, and C. Lubich, *Geometric Numerical Integration: Structure-Preserving Algorithms for Ordinary Differential Equations*. Berlin, Heidelberg: Springer Berlin Heidelberg, 2002. Corrected second printing (2004).

[13] P. Michel and G. B. Valsecchi, "Numerical experiments on the efficiency of second-order mixed-variable symplectic integrators for n-body problems," *Celestial Mechanics and Dynamical Astronomy*, vol. 65, pp. 355–371, Dec 1996.

[14] H. Yoshida, "Construction of higher order symplectic integrators," *Physics Letters A*, vol. 150, no. 5, pp. 262 – 268, 1990.

[15] J. Laskar and P. Robutel, "High order symplectic integrators for perturbed hamiltonian systems," *Celestial Mechanics and Dynamical Astronomy*, vol. 80, pp. 39–62, May 2001.

[16] J. E. Chambers, "A hybrid symplectic integrator that permits close encounters between massive bodies," *Monthly Notices of the Royal Astronomical Society*, vol. 304, pp. 793–799, 04 1999.

[17] M. J. Duncan, H. F. Levison, and M. H. Lee, "A multiple time step symplectic algorithm for integrating close encounters," *The Astronomical Journal*, vol. 116, no. 4, p. 2067, 1998.

[18] J. Wisdom and M. Holman, "Symplectic maps for the n-body problem," *The Astronomical Journal*, vol. 102, pp. 1528–1538, 1991.

[19] H. F. Levison and M. J. Duncan, "The long-term dynamical behavior of short-period comets," *Icarus*, vol. 108, no. 1, pp. 18 – 36, 1994.

[20] B. Gladman, M. Duncan, and J. Candy, "Symplectic integrators for long-term integrations in celestial mechanics," *Celestial Mechanics and Dynamical Astronomy*, vol. 52, pp. 221–240, Sep 1991.

[21] H. Rein, D. Tamayo, and G. Brown, "High-order symplectic integrators for planetary dynamics and their implementation in rebound," *Monthly Notices of the Royal Astronomical Society*, vol. 489, pp. 4632–4640, 09 2019.

[22] A. Quarteroni, R. Sacco, and F. Saleri, *Numerical Solution of Ordinary Differential Equations*, pp. 479–538. Berlin, Heidelberg: Springer Berlin Heidelberg, 2007.

[23] J. R. Dormand and P. J. Prince, "A family of embedded runge-kutta formulae," *Journal of Computational and Applied Mathematics*, vol. 6, no. 1, pp. 19 – 26, 1980.

[24] J. R. Dormand, M. Elmikkawy, and P. J. Prince, "Families of Runge-Kutta-Nystrom formulae," *IMA Journal of Numerical Analysis*, vol. 7, 04 1987.

[25] P. J. Prince and J. R. Dormand, "High order embedded runge-kutta formulae," *Journal of Computational and Applied Mathematics*, vol. 7, no. 1, pp. 67 – 75, 1981.

[26] E. Everhart, "Implicit single-sequence methods for integrating orbits," *Celestial mechanics*, vol. 10, pp. 35–55, Aug 1974.

[27] E. Everhart, "An efficient integrator that uses gauss-radau spacings," *International Astronomical Union Colloquium*, vol. 83, p. 185–202, 1985.

[28] K. F. Sundman *et al.*, "Mémoire sur le problème des trois corps," *Acta mathematica*, vol. 36, pp. 105–179, 1913.

[29] V. Szebehely, "Selection of regularizing functions," *The Astronomical Journal*, vol. 72, p. 370, 1967.

[30] P. Kustaanheimo and E. Stiefel, "Perturbation theory of kepler motion based on spinor regularization," *J. Math. Bd*, vol. 218, p. 27, 1965.

[31] T. Levi-Civita, "Sur la régularisation du problème des trois corps," *Acta Math.*, vol. 42, pp. 99–144, 1920.

[32] G. Bau, A. Huhn, H. Urrutxua, C. Bombardelli, and J. Peláez, "Dromo: a new regularized orbital propagator," in *International Symposium on Orbit Propagation and Determination, IMCCE, Lille, France*, pp. 26–28, Citeseer, 2011.

[33] J. Roa, M. Sanjurjo-Rivo, and J. Peláez, "Singularities in dromo formulation. analysis of deep flybys," *Advances in Space Research*, vol. 56, no. 3, pp. 569 – 581, 2015. Advances in Asteroid and Space Debris Science and Technology - Part 1.

[34] H. Urrutxua, M. Sanjurjo-Rivo, and J. Peláez, "Dromo propagator revisited," *Celestial Mechanics and Dynamical Astronomy*, vol. 124, pp. 1–31, Jan 2016.

[35] R. H. Battin, *An Introduction to the Mathematics and Methods of Astrodynamics*. AIAA, 1968.

[36] A. Milani, S. R. Chesley, and G. B. Valsecchi, "Asteroid close encounters with earth: risk assessment," *Planetary and Space Science*, vol. 48, pp. 945–954, Aug. 2000.

[37] P. W. Chodas, "Estimating the impact probability of a minor planet with the earth," *Bulletin of the American Astronomical Society*, vol. 25, p. 1236, June 1993.

[38] E. J. McGrath and D. C. Irving, "Techniques for efficient monte carlo simulation. volume iii. variance reduction," 4 1975.

[39] D. K. Yeomans and P. W. Chodas, "Predicting close approaches of asteroids and comets to earth," in *Hazards Due to Comets and Asteroids* (T. Gehrels, M. S. Matthews, and A. M. Schumann, eds.), p. 241, 1994.

[40] P. W. Chodas and D. K. Yeomans, "Could asteroid 1997 xf11 collide with earth after 2028?," in *AAS/Division of Dynamical Astronomy Meeting*, vol. 31 of *Bulletin of the American Astronomical Society*, p. 1227, Sept. 1999.

[41] P. Chodas and D. Yeomans, "Predicting close approaches and estimating impact probabilities for near-earth objects," *Advances in the Astronautical Sciences*, vol. 103, 01 2000.

[42] A. Milani, S. R. Chesley, M. E. Sansaturio, G. Tommei, and G. B. Valsecchi, "Nonlinear Impact monitoring: Line Of Variation searches for impactors," *Icarus*, vol. 173, pp. 362–384, 2005.

[43] D. L. Mathias, L. F. Wheeler, and J. L. Dotson, "A probabilistic asteroid impact risk model: assessment of sub-300m impacts," *Icarus*, vol. 289, pp. 106 – 119, 2017.

[44] A. Milani, M. Sansaturio, G. Tommei, O. Arratia, and S. Chesley, "Multiple solutions for asteroid orbits: Computational procedure and applications," *Astronomy and Astrophysics*, vol. 431, 02 2005.

[45] D. Farnocchia, S. R. Chesley, A. Milani, G. F. Gronchi, and P. W. Chodas, "Orbits, long-term predicitions, and impact monitoring," pp. 815–834, 2015.

[46] G. Tommei, "Nonlinear impact monitoring: 2-dimensional sampling," *Proceedings of the International Astronomical Union*, vol. 2004, no. IAUC197, p. 259–264, 2004.

[47] G. B. Valsecchi, A. Del Vigna, and M. Ceccaroni, "The evolution of the line of variations at close encounters: an analytic approach," *Celestial Mechanics and Dynamical Astronomy*, vol. 131, p. 47, Sep 2019.

[48] R. Jehn, "Estimation of impact probabilities of interplanetary Ariane upper stages," in *Proceedings of the 30th International Symposium on Space Technology and Science, 4-10 Jul. 2015, Kobe, Japan*, 2015.

[49] M. S. Wallace, "A massively parallel bayesian approach to planetary protection trajectory analysis and design," in *AAS/AIAA Astrodynamics Specialist Conference*, Aug. 2015.

[50] J. Barengoltz, "Calculation of the number of monte carlo histories for a planetary protection probability of impact estimation," in *41st COSPAR Scientific Assembly*, vol. 41, 2016.

[51] E. B. Wilson, "Probable inference, the law of succession, and statistical inference," *Journal of the American Statistical Association*, vol. 22, no. 158, pp. 209–212, 1927.

[52] J. Liu, *Monte Carlo Strategies in Scientic Computing*. 02 2009.

[53] A. Morselli, R. Armellin, P. D. Lizia, and F. Bernelli-Zazzera, "A high order method for orbital conjunctions analysis: Monte carlo collision probability computation," *Advances in Space Research*, vol. 55, no. 1, pp. 311–333, 2015.

[54] H. Rickman, T. Wi´sniowski, P. Wajer, R. Gabryszewski, and G. B. Valsecchi, "Monte carlo methods to calculate impact probabilities," *A&A*, vol. 569, p. A47, 2014.

[55] D. Farnocchia, S. Chesley, P. Chodas, M. Micheli, D. Tholen, A. Milani, G. Elliott, and F. Bernardi, "Yarkovsky-driven impact risk analysis for asteroid (99942) apophis," *Icarus*, vol. 224, no. 1, pp. 192 – 200, 2013.

[56] F. Letizia, C. Colombo, J. V. den Eynde, R. Armellin, and R. Jehn, "SNAPPshot: Suite for the numerical analysis of planetary protection," in *Proceedings of the 6th International Conference on Astrodynamics Tools and Techniques (ICATT), 14-17 Mar. 2016, Darmstadt, Germany*, 2016.

[57] F. Letizia, C. Colombo, J. V. den Eynde, and R. Jehn, "B-plane visualisation tool for uncertainty evaluation," in *Proceedings of the 26th AAS/AIAA Space Flight Mechanics Meeting, 14-18 Feb. 2016, Napa, CA*, no. AAS 16-438, 2016.

[58] R. Armellin, P. Di Lizia, F. Bernelli-Zazzera, and M. Berz, "Asteroid close encounters characterization using differential algebra: The case of apophis," *Celestial Mechanics and Dynamical Astronomy*, vol. 107, pp. 451–470, 01 2011.

[59] M. Losacco, M. Romano, P. Di Lizia, C. Colombo, A. Morselli, R. Armellin, and J. M. Sánchez Pérez, "Advanced monte carlo sampling techniques for orbital conjunctions analysis and neo impact probability computation," in *Proceedings of the 1st NEO and Debris Detection Conference, Jan. 22nd-24th 2019, ESA/ESOC, Darmstadt, Germany*, 2019.

[60] A. Fuller, "Analysis of nonlinear stochastic systems by means of the fokker–planck equation†," *International Journal of Control*, vol. 9, pp. 603–655, 01 2007.

[61] Y. Luo and Z. Yang, "A review of uncertainty propagation in orbital mechanics," *Progress in Aerospace Sciences*, vol. 89, pp. 23 – 39, 2017.

[62] S. J. Julier, J. K. Uhlmann, and H. F. Durrant-Whyte, "A new approach for filtering nonlinear systems," in *Proceedings of 1995 American Control Conference-ACC'95*, vol. 3, pp. 1628–1632, IEEE, 1995.

[63] S. J. Julier and J. K. Uhlmann, "Unscented filtering and nonlinear estimation," *Proceedings of the IEEE*, vol. 92, no. 3, pp. 401–422, 2004.

[64] R. Garmier, B. Revelin, P. Legendre, S. Delavault, B. Vidal, and L. Lorda, "Computation of a collision probability based on a gaussian mixture model of the tle accuracy," in *International Symposium on Space Flight Dynamics*, 2009.

[65] G. Terejanu, P. Singla, T. Singh, and P. D. Scott, "Uncertainty propagation for nonlinear dynamic systems using gaussian mixture models," *Journal of Guidance, Control, and Dynamics*, vol. 31, no. 6, pp. 1623–1633, 2008.

[66] D. Giza, P. Singla, and M. Jah, "An approach for nonlinear uncertainty propagation: Application to orbital mechanics," in *AIAA Guidance, Navigation, and Control Conference*, p. 6082, 2009.

[67] D. Giza, P. Singla, and M. Jah, "An adaptive gaussian sum filtering approach for orbit uncertainty estimation," in *AAS/AIAA Space Flight Mechanics Meeting*, pp. 475–488, 2010.

[68] K. J. DeMars, R. H. Bishop, and M. K. Jah, "Entropy-based approach for uncertainty propagation of nonlinear dynamical systems," *Journal of Guidance, Control, and Dynamics*, vol. 36, no. 4, pp. 1047–1057, 2013.

[69] V. Vittaldev and R. P. Russell, "Collision probability for space objects using gaussian mixture models," in *Proceedings of the 23rd AAS/AIAA Space Flight Mechanics Meeting*, vol. 148, pp. 2339–2358, Citeseer, 2013.

[70] S. Frey, C. Colombo, and S. Lemmens, "Interpolation and integration of phase space density for estimation of fragmentation cloud distribution," in *Proceedings of the 29th AAS/AIAA Space Flight Mechanics Meeting, Ka'anapali, HI, USA*, 02 2019.

[71] N. Wiener, "The homogeneous chaos," *American Journal of Mathematics*, vol. 60, no. 4, pp. 897–936, 1938.

[72] B. A. Jones, A. Doostan, and G. H. Born, "Nonlinear propagation of orbit uncertainty using non-intrusive polynomial chaos," *Journal of Guidance, Control, and Dynamics*, vol. 36, no. 2, pp. 430–444, 2013.

[73] R. S. Park and D. J. Scheeres, "Nonlinear mapping of gaussian statistics: theory and applications to spacecraft trajectory design," *Journal of guidance, Control, and Dynamics*, vol. 29, no. 6, pp. 1367–1375, 2006.

[74] M. Berz, "Modern map methods in particle beam physics," *Adv. Imaging Electron Phys.*, vol. 108, pp. 1–318, 1999.

[75] R. Armellin, P. Di Lizia, F. Bernelli-Zazzera, and M. Berz, "Asteroid close encounters characterization using differential algebra: the case of Apophis," *Celestial Mechanics and Dynamical Astronomy*, vol. 107, pp. 451–470, Aug 2010.

[76] A. Wittig, P. Di Lizia, R. Armellin, K. Makino, F. Bernelli-Zazzera, and M. Berz, "Propagation of large uncertainty sets in orbital dynamics by automatic domain splitting," *Celestial Mechanics and Dynamical Astronomy*, vol. 122, no. 3, pp. 239–261, 2015.

[77] B. A. Jones and R. L. Anderson, "A survey of symplectic and collocation integration methods for orbit propagation," in *Proceedings of the 22nd Annual AAS/AIAA Space Flight Mechanics Meeting, 29 Jan. - 2 Feb. 2012 Charleston, SC*, 2012.

[78] M. P. Calvo and J. Sanz-Serna, "High-Order Symplectic Runge-Kutta-Nystrom Methods," *Siam Journal on Scientific Computing*, vol. 14, 09 1993.

[79] F. Debatin, A. Tilgner, and F. Hechler, "Fast numerical integration of interplanetary orbits," in *ESA Special Publication*, vol. 255 of *ESA Special Publication*, Dec. 1986.

[80] E. Zio and N. Pedroni, "Subset Simulation and Line Sampling for advanced Monte Carlo reliability analysis," in *Proceedings of the European Safety and RELiability (ESREL) 2009 Conference*, 2009.

[81] E. Zio, *The Monte Carlo Simulation Method for System Reliability and Risk Analysis*. Springer-Verlag London, 1st ed., 2013.

[82] B. Schutz, B. Tapley, and G. H. Born, *Statistical orbit determination*. Elsevier, 2004.

[83] J. Struckmeier and C. Riedel, "Fundamentals and applications of canonical transformations in the extended phase space," 2003.

[84] A. Morbidelli, *Modern celestial mechanics : aspects of Solar System dynamics*. Taylor & Francis, 2002.

[85] L. F. Shampine, "Some practical runge-kutta formulas," *Mathematics of Computation*, vol. 46, no. 173, pp. 135–150, 1986.

[86] G. Rangarajan, "Symplectic integration of nonlinear Hamiltonian systems," *Pramana*, vol. 48, pp. 129–142, Jan 1997.

[87] G. G. Dahlquist, "A special stability problem for linear multistep methods," *BIT Numerical Mathematics*, vol. 3, no. 1, pp. 27–43, 1963.

[88] E. Forest and R. D. Ruth, "Fourth-order symplectic integration," *Physica D: Nonlinear Phenomena*, vol. 43, no. 1, pp. 105 – 117, 1990.

[89] M. Romano, C. Colombo, and J. M. Sánchez Pérez, "Verification of planetary protection requirements with symplectic methods and Monte Carlo Line Sampling," in *Proceedings of the 68th International Astronautical Congress (IAC), 25-29 Sep. 2017, Adelaide, Australia*, no. IAC-17-C1.9.5, 2017.

[90] P. K. Seidelmann, *Explanatory supplement to the astronomical almanac*. University Science Books, 1992.

[91] A. Masat, "B-plane orbital resonance analysis and applications, perturbed semi-analytical model for planetary protection and defence applied to ballistic resonant flyby design," Master's thesis, Politecnico di Milano, 2019. Supervisors: Colombo, Camilla and Romano, Matteo.

[92] R. A. Broucke and P. J. Cefola, "On the equinoctial orbit elements," *Celestial mechanics*, vol. 5, pp. 303–310, May 1972.

[93] E. J. Opik and O. E.J., "Interplanetary encounters. close-range gravitational interactions.," 1976.

[94] G. Valsecchi, C. Froeschlé, and R. Gonczi, "Modelling close encounters with öpik's theory," *Planetary and space science*, vol. 45, no. 12, pp. 1561–1574, 1997.

[95] G. B. Valsecchi, A. Milani, G. F. Gronchi, and S. R. Chesley, "Resonant returns to close approaches: Analytical theory*," *A&A*, vol. 408, no. 3, pp. 1179–1196, 2003.

[96] D. Amato, G. Baù, and C. Bombardelli, "Accurate orbit propagation in the presence of planetary close encounters," *Monthly Notices of the Royal Astronomical Society*, vol. 470, pp. 2079–2099, 05 2017.

[97] J. R. Silvester, "Determinants of block matrices," *The Mathematical Gazette*, vol. 84, no. 501, pp. 460–467, 2000.

[98] D. P. Hamilton and J. A. Burns, "Orbital stability zones about asteroids: Ii. the destabilizing effects of eccentric orbits and of solar radiation," *Icarus*, vol. 96, no. 1, pp. 43 – 64, 1992.

[99] H. Pradlwarter, M. Pellissetti, C. Schenk, G. Schueller, A. Kreis, S. Fransen, A. Calvi, and M. Klein, "Realistic and efficient reliability estimation for aerospace structures," *Computer Methods in Applied Mechanics and Engineering*, vol. 194, no. 12-16, pp. 1597–1617, 2005.

[100] M. Romano, M. Losacco, C. Colombo, and P. Di Lizia, "Impact probability computation of near-earth objects using monte carlo line sampling and subset simulation," 2019. unpublished manuscript.

[101] S.-K. Au and J. L. Beck, "Estimation of small failure probabilities in high dimensions by subset simulation," *Probabilistic Engineering Mechanics*, vol. 16, no. 4, pp. 263 – 277, 2001.

[102] F. Cadini, D. Avram, N. Pedroni, and E. Zio, "Subset simulation of a reliability model for radioactive waste repository performance assessment," *Reliability Engineering & System Safety*, vol. 100, p. 75–83, 04 2012.

[103] K. Zuev, J. Beck, S.-K. Au, and L. Katafygiotis, "Bayesian post-processor and other enhancements of subset simulation for estimating failure probabilities in high dimensions," *Computers & Structures*, vol. 92-93, 10 2011.

[104] M. Rosenblatt, "Remarks on a multivariate transformation," *Ann. Math. Statist.*, vol. 23, no. 3, pp. 470–472, 1952.

[105] N. Metropolis, A. W. Rosenbluth, M. N. Rosenbluth, A. H. Teller, and E. Teller, "Equations of state calculations by fast computing machines," *The journal of Chemical Physics*, vol. 21, pp. 1087–1092, 1953.

[106] W. K. Hastings, "Monte Carlo sampling methods using Markov chains and their applications," *Biometrika*, vol. 57, pp. 97–109, 1970.

[107] G. B. Arfken and H. J. Weber, "Gram-schmidt procedure," in *Mathematical Methods for Physicists (Sixth Edition)*, pp. 173–174, Elsevier Academic Press, sixth ed., 2005.

[108] E. S. Agency, "Solar orbiter, exploring the sun-heliosphere connection, definition study report," *ESA/SRE(2014)11, European Space Agency*, July 2011.

[109] M. Romano, C. Colombo, and J. M. Sánchez Pérez, "Efficient planetary protection analysis for interplanetary missions," in *Proceedings of the 69th International Astronautical Congress (IAC), 1-5 Oct. 2018, Bremen, Germany*, no. IAC-18-A3.5.10, 2018.

[110] K. J. DeMars, Y. Cheng, and M. K. Jah, "Collision probability with gaussian mixture orbit uncertainty," *Journal of Guidance, Control, and Dynamics*, vol. 37, no. 3, pp. 979–985, 2014.

[111] H. W. Sorenson and D. L. Alspach, "Recursive bayesian estimation using gaussian sums," *Automatica*, vol. 7, no. 4, pp. 465–479, 1971.

[112] K. Vishwajeet and P. Singla, "Adaptive split/merge-based gaussian mixture model approach for uncertainty propagation," *Journal of Guidance, Control, and Dynamics*, vol. 41, no. 3, pp. 603–617, 2017.

[113] J. T. Horwood, N. D. Aragon, and A. B. Poore, "Gaussian sum filters for space surveillance: theory and simulations," *Journal of Guidance, Control, and Dynamics*, vol. 34, no. 6, pp. 1839–1851, 2011.

[114] C. E. Shannon and W. Weaver, *The mathematical theory of communication*. University of Illinois press, 1998.

[115] T. M. Cover and J. A. Thomas, *Elements of information theory*. John Wiley & Sons, 2012.

[116] S. Kullback, *Information theory and statistics*. Courier Corporation, 1997.

[117] K. J. DeMars, *Nonlinear orbit uncertainty prediction and rectification for space situational awareness*. PhD thesis, 2010.

[118] J. R. Dormand and P. J. Prince, "New runge-kutta algorithms for numerical simulation in dynamical astronomy," *Celestial Mechanics*, vol. 18, no. 3, pp. 223–232, 1978.

[119] E. Fehlberg, "Low-order classical runge-kutta formulas with stepsize control and their application to some heat transfer problems," 1969.

[120] E. B. Shanks, "Solutions of differential equations by evaluations of functions," *Mathematics of Computation*, vol. 20, no. 93, pp. 21–38, 1966.

[121] J. C. Butcher, "Implicit runge-kutta processes," *Mathematics of Computation*, vol. 18, no. 85, pp. 50–64, 1964.